

**ENHANCING THE PROPERTIES OF COPPER FOAM WICKS
USING GRAPHENE COATINGS FOR HIGH-PERFORMANCE
VAPOR CHAMBERS AND HEAT PIPES**

A Dissertation
Presented to
The Academic Faculty

by

James Alexander Moss

In Partial Fulfillment
of the Requirements for the Degree
MASTER OF SCIENCE in the
SCHOOL OF MATERIAL SCIENCE & ENGINEERING

Georgia Institute of Technology
May 2023

COPYRIGHT © 2023 BY JAMES MOSS

**ENHANCING THE PROPERTIES OF COPPER FOAM WICKS
USING GRAPHENE COATINGS FOR HIGH-PERFORMANCE
VAPOR CHAMBERS AND HEAT PIPES**

Approved by:

Dr. Vanessa Smet, Co-Advisor
School of Mechanical Engineering
Georgia Institute of Technology

Dr. Meisha Shofner
School of Material Science & Engineering
Georgia Institute of Technology

Dr. Antonia Antoniou, Co-Advisor
School of Mechanical Engineering
Georgia Institute of Technology

Dr. Preet Singh
School of Material Science & Engineering
Georgia Institute of Technology

Dr. Eric Vogel, Co-Advisor
School of Material Science & Engineering
Georgia Institute of Technology

Date Approved: [April 24, 2023]

To my family and friends

ACKNOWLEDGEMENTS

First off, I would like to acknowledge my co-advisors throughout my graduate studies: Dr. Vanessa Smet, Dr. Antonia Antoniou, and Dr. Eric Vogel. All have been great mentors in helping develop not only my thesis but my skills in both the academic and electronic packaging fields. I would also like to thank Dr. Meisha Shofner and Dr. Preet Singh for taking the time to serve on my committee and helping develop my thesis with different perspectives from various fields of material science. I would like to further acknowledge the Bosch GmbH group members – Alexander Frank, Martin Rittner, and Michael Guyenot – for the project’s guidance and funding.

Furthermore, I would like to thank my fellow students Ramón Sosa, Emanuel Torres, and Nithin Nedumthakady for their assistance in developing and characterizing the coating material. I would also like to acknowledge the preliminary work done by Ryan Wong, a graduate student from Georgia Tech, who began the study of new composite wick materials. His mentorship and work were invaluable and helped lead to the discoveries found in this thesis. I would further like to acknowledge Dr. Yogendra Joshi and his student Mete Muslu for their help and guidance with their unique understanding of thermal systems and heat transfer. I would further like to thank the other students of Vanessa’s lab and the fellow students with PRC for encouraging me and supporting my research.

Lastly, I would like to thank my family and friends who have always supported my efforts in developing this thesis throughout my graduate studies. Their support has helped me become the student and person I am today.

TABLE OF CONTENTS

ACKNOWLEDGEMENTS	iv
LIST OF TABLES	vii
LIST OF FIGURES	viii
LIST OF SYMBOLS AND ABBREVIATIONS	xi
SUMMARY	xiii
CHAPTER 1. Introduction	1
1.1 Strategic Need	1
1.1.1 Thermal Densification Of Electronic Systems	1
1.1.2 Capillary-Driven Two-Phase Cooling Systems	6
1.1.3 Wick Structures And Materials	11
1.2 Research Objectives	14
1.2.1 Unique Approach	17
1.2.2 Task Breakdown	19
CHAPTER 2. Literature Review & Methodology	20
2.1 State-Of-The-Art Wicks Structures	20
2.1.1 Sintered Particle Wicks	20
2.1.2 Micropillars	22
2.1.3 Microchannels/Microgrooves	23
2.1.4 Mesh Wicks	24
2.1.5 Foams	25
2.2 Selection Of Graphene	28
2.2.1 Carbon Allotropes	28
2.2.2 Graphene Synthesis Processes	32
2.2.3 Graphene Foams	34
2.3 Preliminary Tested Graphene Foams	38
2.4 Copper-Graphene Composites	41
2.4.1 Graphene Coatings	44
2.5 Characterization Methodology	45
2.5.1 Surface And Structure Analysis	45
2.5.2 Thermal Conductivity Analysis	49
2.5.3 Electrical Conductivity Analysis	50
2.5.4 Mechanical Analysis	50
CHAPTER 3. Single-Layer Graphene Coatings	53
3.1 Acquisition Of Baseline Cu Foams	53
3.2 Low-Pressure Chemical Vapor Deposition	57
3.3 Surface Analysis & Verification	58
3.3.1 SEM Analysis Of Single-Layer Graphene Coating	58

3.3.2	Raman Spectroscopy Of Single-Layer Graphene Coating	60
3.4	Wick Wettability, Permeability, And Capillary Performance With Gr-Coating	61
3.5	Physical Property Characterization Of Gr-Coated Foams	64
3.5.1	Laser Flash Analysis Of Single-Layer Coating	65
3.5.2	Four-Point Probe Analysis Of Single-Layer Coating	67
3.5.3	Uniaxial Tensile Testing Of Single-Layer Coating	71
CHAPTER 4.	Multilayer Graphene Coating	80
4.1	Electroless Deposition Of Intermediate Cu Layer On Gr-Coated Cu Foam	80
4.1.1	Original Electroless Cu Deposition Setup	82
4.1.2	Plating Rate Characterization On Cu Foil Geometries	83
4.2	Secondary Graphene Layer	94
4.2.1	Surface Characterization	94
4.2.2	Thermal Characterization	96
4.2.3	Electrical Characterization	99
4.2.4	Mechanical Characterization	101
CHAPTER 5.	Conclusion	106
5.1	Summary	106
5.2	Pathways for Future Work	108

LIST OF TABLES

Table 1	– Research objectives compared to prior art.	16
Table 2	– Literature review of various state-of-the-art wick structures.	27
Table 3	– Graphene foam properties from literature.	37
Table 4	– State-of-the-art copper graphene composite properties.	43
Table 5	– Relative density averages of the 4 copper foam types chosen for the development of the graphene-coating.	54
Table 6	– Structural properties of baseline pure copper foams.	56
Table 7	– Vertical travel distance of OpticoolA through Cu foams and Gr-coated Cu foams demonstrating the relative capillary performance of foam types.	63
Table 8	– Electrical and thermal properties of Cu and Cu-Gr single-layer foams.	71
Table 9	– Mechanical properties of Cu and Cu-Gr single-layer foams.	75
Table 10	– Thermal diffusivity and conductivity of 40 PPI uncompressed copper foam after multilayer graphene deposition process.	97
Table 11	– Electrical conductivity and resistivity of 40 PPI uncompressed copper foam after multilayer graphene deposition process.	99
Table 12	– Electrical, thermal, and mechanical properties of both 40 PPI foam types	105

LIST OF FIGURES

Figure 1	– Thermal densification of electronic devices with increasing heat fluxes and hot spot densities exceeding that of the Sun’s surface.	3
Figure 2	– Heat flux handling capability of commonly-used thermal solutions for cooling electronic systems.	3
Figure 3	– Increasing energy densities and power with new packaging architectures for miniaturization.	4
Figure 4	– Co-heating of devices in embedded package architectures with no thermal outlet or heat spreader.	5
Figure 5	– Comparison of heat flux uniformity by common heat spreading materials vs. a vapor chamber (TGP).	7
Figure 6	– Diagram of an integrated vapor chamber design.	9
Figure 7	– Cross-sectional view schematic of the working fluid state in the wick structure of a vapor chamber operating in evaporation and boiling regimes and simplified thermal resistance circuit representation of heat transfer mechanisms experienced in both regimes.	10
Figure 8	– Integration of a vapor chamber into a heterogeneous electronic package architecture.	13
Figure 9	– Fabrication and testing workflow of multilayer composite foam.	18
Figure 10	– Sintered wick for a loop heat pipe utilizing both biporous and monoporous structures.	22
Figure 11	– Thermal resistance of various wick structures over increasing power inputs.	26
Figure 12	– Top-down look of a graphene structure (left) and visualization of the sp^2 hybridization of carbon orbitals (right).	31
Figure 13	– Optical image (left) and SEM image (right) of graphene foam wick.	35

Figure 14	– SEM imaging of commercially available graphene foams at a) x35, b) x130, c) x2.00k, and d) 1.80k magnifications.	39
Figure 15	– Raman spectroscopy of commercial 3D graphene foams.	40
Figure 16	– Raman spectra of graphene with differing numbers of layers (L) and highly oriented pyrolytic graphite (HOPG).	48
Figure 17	– Property characterization methods used to evaluate foams: a) uniaxial testing set-up and tool, b) laser flash analysis setup, c) laser flash tool, and d) four-point probe set-up and tool.	52
Figure 18	– Pore and ligament sizes based on foam type.	54
Figure 19	– SEM imaging of 40 PPI 2x compressed copper foam showing nodes with 2, 3, and 4 connections.	55
Figure 20	– Connectivity of the selected foam types.	56
Figure 21	– SEM imaging of Gr-coating Cu foams at a) x1.5k, b) x3.0k, and c) x10.0k.	59
Figure 22	– Raman spectroscopy of Gr-coating on a 40 PPI uncompressed copper foam.	60
Figure 23	– Contact angle measurements of Cu vs Gr-coated copper using water and OpticoolA.	62
Figure 24	– a) The thermal conductivity of Cu foams and Gr-coated Cu foams and the b) thermal conductivity improvement for each foam type at 25°C.	66
Figure 25	– a) The thermal conductivity of Cu foams and Gr-coated Cu foams and the b) thermal conductivity improvement for each foam type at 25°C.	68
Figure 26	– Exchange surface based on the relative density of metal open-cell foams with an average ligament radius of 0.1 mm.	69
Figure 27	– Stress vs. strain curves of Cu and Gr-coated Cu foams for both a) 20 PPI uncompressed and b) 20 PPI 2x compressed.	73
Figure 28	– The a) tensile Young’s modulus, b) tensile yield strength, and c) energy absorption of the base Cu foams vs. Gr-coated Cu foams.	75
Figure 29	– Stress vs. strain of 40PPI uncompressed foam as received (red), annealed (blue), and Gr-coated (black).	78

Figure 30	– Deposition process using a polymer coating as a Cu growth inhibitor to analyze growth rates.	83
Figure 31	– FIB-SEM cross-section of polymer coating and electroless copper interface for deposition rate characterization.	84
Figure 32	– SEM imaging of Cu deposition on Gr-coated Cu foams after original e-less deposition at a) 0.2 M CuSO ₄ (low coverage), b) 0.3 M CuSO ₄ (medium coverage), and c) 0.4 M CuSO ₄ (high, but incomplete coverage).	86
Figure 33	– SEM analysis of electrolessly deposited Cu on a Gr-coated Cu foam.	88
Figure 34	– FIB-SEM cross-section of newly deposition Cu layer on the Gr-coated Cu foam surface.	89
Figure 35	– Raman spectroscopy of Gr-coated Cu foam and electroless Cu layer.	91
Figure 36	– Thermal profile of forming gas reduction process.	93
Figure 37	– SEM analysis of the secondary graphene layer of the multilayer Gr-coating.	95
Figure 38	– Raman spectrum of secondary graphene layer deposited on the intermediate electroless Cu layer.	96
Figure 39	– a) Thermal conductivity of the 40 PPI foam types and b) the percent improvement in thermal conductivity with each additional Gr layer compared to the research objective.	98
Figure 40	– a) Electrical conductivity of the 40 PPI foam types and b) the percent improvement in thermal conductivity with each additional Gr layer compared to the research objective.	101
Figure 41	– a) The stress vs. strain curves of the 40 PPI 2x compressed foam type, b) exploded view of the curve up to 0.5% strain, c) the yield strengths of the 40 PPI foam types, and d) Young's modulus of the 40 PPI foam types with each added layer.	103

LIST OF SYMBOLS AND ABBREVIATIONS

%IACS	-	Percent International Annealed Copper Standard
AFM	-	Atomic Force Microscopy
APCVD	-	Atmospheric Pressure Chemical Vapor Deposition
CNT	-	Carbon Nanotubes
c_p	-	Heat Capacity
CVD	-	Chemical Vapor Deposition
DI	-	Deionized
DSC	-	Differential Scanning Calorimetry
EDS	-	Energy-dispersive X-Ray Spectroscopy
FEA	-	Finite Element Analysis
FIB	-	Focused Ion Beam
FIB-SEM	-	Focused Ion Beam + Scanning Electron Microscopy
Gr	-	Graphene
HOPG	-	Highly Oriented Pyrolytic Graphene
LFA	-	Laser Flash Analysis
LPCVD	-	Low-Pressure Chemical Vapor Deposition
MWNT	-	Multi-Wall Carbon Nanotubes
PPI	-	Pores Per Inch
SEM	-	Scanning Electron Microscopy
SoC	-	System-on-Chip
SoP	-	System-on-Package
STA	-	Simultaneous Thermal Analysis

SWNT	-	Single-Wall Carbon Nanotubes
TEM	-	Transmission Electron Microscopy
TGA	-	Thermogravimetric Analysis
TGP	-	Thermal Ground Plane
UTS	-	Ultimate Tensile Strength
XPS	-	X-ray Photoelectron Spectroscopy
α	-	Thermal Diffusivity
ΔG	-	Differential Gibbs Free Energy
κ	-	Thermal Conductivity
ρ^*	-	Relative Density
ρ_e	-	Electrical Resistivity
ρ_s	-	Sheet Resistivity
σ	-	Electrical Conductivity

SUMMARY

Thermal densification of electronic systems is becoming an increasingly critical challenge for the design of reliable electronic products as the semiconductor industry keeps on pushing the boundaries of miniaturization and functional density. While the latter was pursued almost exclusively through transistor scaling and silicon monolithic integration in the past, Moore's Law's recent slowdown has shifted the focus on system scaling through innovations in package architectures. While 2.5D and 3D integration schemes continue to prevail to support the nascent chiplet revolution, fan-out packaging wherein active and passive components are embedded into the package substrates is emerging as a key technology for continued performance improvements. Such compact solutions only serve to aggravate existing thermal challenges with too much heat trapped in a restricted space, leading to tangible reliability concerns. These trends are only reinforced by the growing adoption of wide bandgap devices with increasing hot spot densities as compared to their silicon counterparts. Thermal dissipation has, therefore, become a limiting constraint in package design, driving the need for innovative, high-performance, heat-spreading solutions capable of handling greater heat flux densities than copper while still directly integrated into the package.

Capillary-driven two-phase systems such as vapor chambers, a planar type of heat pipe, have gained momentum to address this grand challenge. They operate as a passive, closed-loop system wherein a working fluid absorbs the heat generated by the components mounted on the chamber causing a change to a vapor state. The vapors then travel to the cooler parts of the chamber where the working fluid condenses back into its liquid state,

giving off the absorbed heat. The liquid working fluid finally returns to its original position and the cycle repeats itself until the heat is evenly distributed throughout the chamber. The efficiency of such two-phase systems is, therefore, heavily reliant on their wick structure's ability to effectively transfer heat to the working fluid and circulate the working fluid.

Open-cell micro-foams have demonstrated favorable wick characteristics for heat pipe and vapor chamber implementation at high heat flux densities through a balance between permeability and capillary performance. While copper has, to date, been the material of choice for such wicks owing to its excellent thermal conductivity, further performance and miniaturization enhancements require the exploration of advanced materials with superior properties than copper such as graphene. Although graphene's thermal conductivity is an order of magnitude higher than that of copper, graphene foams exhibit poor performance due to low material quality, material content, and structural integrity. As a result, this research explores the use of conformal graphene coatings deposited on open-cell copper foams to enhance their properties and performance.

Monolayer graphene was conformally deposited on copper micro-foams of varying pore sizes, densities, and 3D connectivity of the copper network through a controlled chemical vapor deposition process. The thermal, electrical, and mechanical properties of the foams were characterized before and after graphene coating along with the wettability and permeability of the resulting wick structures to evaluate the potential of this approach in generating high-performance wicks. An electroless copper plating process was further established for the deposition of a thin, conformal layer of copper on graphene to enable a sequential deposition process of alternating copper and graphene layers. This thesis reports the resulting improvements in wick properties and performance from graphene coatings,

establishing this method as a promising pathway for compact and highly efficient in-package heat spreading solutions, capable of mitigating high heat flux densities, and provides design guidelines to maximize benefits from this material innovation with considerations of ease of processability and cost.

CHAPTER 1. INTRODUCTION

1.1 Strategic Need

1.1.1 Thermal Densification Of Electronic Systems

Thermal management of electronic systems has always been a key design consideration as it plays a critical role in products' reliability and operating life. It has now become the limiting physics to system performance in response to the continuous desire for increased functional density and system miniaturization. While traditional heat removal techniques such as heat sinks and air cooling were originally all that was necessary to ensure the thermal stability of consumer products such as laptops and cellphones, it was not long before the increasing components density on one hand, and size reduction, on the other hand, resulted in too much heat trapped in too small a space with heat fluxes beyond what these simple thermal solutions can handle [1]. And nobody wants a phone that is too hot to hold!

This challenge is only further aggravated by advances in device technologies with the wide-scale adoption of wide-bandgap devices and in package architectures with the emergence of diverse 3D integration platforms. On the chip side, transistor scaling following Moore's law has resulted in the thermal densification reported in Figure 1 [2]. In the example of power-hungry logic chips, average heat fluxes are nearing 100 W/cm^2 , which is comparable to a nuclear blast, with a hot spot density exceeding 1 kW/cm^2 while their temperatures still ought to be maintained below 125°C for safe operation. Such heat fluxes cannot be handled with passive cooling solutions nor forced convection and are

already pushing the boundaries of liquid cooling systems as shown in Figure 2 [3]. As for power amplifiers, the GaN technology was recently adopted for systems operating in the mm-wave frequency range to boost their efficiency. These advanced GaN devices also enable a significant reduction in footprint as compared to their Si counterparts at the same power level, at the cost of increased hot spot densities exceeding the heat fluxes experiences on the surface of the sun, as shown in Figure 1.

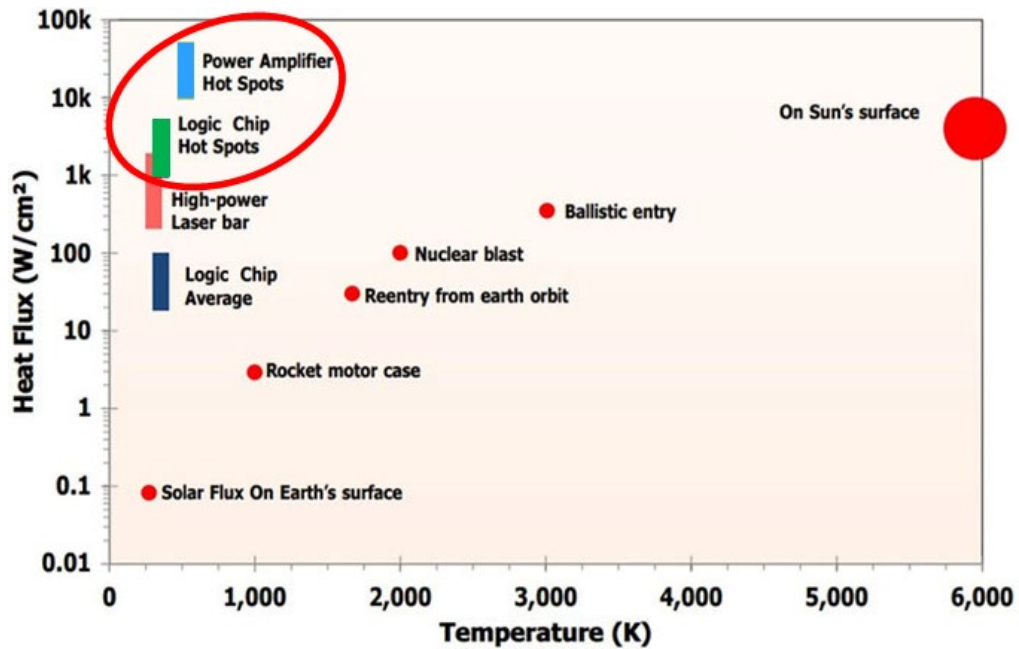


Figure 1 – Thermal densification of electronic devices with increasing heat fluxes and hot spot densities exceeding that of the Sun’s surface [2].

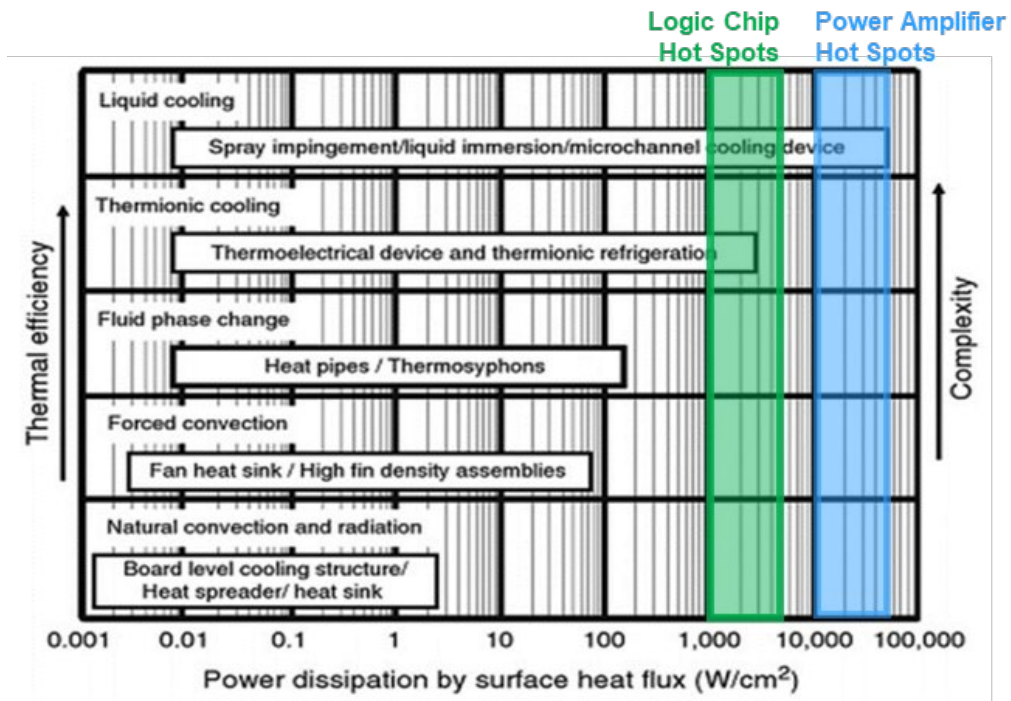


Figure 2 – Heat flux handling capability of commonly-used thermal solutions for cooling electronic systems [3].

To make matters worse, Moore’s Law’s recent slow-down has shifted the spotlight on packaging as the next vector of innovation for continued scaling of system performance. While monolithic silicon integration following the System-on-Chip (SoC) roadmap has been the power horse of the semiconductor industry for many decades, it has now reached its limits, birthing a new era of heterogeneous integration wherein the package now plays the center role in system scaling. This paradigm shift has resulted in rapid advances in package architectures as shown in Figure 3, relying on unique combinations of 2.5D, 3D and fan-out integration schemes as the industry strives to establish a new, disruptive System-on-Package (SoP) roadmap for high-density systems [4].

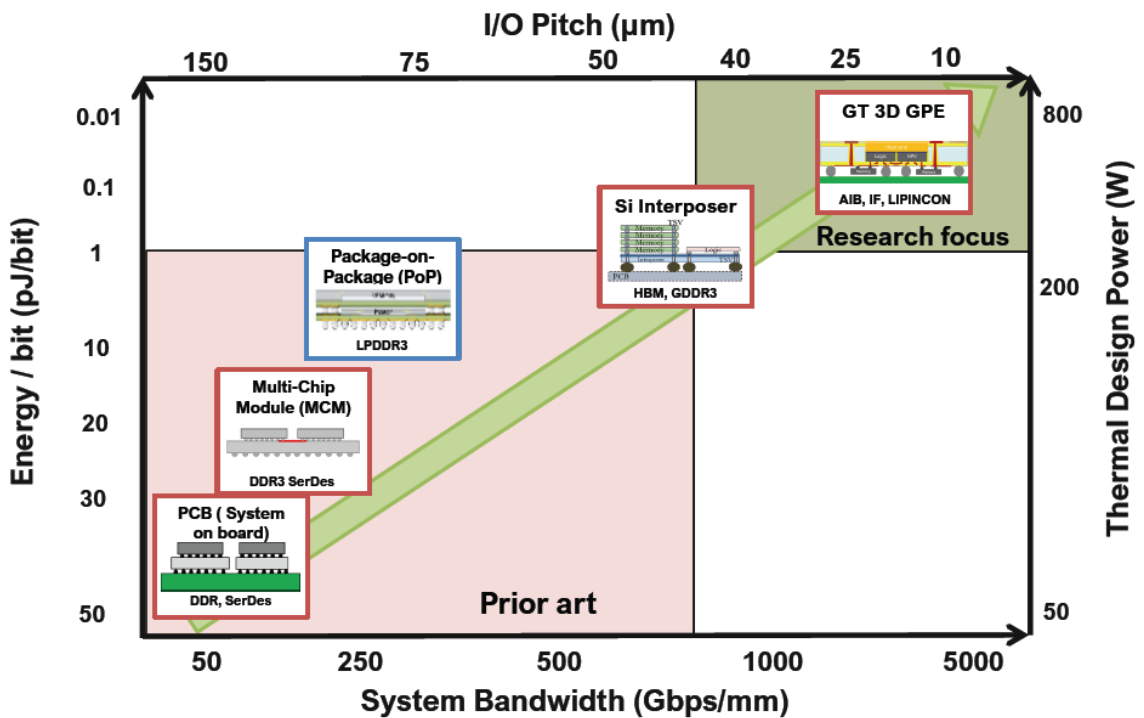


Figure 3 – Increasing energy densities and power with new packaging architectures for miniaturization [4].

These emerging solutions allow for the co-integration of heterogeneous devices from the most advanced technologies and nodes, bridging together, for the first time, the

best of both worlds. However, as high heat-flux devices are integrated closer together, in a planar or, worse, a vertical manner, thermal challenges predictably worsen. In fan-out packages, the most demanding configuration, active and passive components are embedded in the substrate and vertically interconnected with other devices with nowhere for the heat to go resulting in the co-heating of devices illustrated in Figure 4.

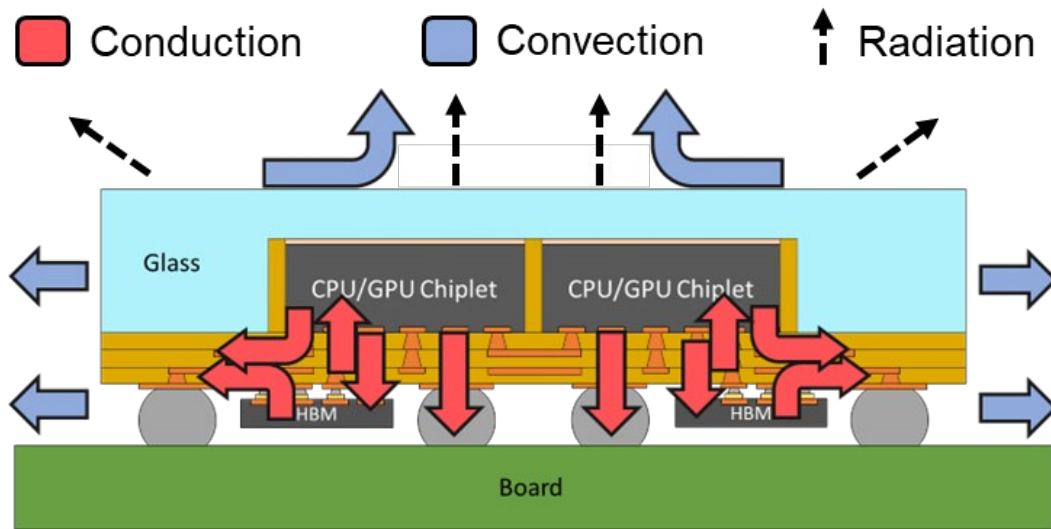


Figure 4 – Illustration of co-heating of devices in embedded package architectures with no thermal outlet or heat spreader.

This brings the need for advanced form- factor- restricted thermal solutions that can be directly integrated into the package, particularly to provide efficient heat spreading to mitigate hot spots and bring heat fluxes down to what can be handled with typical application-driven thermal solutions. High-density hot spots such as the ones generated in GaN devices can result in extreme temperature gradients within the package and, subsequently, in high thermomechanical stresses due to mismatched thermal expansion of the different materials present in the system. This could lead to catastrophic system failures,

the most notorious perhaps being recent incidents of phone battery explosions due to overheating. This, for instance, led to the prompt recall of Samsung's Galaxy Note7 smartphones shortly after their release and has further stressed the criticality of reliable thermal management solutions in portable systems to avoid serious burn and fire hazards. As heat rejection systems are typically integrated at the board level, too far from the heat source, and substrate materials such as copper lack the thermal conductivities to effectively spread heat of that intensity, high-performance heat spreading structures must be implemented at the package level to address this grand challenge. One example of such already in use in consumer and portable electronic systems is heat pipes.

1.1.2 Capillary-Driven Two-Phase Cooling Systems

Heat pipes are capillary-driven closed-loop two-phase systems that utilize the enthalpy change between the evaporation and condensation phases of a working fluid to transport and spread heat internally. Because two-phase systems are closed environments, they can directly be integrated at any level of packaging [5]. By using the latent heat of evaporation of the working fluid, which is usually 1-2 orders of magnitude higher than sensible heat removal, heat pipes are capable of handling much higher heat fluxes than solid metals and carbon-based thermal interface materials, up to $\sim 1 \text{ kW/cm}^2$ as reported in Figure 2. This is illustrated in the finite element analysis (FEA) results of Figure 5, plotting the lateral heat flux distribution of a hot spot of 1 kW/cm^2 initial density provided by a Cu, graphite, or diamond heat spreader as compared to a planar type of heat pipes called vapor chambers [6]. In the model, vapor chambers are referred to as thermal ground planes (TGP). The latter manages to near-evenly distribute the heat, with a $\sim 60\%$ reduction in

maximum heat flux as compared to copper, the material of choice for heat spreading at the package level.

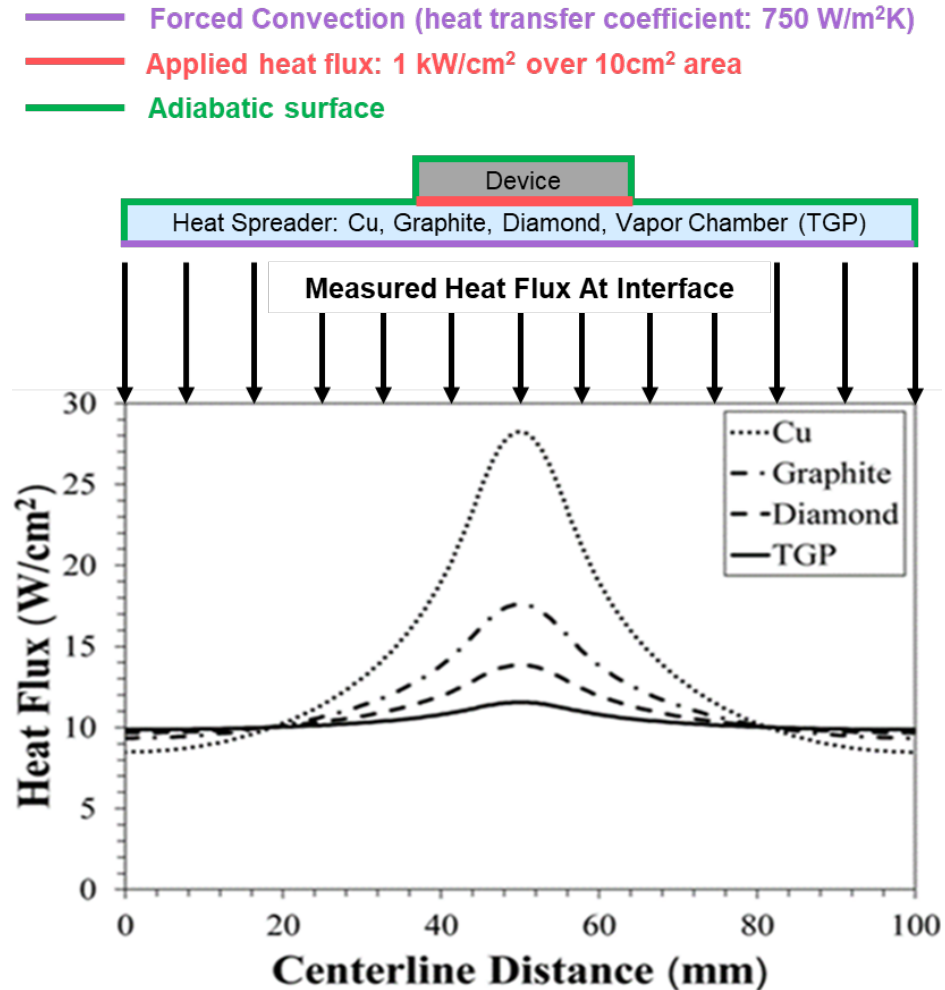


Figure 5 – Comparison of heat flux uniformity by common heat spreading materials vs. a vapor chamber (TGP) [6].

Although vapor chambers are often described as a planar type of heat pipes, the two denominations are typically used to differentiate their direct usage in electronics. Heat pipes are usually designed to spread and transport heat from the source (e.g., active chips) to the heat rejection system (e.g., heat sink, fans) while vapor chambers are directly integrated into a substrate to spread energy densities locally, in other words, mitigate hot

spots. Heat pipes have been integrated into portable devices for some time now, like in Samsung's Galaxy S7 and 7 Edge smartphones released in 2016, while vapor chambers have had limited commercial implementation due to their more recent development. ASUS created GameCool, an integrated 3D vapor chamber cooling system, in 2018 to improve the thermal performance and reliability of their ROG phone. Vapor chambers have been rapidly gaining traction owing to their relatively simple design and smaller form factors that allow for potential in-package integration.

A schematic drawing of a vapor chamber is shown in Figure 6, identifying its main components. The heat source (e.g., chips) is mounted on the evaporator which comprises a wick structure. The latter plays a critical role in the efficiency and reliable operation of the vapor chamber as it ensures the continued presence of working fluid in liquid phase in areas of high thermal density. Furthermore, the wick structure must efficiently conduct heat from the evaporator to the working fluid requiring a high thermal conductivity and surface area. The condenser is integrated at the other end of the vapor chamber and interfaces with the heat rejection system. Condensers are designed to have a high surface area for efficient condensation of the working fluid vapors. The working fluid is expected to have low viscosity and adequate wettability with the material the condenser and evaporator are made of. Deionized (DI) water is commonly used for lab-scale experiments as it is chemically inert, commonly available, and exhibits decent thermal properties for phase-change heat dissipation. Important working fluid properties include the latent heat of vaporization, surface tension, vapor and liquid density, liquid thermal conductivity, liquid viscosity, and

saturation temperature. Other working fluids include acetone, ethanol, methane, ammonia, and various oils depending on the wick material.

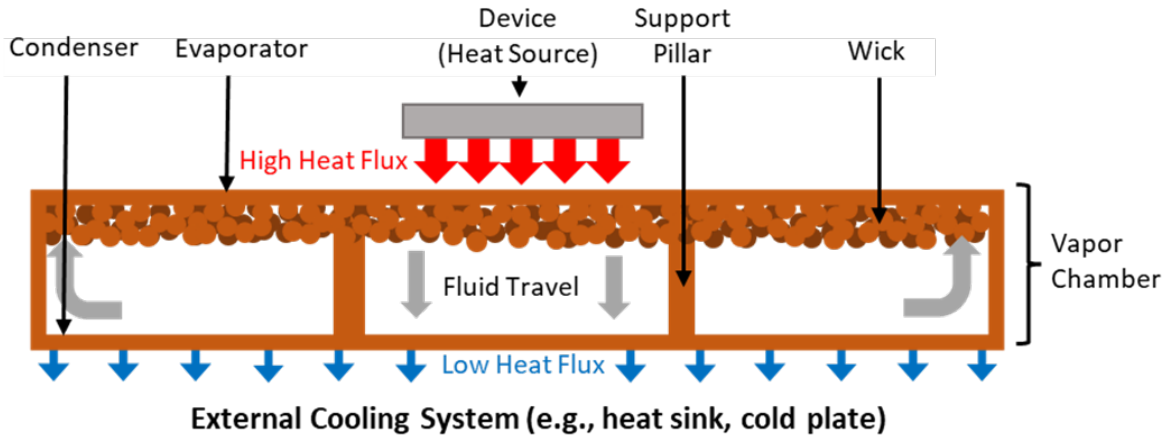


Figure 6 – Diagram of an integrated vapor chamber design.

Vapor chambers have two primary operating regimes: evaporation and boiling, each involving different thermal transport mechanisms with varying efficiency as depicted in Figure 7. The evaporation mode of thermal transport occurs at temperatures below the saturation temperature of the working fluid. Heat is then primarily transported through evaporation from the surface of the working fluid and conduction in the wick material. As there is no internal circulation of the fluid, the evaporation regime is, however, not the most effective at heat spreading and the saturation temperature of the working fluid should, therefore, be well below the maximum temperature admissible by the heat source. Once the saturation temperature is reached, the vapor chamber operates in the boiling regime, which is the most efficient mode of heat transfer due to increased circulation caused by the rapid boiling vapors of the working fluid traveling through the wick. The difference in heat

transfer efficiency between the two regimes is highlighted in the simplified thermal resistance model of Figure 7 [7].

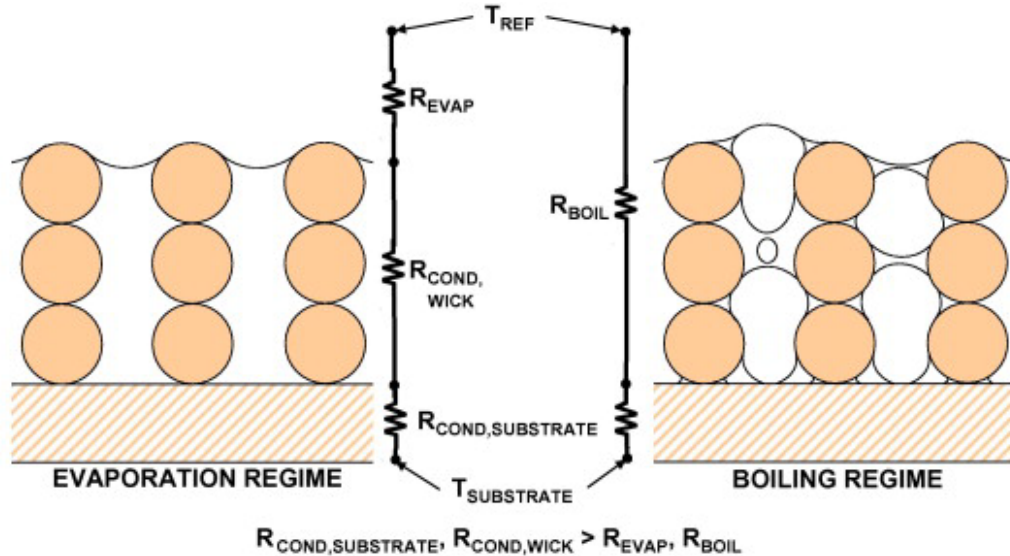


Figure 7 – Cross-sectional view schematic of the working fluid state in the wick structure of a vapor chamber operating in evaporation and boiling regimes and simplified thermal resistance circuit representation of heat transfer mechanisms experienced in both regimes [7].

The effectiveness of the vapor chamber in the boiling regime is heavily influenced by the wick design as poorly designed wicks can trap migrating gases. These trapped gases significantly affect the thermal resistance of the wick and lead to a critical operating limit: dryout, a catastrophic failure of the vapor chamber system that can lead to thermal runaway. Dryout occurs when the two-phase system is pushed beyond its limits, and the working fluid cannot effectively replenish on the evaporator area creating regions of significantly higher thermal densities. Dryout can, however, be delayed through optimization of the wick structure and its thermal properties. To improve the thermal capabilities of the wick, and

in turn, the heat spreading capabilities of two-phase heat spreaders, further design and research into wick structure and materials is critical.

1.1.3 Wick Structures And Materials

The wick in a two-phase system functions as the main structure for facilitating working fluid flow and heat transfer between the evaporator and working fluid. Wick design can be defined in two separate design areas: structure and material. The structure is typically imposed by the fabrication techniques available to realize the desired geometry and feature size, the target heat flux capability and form factor defined by the vapor chamber integration strategy.

Permeability and capillary performance are two significant wick characteristics that influence the structural design. Permeability is defined by the ability of a fluid to flow through the wick and benefits from large pore size and low relative density; however, high permeability trends with increased thermal resistance due to the lower material content. The capillary pressure of the wick is a competing property. Small pore sizes and a highly compact structure increase the capillary action of a system which helps drive fluid circulation and overcome pressure drops that would result in dry-out and failure of the system. Though smaller pore sizes can be favorable for reducing thermal resistance and increasing capillary performance, these features could result in trapping or inefficient gaseous escape during the boiling regime of operation.

Various state-of-the-art wick systems have been developed with unique structures and fabrication techniques designed to tackle the problems around the optimization of permeability versus capillary performance: sintered wicks, wire meshes, micropillars,

microchannels/microgrooves, and open-cell foams reference. The latter have also been demonstrated to provide the lowest thermal resistance for the vapor chamber at high heat flux densities and are, therefore, a promising candidate to support the thermal management needs of emerging electronic systems. To further mitigate the competitive requirements in permeability and capillary performance, biporous wicks – wicks with pore sizes of differing magnitudes – have been evaluated with some regions of the wick that have high permeability to maintain a constant flow of the working fluid, while other regions have high capillary pressure near the surface of the evaporator to maintain a fluid presence at the high-heat flux sources.

With increasing thermal densities, improvements in both wick structure and material are needed to support the thermal management needs of next-generation electronic systems. From a materials perspective, there is a number of properties that can affect the performance of the wick, and, subsequently, of the vapor chamber. Thermal conductivity is a critical property as it directly correlates to the thermal resistance of the wick in both the evaporation and boiling regimes, and thus, the overall thermal resistance of the vapor chamber. Furthermore, high thermal conductivity enhances lateral heat spreading through the wick beyond the footprint of the heat sources to initiate boiling quicker and over a larger area. Thermal conductivity also plays a role in the dispersion of heat during bubble formation to prevent hot spot formation and dryout. The material system selected must also have wetting compatibility with the chosen working fluid for efficient heat transfer at the wick/fluid interface. Furthermore, as wettability is a relationship between the surface energies of the wick material and working fluid, the wetting properties can affect the capillary performance and working fluid circulation throughout the vapor chamber. High

mechanical strengths and toughness are important for wick materials due to the high pressures and fluctuating temperatures that induce tensile, shear, and compressive stresses. Some commercial implementations of vapor chambers – such as in AMD’s new 7900XTX GPU – have even added wicks to the support pillars for both structural support and added working fluid circulation [8]. Finally, with the increased miniaturization of electronic packages and the integration of vapor chambers directly into the substrate, the heat spreading system will begin to take up the decreasing electrical real estate as shown in Figure 8 [9]. This, in turn, results in the need to send electrical signals through the vapor chambers and the possible need for wicks to have a high electrical conductivity on top of the other important material properties.

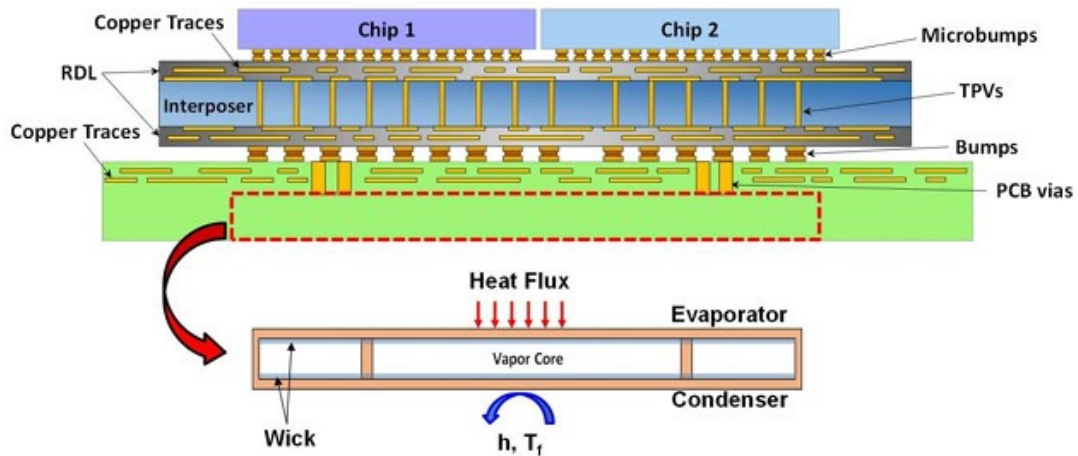


Figure 8 – Integration of a vapor chamber into a heterogeneous electronic package architecture [9].

Aluminum has been recently implemented as a thermal management material due to its low cost and lighter weight than other thermal materials like copper and silver. However, aluminum has a thermal conductivity of 239 W/mK, well under what’s needed

for systems with immense power densities. Aluminum also suffers from challenges in structural integrity due to its low Young's modulus (68 GPa). Furthermore, aluminum struggles with self-oxidation on its surface making fabrication difficult in room temperature and high-temperature settings. Silicon has also been implemented into thermal management solution technologies due to the matching CTEs between the substrate and devices. This significantly reduces the shear stress at elevated temperatures, but silicon has a significantly lower thermal conductivity (148 W/mK) to effectively remove or spread heat in most applications. Polymer systems have also been implemented into niche areas of thermal management due to the rise in flexible, low-power electronics. Copper has been the primary wick material due to its high thermal conductivity (386 W/mK), mechanical toughness, and versatile fabrication technologies; however, copper struggles in compatibility under intense heat due to its high coefficient of thermal expansion (16.7 ppm/°C) compared to device and substrate materials (4 – 6 ppm/°C). Similarly, to aluminum, copper naturally oxidizes - with increased oxidation rates at higher temperatures - leading to added system fabrication complexities and reduced longevity if not protected properly. As shown in Figures 1 and 2, copper is not a suitable material for future heat-spreading applications of high thermal densities (heat fluxes $> 1000 \text{ W/cm}^2$) and the development of new, high-performance materials are necessary for the thermal reliability of electronic packages.

1.2 Research Objectives

As the properties of copper limit the thermal capabilities of future packaging architectures, a new material of higher thermal conductivity than pure copper must be developed. In this research, a wick material system is researched, designed, and fabricated

for implementation into high-performance, high-heat flux heat spreading systems. The objective is to choose an optimal wick structure to develop a material system that is capable of managing heat fluxes well beyond the prior art shown in Table 1, possibly towards heat fluxes of $+1000 \text{ W/cm}^2$. Improvements in the thermal conductivity of the wick are the most desirable as thermal conductivity has a significant effect on the thermal resistance of the vapor chamber during both evaporation and boiling regimes. Mechanical properties will also be evaluated for the implementation of wicks onto support structures to add both structural stability of the chamber during charging of the working fluid and use as well as increased fluid circulation. The new material must also maintain or improve the wetting characteristics and capillary performance so that it does not affect the efficiency of heat transfer at the wick/working fluid interface. Finally, electrical evaluation of the wick will be performed for the implementation of electrical wiring into substrate-integrated vapor chambers without taking up electrical real estate.

Table 1 – Research objectives compared to prior art.

	Objectives	Prior Art
Performance	<ul style="list-style-type: none"> •Synthesis and characterization of foams with high thermal conductivity (κ) improvements (> 20% of Cu foams) •Maintain or increase the wettability and capillary performance of the foam •Mechanical strengths above the minimum sealed chamber vapor pressure by API 682 standards (pressure > 340 kPa) •Maintain or increase the electrical conductivity (σ) 	Systems
		Graphene Foams [10]
		<ul style="list-style-type: none"> - Performed twice as well as their copper counterpart - <i>Heat Flux</i> ≥ 80 W/cm²
		Copper Foams [11]
		Composites
		Sintered Cu-Gr [12]
		<ul style="list-style-type: none"> - 20% κ increase
		Multilayer Cu-C nanotube [13]
		<ul style="list-style-type: none"> - 25% σ increase

Graphene (Gr) has recently been introduced into thermal and electrical systems due to its uniquely high thermal, electrical, and mechanical properties and was originally chosen to be the wick material for the application. Previous work at Georgia Tech by fellow student Ryan Wong was performed to benchmark the usability of commercially available graphene foams as wicks. Thermal, mechanical, and structural data indicated that these graphene foams would not perform at the desired levels due to their low material content and graphitic nature. Because of these results, a new graphene-coated copper foam structure was designed. As copper is already a commonly used material in thermal systems, graphene would allow for further compatibility and performance through mechanical, thermal, and electrical property improvements. The foam wick was selected as the primary wick structure for the composite due to its low thermal resistance compared to other wicks and high permeability for the deposition of the coating layers. Furthermore, foams can be

easily analyzed with various characterization techniques due to their open-cell structure. The fully open network provides an excellent starting point for the preliminary work and could be implemented into other wick systems in the future. Based on the new design, the research focus shifted to developing a Cu-Gr-coated foam with increased thermal properties over pure copper compared to other state-of-the-art copper-graphene fabrication methods. Other methods typically utilize a sintering process or electroless deposition process to integrate graphene sheets into the copper matrix, but these methods often do not utilize the full potential of graphene due to the misalignment of the graphene inclusions.

1.2.1 Unique Approach

Using state-of-the-art deposition techniques, a new, multilayer graphene-coated copper material would be fabricated creating a fully 3-dimensional graphene network using copper as its reinforcement. Ideally, parallel, single-layer graphene networks would be separated by intermediate conformal copper layers. To perform the graphene deposition, low-pressure chemical vapor deposition – designed to deposit graphene on base copper substrates – would be used to deposit a fully connected graphene layer of uniform thickness throughout the foam. The resulting structure would then be closely monitored through surface, structure, and bulk property characterization techniques to analyze the effect of each layer. The deposition of the intermediate copper layer is performed through electroless deposition to create a conformal copper coating on the graphene surface. The copper deposition process is designed and based on typical electroless copper techniques and preliminary literature. A secondary graphene layer is also applied to understand the benefits of multiple graphene layers for future projects and endeavors. The fabrication and testing workflow of the multilayer foam is shown in Figure 9.

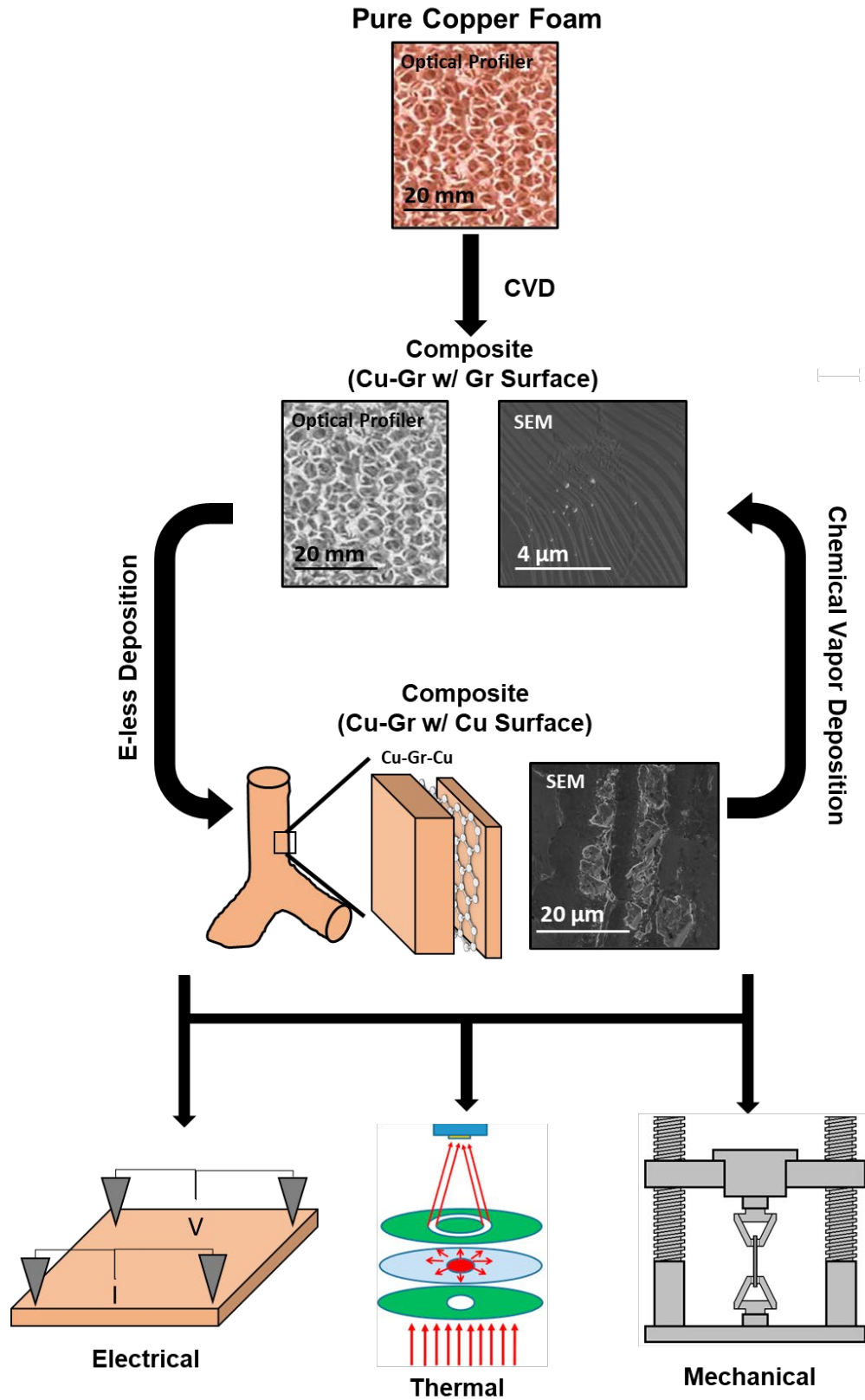


Figure 9 – Fabrication and testing workflow of multilayer composite foam.

1.2.2 Task Breakdown

For this research, the backbone of the composite material is selected based on literature studies of state-of-the-art wicks and benchmarking of base wick material and structure is to be performed. The benchmarking determines both the structural components (e.g., pore size, connectivity, etc.) and effectiveness as a wick (e.g., permeability, capillary pressures). After initial screening, baseline property characterization is performed as a starting comparison for additional coating layers. Primary property characterization of an effective wick structure is focused on thermal, mechanical, and electrical improvements. Along with analyzing electrical conductivity for the multifunctionality of vapor chambers, electrical conductivity also trends similarly with thermal conductivity for bulk materials and provides a quick, effective way to gauge property improvements. The material system's wick performance properties (e.g., wettability, capillary pressures, and permeability) must also be evaluated to ensure there is no harmful effect on the graphene layer. After evaluation of the initial, single-layer graphene coating, an electroless deposition process of the copper layer is to be optimized to ensure a high level of conformal copper coverage of the graphene layer for proper separation of graphene networks. Furthermore, after each deposition process, the layers are to be closely analyzed for potential unwanted structures that could influence wick performance. A secondary graphene layer will then be deposited to understand the effects of separated graphene networks as a coating. Evaluation of how each layer impacts the foam will drive further research and implementation of both the composite coating and foam structure.

CHAPTER 2. LITERATURE REVIEW & METHODOLOGY

2.1 State-Of-The-Art Wicks Structures

The design of the wick structure for a two-phase system is critical for creating an effective thermal spreading system. As previously mentioned, there are five common wick types implemented in literature for various applications: sintered particle wicks, micropillars, microchannels, meshes, and foams. Each wick structure has unique properties and manufacturing techniques making them viable for different electronic packaging environments. State-of-the-art wick research is shown in Table 2 to compare their thermal properties and capabilities when implemented into vapor chambers. Favorable characteristics of vapor chambers include low thermal resistance and high maximum heat flux. Wicks help these properties by having high thermal conductivities with effective permeability and capillary pressures. Each wick structure was evaluated using the literature of prior art systems to understand which would be the best backbone for the coating system.

2.1.1 *Sintered Particle Wicks*

Sintered particle wicks are one of the most commonly implemented wick systems due to their high density and capillary performance. Sintered particle wicks are fabricated through the sintering of metal microparticles. Monoporous sintered wicks are a type of sintered metal wick that utilizes a singular particle size to achieve a relatively uniform pore size distribution; however, these wick types struggle with low permeability and high thermal resistance. To combat these issues, biporous sintered wicks were developed using 2 different particle size ranges – one being a magnitude larger in diameter. T. Semenic &

I. Catton [14] demonstrated the effects of changing the particle size in both monoporous & biporous sintered wick types. Through the evaluation of monoporous wicks, the smallest particle sizes with a diameter of $\sim 100 \mu\text{m}$ had the best heat flux performance over the larger $\sim 300 \mu\text{m}$ and $\sim 600 \mu\text{m}$ particle wicks. These wicks dried up around 300 W/mK , significantly lower than the target of 1000 W/mK . The biporous wicks, on the other hand, should better heat flux capabilities all with maximum heat fluxes at or above 400 W/mK . Wick thermal resistances at the critical heat flux ranged between $0.95 - 0.195 \text{ K/W/cm}^2$, the lower is related to a smaller wick thickness and smaller diameters of the larger particle size. The critical heat flux of the wicks showed greater performance with thicker wick systems and larger diameters of the larger particle pair. J. Weibel et. al. [7] also demonstrated that increased wick thicknesses $> 1.0 \text{ mm}$ show potential for a wick system capable of heat fluxes well above 500 W/mK . The porosity of these biporous wicks is around 65%, or 35% relative density, with high capillary pressures. As monoporous wicks show high capillary performance as standalone structures, S. C. Wu et. al. [15] developed a double-layer loop heat pipe in which the inner layer is a monolayer wick, while the outer is biporous which is depicted in Figure 10.

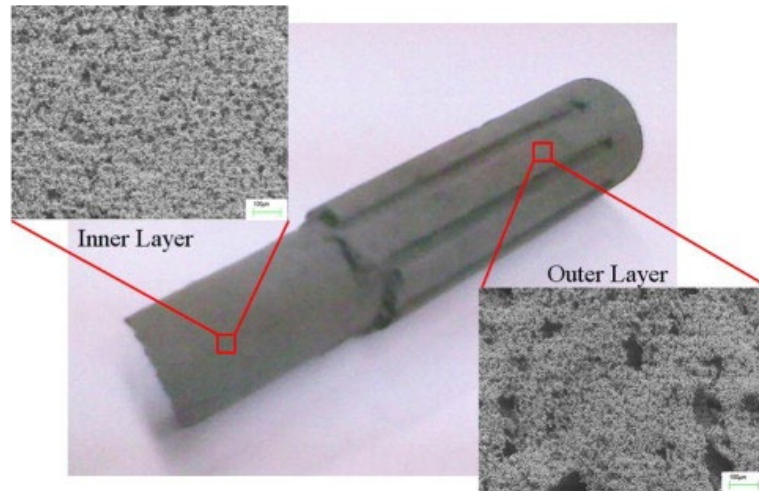


Figure 10 – Sintered wick for a loop heat pipe utilizing both biporous and monoporous structures [15].

The double-layer heat pipe showed a thermal resistance of 0.08 K/W, half the resistance of the tested monoporous wick used (0.17K/W). Though hybrid sintered wicks show promise towards reaching a heat flux of 1000 W/mK, for the application of creating a Gr-coated copper wick, sintered particle wicks could cause issues as the high number of irregular particles could cause discontinuities to the graphene network, as well as insufficient deposition of the graphene and copper layers due to the low permeability of the wicks. Furthermore, closed porosity along with potential insufficient mixing of sintered particles during sintering can cause unwanted uncertainty and added thermal resistances.

2.1.2 Micropillars

A wick system designed around higher predictability and fabrication is micropillars. Micropillars can be fabricated through both additive and subtractive methods giving high levels of fabrication flexibility for structure design and material. Pillar cross-sections can have customizable shapes and sizes for various organization techniques. The

customization can accurately control the desired capillary pressures and permeability, though capillary pressures are typically lower due to the open top of the micropillar structure. Silicon integration has been introduced through micropillars due to the similar fabrication techniques used in device and substrate manufacturing. As the fabrication of these wicks has less uncertainty and randomness, predictive modeling is commonly used to understand the performance metrics of these wick systems. S. Q. Cai. and A. Bhunia [16] demonstrate the geometric effects of the wick system by analyzing the ratio between heater width and wick thickness. For wicks of small thickness and larger heater size, the dominant controller of performance was liquid flow resistance creating an emphasis on the importance of high permeability in wicks. For wicks of large thickness and small heater size, the maximum heat flux was dominated by the ratio of the micropillar diameter to wick thickness. Though micropillars show promise for thermal applications and predictability, they do not provide any mechanical support and have a high thermal resistance for vapor chamber systems making them unfavorable candidates for investigation of the graphene coating.

2.1.3 Microchannels/Microgrooves

Microchannels and microgrooves are another form of wick structure designed around simple and predictable fabrication. Opposed to micropillars, microchannels allow for a more directional flow of working fluid, though they have a higher thermal resistance and lower capillary performance compared to other wick systems. However, because of the increased surface area and lower capillary action, Chen et al. [17] implemented microgrooves onto the condenser side of the vapor chamber to increase the area for condensation. Furthermore, Chen et al. [17] improved the capillary performance of the

microgrooves by keeping grain-like structures formed during milling in the grooves. The technique created an ultra-thin aluminum vapor chamber capable of dissipating 160 W and thermal resistance of 0.156 K/W. Wong et al. [18] fabricated a flat heat pipe using parallel grooves made from oxygen-free copper. Using acetone as its tested working fluid, the heat pipe managed a thermal resistance of 0.0868 K/W. However, microchannels and microgrooves are implemented into thin, low-power vapor chamber applications making them undesirable for coating research. Furthermore, these wick structures require increased mechanical support pillars to maintain reliability under pressurization. Characterization of the mechanical properties would also be difficult as techniques are limited to local area testing such as micro- and nano-indentation.

2.1.4 Mesh Wicks

Mesh wicks are another wick designed specifically around miniaturization and integration. Mesh wicks allow for the fabrication of sub-millimeter-thick vapor chambers because the meshes are sub-100 microns thick. Mesh wicks typically utilize a metal with high thermal conductivity to maintain a high heat transfer capacity with an ultra-thin design. Mesh wicks are fabricated through the sintering of stacked woven metal wire sheets. Wire meshes maximize the capillary performance of the wick over permeability due to size and implementation; however, with the increasing power densities of miniature devices as well, Lui et al. [19] developed a thin screen mesh wick with improved wick performance by laser etching the wick to increase surface area and nucleation sites for boiling. The study analyzed thin vapor chambers with various laser-etching area ratios and managed to decrease the thermal resistance by 23.9% and increase the heat transfer capacity by 20%. The maximum laser-etching area ratio evaluated was at 83.3% and

created a superhydrophilic surface – tested through water contact angle measurements. Huang et al. [20] also developed a wick modification process for copper mesh wicks using O₂ plasma to create a superhydrophilic surface. The process was able to generate a vapor chamber with a thermal resistance of 0.197 K/W. As wire mesh wicks are ultra-thin, added support structures are typically needed for the mechanical stability of the vapor chamber structure. Huang et al. [21] fabricated a wick structure multi functionalizing the supports as working fluid transporting wicks using spiral woven wire meshes. The ultra-thin vapor chamber design had a maximum effective thermal conductivity of 25200 W/mK at 9W. Wire meshes typically have a higher thermal resistance due to the thermal interfaces created during the wire sintering though the lower thermal resistance values come from the low thickness of the overall two-phase system.

2.1.5 Foams

Finally, foam wicks are a common wick choice for both high and low-power applications due to their high permeability and low thermal resistance. Foam wicks have multiple methods of fabrication including casting, sponge-replication techniques, and additive manufacturing. Casting is a common form of open-cell foam creation as it maintains a low thermal resistance and high strength in a continuously reinforced structure. Sponge-replication is another form of metal foam fabrication but can lead to closed porosity with the nodes and ligaments resulting in worse mechanical performance [22]. The foams thus require post-processing to reduce the porosity. Metal open-cell foams struggle with capillary performance due to pore sizes and difficulty in miniaturization. Ryu et al. [23] fabricated a bilayer structure combining the high capillary pressures of micropillars with the high permeability and working fluid transportation of metal foams.

The metal foam had 5x times the permeability of the microposts, increasing the maximum heat flux by over 150%. Sun et al. [24] further demonstrated the low thermal resistance (+30% lower than any other structure) of foam structures at high-power inputs (> 100W) due to the foams' higher permeability for vapor transportation as shown in Figure 11.

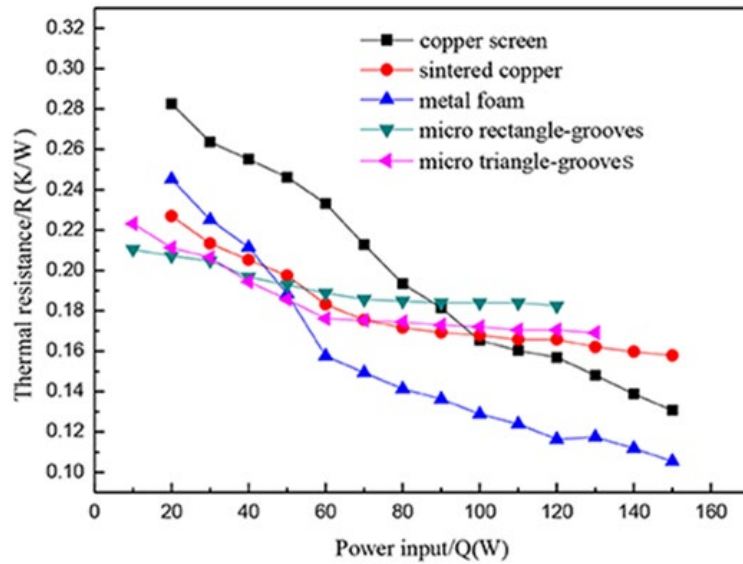


Figure 11 – Thermal resistance of various wick structures over increasing power inputs [24].

Lu et al. [15] designed and tested a graphite foam to compare the use of graphite over copper foams. The vapor chamber structure uses ethanol as its working fluid to demonstrate stable performance at a heat flux of 80 W/cm². Because graphite is hydrophobic when exposed to air, O₂ plasma would be required to achieve better wetting of the foam when using water as the working fluid. Through literature evaluation, the foam wick structure was identified as a promising structure type for increasing the heat-spreading capabilities of vapor chambers; however, new material systems that surpass the capabilities of copper are necessary for these advancements.

Table 2 – Literature review of various state-of-the-art wick structures.

Ref.	Wick Type	Material	Working Fluid	Porosity Or Particle Size	Dimensions (mm ³)	CHF (W/cm ²)	Thermal Res. (K/W)	HTC (W)
[25]	Sintered	Cu	Water	27.45% - 73.39%	40 x 70 x 3	34.67	<0.4833	>50
		Cu	Water	d = 41/302 um		244		
		Cu	Water	d = 58/302 um		293		
[14]	Sintered	Cu	Water	d = 72/302 um		311		
		Cu	Water	d = 74/302 um		321		
		Cu	Water	d = 83/302 um		334		
[7]	Sintered	Cu	Water	63% - 65%		>500	<0.3	
[6]	Sintered	Cu			107 x 99 x 5.5	450	0.15	
[26]	Sintered	Cu	Water	68%	76 x 60 x 6		0.18	
[27]	Sintered	Cu		50%	30 x 30 x 1 - 3	> 100		
[28]	Sintered	Cu		36%	81 x 76 x 5		0.092	
[19]	Mesh	Cu	Water	70.80%	30 x 30		<0.56	100
[29]	Mesh	Cu			104 x 14 x 0.4		1.06	4.50
[21]	Mesh	Cu			100 x 15 x 0.5		0.48	7.58
[30]	Mesh	Cu			100 x 50 x 0.95		0.39	30.25
[31]	Mesh	Cu			100 x 36 x 0.91		3.87	5.4
[20]	Mesh	Cu			100 x 65 x 1.26		0.197	50
[32]	Mesh	Cu			130 x 70 x 1.31		< 3.0	30
[33]	Mesh	Stainless Steel			70 x 70 x 0.2		1.54	15.36
[11]	Foam	Cu	Water	95%		450	> 0.03	
[23]	Pillars + Foam	Cu		pillars: 60%, foam: 96%	30 x 30	>400		
[10]	Foam	Graphite	Ethanol	71%	25 x 25 x 6	80	0.4	
[34]	Pillars	Cu	Water		2 x 2	>800		
[35]	Pillars	SU-8			10 x 20 x 0.3			9.54
[36]	Pillars	Si	Water			>40		
[17]	Grooves	Al	Water		120 x 120 x 2		0.156	160
[37]	Grooves	Cu	Water		90 x 70 x 6	10	0.24	
[38]	Grooves	Cu	Ethanol		60 dia. x 3		0.67	

2.2 Selection Of Graphene

When identifying materials of high thermal conductivity, the carbon family is commonly brought into the conversation. Diamond, graphite, carbon nanotubes, and graphene are all carbon-based materials of high thermal conductivity that have previously been implemented into thermal management systems. From the design standpoint of implementing these systems into a foam geometry, diamond is unsuitable for this application due to its high hardness and brittle nature. Furthermore, graphite has proven to be a low-performing material system due to its low mechanical strength and electrical conductivity compared to copper.

2.2.1 Carbon Allotropes

2.2.1.1 Fullerene

The research of carbon nanostructures began with the discovery of fullerene in the form of C₆₀, otherwise known as buckminsterfullerene. Fullerene is a ball-shaped cage of sp² hybridized carbons with incredibly high strength and chemical stability and is considered a 0-D carbon. Fullerenes come in a multitude of sizes (C₆₀, C₇₀, C₈₀, etc.) and are mostly found as C₆₀. As all the carbon atoms are covalently connected to other carbon atoms, these structures are composed of strong bonds but rely on weaker Van Der Waals forces when formed into bulk fullerene materials. A C₆₀ fullerene structure is measured to be roughly 7.0 x 10⁻¹⁰m wide in diameter making it an excellent nanomaterial for matrix inclusion and transportation in biomedical treatments [39]. Though C₆₀ has demonstrated low electrical conductivity at room temperature, crystalline C₆₀ has shown superconductivity at cryogenic temperatures with alkali and alkaline earth metals [40].

Fullerenes can be fabricated in multiple different methods such as the vaporization of graphite and combustion of simple hydrocarbons. Characterization of these molecules includes Raman spectroscopy, UV-Vis, and FT-IR.

2.2.1.2 Carbon Nanotubes

Carbon nanotubes (CNT) are another carbon allotrope utilizing sp^2 hybridized carbon bonds. Carbon nanotubes are cylindrically structured with hexagonal patterning of carbons. Carbon nanotubes can be single (SWNT) or multi-walled (MWNT) structures in which outer walls act as chemical protectors of the inner walls though double-walled structures have 50% of the conductivity of SWNT [41]. Carbon nanotubes gain their high electrical conductivity ($\sigma > 10^7$ S/m) from the extra free electron of the sp^2 arrangement [42]. The unique nature of the nanotubes allows for easy characterization like Fullerene. Nanotubes mainly have freedom in their length making them one-dimensional carbon structures. Though nanotubes do not have definitive lengths and sizes like fullerene, they are currently limited to the nanoscale due to low structural stability at larger sizes. Current uses of nanotubes include inclusions in composite matrixes to improve mechanical, thermal, and electrical properties or in the creation of bulk carbon materials by the binding of CNT fragments. Because of this, bulk carbon nanotube materials have properties significantly lower than that of individual nanotubes. Cho et al. [43] demonstrated the effects of increasing the MWNT wt% in a polymer matrix increasing the composites' compressive strength 10x. Furthermore, a significant increase in thermal conductivity was seen with 5.0 wt% MWNT. Carbon nanotubes have also been implemented into copper matrixes to create ultra-conductive copper composites. Li et al. [13] deposited carbon nanotubes onto a copper substrate through electrospinning and recoated with copper

through copper sputtering and annealing. The process reduced the resistivity of their samples by ~20% with 10 wt% CNT and increased Young's modulus of the samples by as much as ~25%. Carbon nanotube/copper composites have also been fabricated through an electroless deposition process to coat substrates and by the sintering of homogeneously dispersed composite particles.

2.2.1.3 Graphene

Lastly, graphene has become the most important carbon allotrope in the realm of electronics and thermal systems. Like the other carbon structures, graphene is formed by sp^2 hybridized carbon bonds to three other carbon atoms; however, the structure of pure, monolayer graphene remains flat and continues in two dimensions with no variation in the Z-axis. The unit cell is composed of 2 carbon atoms with a highly symmetrical space group of P6/mmm [44]; therefore, graphene has isotropic in-plane properties. The structure and bonding of graphene are shown in Figure 12 for an understanding of its dimensionality.

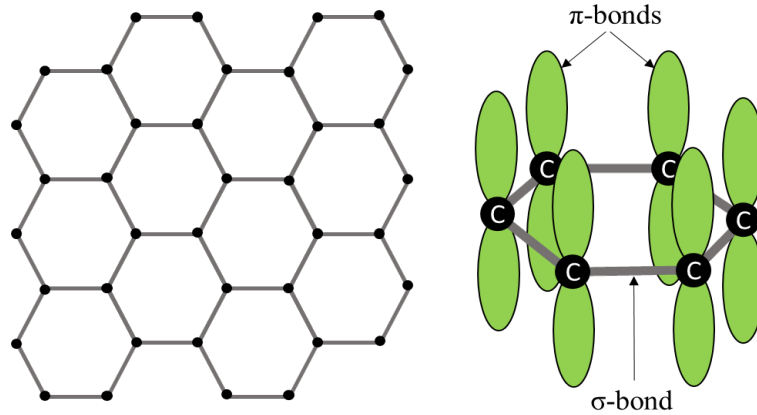


Figure 12 – Top-down look of a graphene structure (left) and visualization of the sp^2 hybridization of carbon orbitals (right).

From the hybridization, 3 sp^2 orbitals are formed in the xy plane creating σ -bonds (covalent) between carbon atoms with the remaining electrons being located in the remaining p_z orbital to create secondary π -bonds. The resulting theoretical electron carrier mobility is greater than $10^5 \text{ cm}^2/\text{Vs}$ at room temperature, well above the electron mobility of copper, gold, and silver which range between $3 - 5 \times 10^3 \text{ cm}^2/\text{Vs}$ [45]. Oostinga et al. [46] demonstrated the tunability of bilayer graphene structures between $1 \times 10^4 - 3 \times 10^4 \text{ cm}^2/\text{Vs}$ through gate voltage tuning. Furthermore, the carbon-carbon covalent bond gives graphene a theoretical Young's modulus of 2.0 TPa. Because of these unique properties, graphene has recently gained traction in semiconductors, electronics, batteries, and composites. Balandin et al. [47] analyzed the thermal conductivity of suspended graphene measuring room temperature values of $4.8 - 5.3 \times 10^3 \text{ W/mK}$ suggesting significantly better thermal conductivity performance than carbon nanotubes. Graphene also has unique optical properties being able to absorb light of any wavelength with an absorption coefficient of $\sim 2.3\%$ per graphene layer [48]. Similar to carbon nanotubes, graphene struggles with bulk implementation due to instability outside the nanoscale currently as a

standalone structure but has gained traction through composite implementation or suspension of graphene in various fluids.

Graphene's electrical and thermal properties are also dictated by layer thickness [49]. Once graphene becomes 10+ layers thick, it becomes graphitic in nature. Graphite is less desirable than graphene in most electronic applications as it has significantly lower electrical ($\sigma > 5000$ S/m), thermal (κ is between 25 – 470 W/mK), and mechanical properties (Young's Modulus = ~36.5 GPa) in comparison [50, 51]. Ideally, monolayered graphene is the preferred structure as monolayered graphene has no gap between the valence and conduction bands, but increasing graphene layers restricts carrier mobility and obstructs these favorable properties [52]. Because of the possibilities of graphene implementation, many methods of fabrication have been developed based on graphene usage.

2.2.2 *Graphene Synthesis Processes*

When developing a system utilizing graphene, it's important to understand the fabrication techniques available to ensure the proper graphene structure is formed. The original "scotch tape" method of creating graphene from graphite is the basis for creating graphene by exfoliation. Because graphene layers within graphite are held weakly together by Van Der Waals forces, exfoliation by mechanical means has been extensively explored and developed since the original method of exfoliation by using scotch tape on graphite takes time and has a low yield of graphene flakes. Narayan et al. [53] developed an exfoliation method using perylene tetracarboxylate as an assisting surfactant for the direct sonication of graphite plates. Graphite flake dimensions ranged between 10 -12 μm and

had a ~30% yield of 2 nm thick graphene sheets and ~8% yield of monolayered graphene. For applications on SU-8 photoresist, Hu et al. [54] developed a graphene exfoliation method by high-temperature pyrolysis. The dominating method for exfoliation is thought to be through the rapid temperature ramp rate and intercalation of gases inside graphite particles. The graphite particles were heated to 1100°C under nitrogen gas and then baked in forming gas (5% H₂ in N₂) for an hour. Scanning electron microscopy (SEM), transmission electron microscopy (TEM), and Raman spectroscopy were used to analyze the resulting graphene flakes.

Another form of graphene deposition is through the decomposition of a precursor material. Common precursors include graphite oxide which can be created using a modified Hummers method [49]. The Hummers method generates graphite oxide by adding potassium permanganate to a solution of graphite, sodium nitrate, and sulfuric acid. The oxide is then reduced by chemical reducing agents such as hydrazine and sodium borohydride; however, by-products of this process are hazardous to both researchers and the environment. For the deposition of graphene directly onto a substrate, Emtsev et al. [55] developed a process for the graphitization of silicon carbide to generate wafer-sized graphene layers. Though the decomposition method of graphene fabrication shows high yield, implementation into a wick structure would be difficult as graphite oxide requires redeposition making the deposition of multiple conformal graphene layers difficult. Furthermore, both reduction and exfoliation methods have low yield rates of monolayer graphene, the most desirable structure.

Chemical vapor deposition (CVD) is another common graphene deposition technique designed around high monolayer graphene yield. There are many types of

chemical vapor deposition available based on processing conditions and substrate material. Typical CVD processes are at high temperatures (~near 1000°C) so enough energy is provided to the reaction to ensure full coverage of graphene. The CVD process typically uses methane gas as the carbon source for the constant growth of graphene grains with an argon purge gas to limit any oxidation. Chemical vapor deposition can occur at various pressures, though low-pressure methods can deposit higher-quality graphene structures. Sharma et al. [56] developed a method utilizing low-pressure chemical vapor deposition for graphene deposition on both copper and Si/SiO₂ substrates. Utilizing a field-effect transistor, the monolayer graphene deposited had a carrier mobility estimated around ~2600 cm²/Vs. The monolayer structure was confirmed using Raman spectroscopy along with Atomic Force Microscopy (AFM). Because the CVD process uses gases for graphene nucleation, the process allows for a fully conformal graphene coating of fully open structures.

2.2.3 *Graphene Foams*

Because of graphene's unique structure and extra degree of freedom compared to CNTs, foams provide a potential shape and network for making 3-dimensional graphene networks a reality. Commercial techniques have already been developed for creating graphene foams with the most common using a metal foam precursor. Graphene is deposited on either a nickel or copper substrate foam using CVD which is then etched away to reveal a self-standing graphene network. Pettes et al. [57] synthesized a 3D graphene foam structure using an open-cell nickel foam. Through joule heating analysis, the pure graphene foam had a thermal conductivity between 0.26 – 2.28 W/mK increasing with density. Loeblein et al. [58] fabricated a high-density 3D graphene foam using a similar

method of chemical vapor deposition on a nickel foam of pore sizes between 100 – 200 μm . Densities between 5 – 450 mg/cm^3 achieved thermal conductivities between 0.02 – 86 W/mK using laser flash analysis (LFA). Electrical conductivity measurements were also made though results show conductivities (59 S/m) significantly lower than that of copper. Imaging of the foam utilized both optical and SEM methods and is shown in Figure 13.

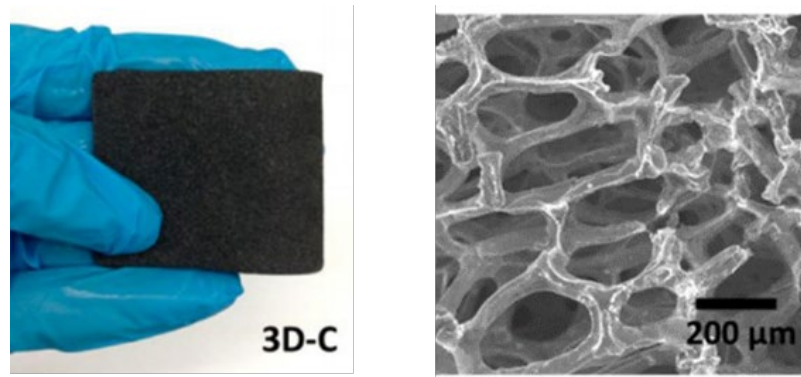


Figure 13 – Optical image (left) and SEM image (right) of graphene foam wick [58].

The SEM image shows a fully connected graphene structure with a small number of ligament breakages. These breakages could have been from incomplete coverage of graphene on the original foam or mechanical breaking during post-processing and analysis. Other methods of graphene fabrication include self-assembled networks using polymer assistance. Chen et al. [59] demonstrated the assembly of connected graphene oxide hollow spheres with ultra-low densities and sub-10 micron pore sizes. The graphene spheres were formed through the trapping of graphene oxide sheets between water/toluene interfaces and stabilizing Pickering emulsions with PVA. Graphene foam fabrication through self-assembly methods includes fabrication done by Zhang et al. [60] where graphene oxide suspensions were reduced by L-ascorbic acid and HI and then heat treated in hydrazine hydrate. The resulting compressive strength of the foam was 320 kPa with an electrical

conductivity of 20.6 S/m. Sha et al. [61] integrated 3D printing technology into graphene foam creation by using a Ni/sucrose mixture in a metal powder printing technique. The printed graphene foams had an ultra-high porosity of 99.3% with an electrical conductivity of 870 S/m; however, the foam was reported to have multilayer graphene features from the sucrose printing process. Similarly, Azhari et al. [62] additively manufactured graphene-hydroxyapatite nanostructures using a mixture of graphene oxide and hydroxyapatite. Average porosities achieved were around 50% with maximum compressive strengths of 0.25 – 0.55 MPa when 3D printing samples of 100 μm . Further data and properties of other three-dimensional graphene foam structures are shown in Table 3. From literature analysis, graphene foams - developed through chemical vapor deposition on metal foams and then etching of the precursor - were originally selected for a baseline of the composite structure.

Table 3 – Graphene foam properties from literature.

Ref.	Name	Structure	Thermal		Electrical		Mechanical		
		ρ [mg/cm ³]	K [W/mK]	Test	σ [S/m]	Test	E [MPa]	Y _s [kPa]	Test
[57]	Graphene-Based Foam	9.6 - 32	0.26 - 2.28	Joule Heating	-	-	-	-	-
[58]	High-Density 3D-Graphene	5 - 450	0.02 - 86	Laser Flash	59	van der Pauw	-	-	-
[63]	Mitsubishi ARA24 Foam	220 - 570	50 - 150	Laser Flash	-	-	-	-	-
	Conoco Dry Mesophase Foam	330 - 590	40 - 135	Laser Flash	-	-	-	-	-
[64]	3D Graphene Foam	5	-	-	-	-	339	-	Uniaxial tensile
[65]	3D Graphene Foam	4	-	-	-	-	0.013	-	Uniaxial Compression
[66]	Graphene Foams	4 - 32	-	-	-	-	0.016 - 0.418	-	Uniaxial Compression
[67]	Three-Dimensional Graphene Networks	5	-	-	700	Two-Probe	-	-	-
[59]	Hollow Graphene Spheres	0.002 - 0.1	-	-	54	-	-	-	-
[68]	Self-Assembled Graphene Hydrogel	-	-	-	0.023 - 0.49	Two-Probe	0.029 - 0.29	3 - 24	Uniaxial Compression
[60]	Graphene Foam by Self-Assembly	14.7	-	-	20.6	Four-Probe	-	320	Uniaxial Compression
[61]	3D Printed Graphene Foams	15	-	-	870	Two-Probe	-	-	Dynamic Mechanical Analysis
[62]	3D Printed Graphene Foam	1.196-1.266	-	-	-	-	1 - 3	-	Uniaxial Compression

2.3 Preliminary Tested Graphene Foams

Originally, graphene foams were chosen as a new base material system for implementation in high-performance, high-heat flux vapor chamber applications and were characterized courtesy of previous Georgia Tech student Ryan Wong. The graphene foams were commercially purchased from the MTI corporation and were fabricated by the chemical vapor deposition of graphene on a nickel precursor foam which was then etched away. These foams were specifically designed for lithium-air battery research with ultra-low density ($\rho = 4 \text{ mg/cm}^3$) and were not optimized for wick application by the company. Structural, thermal, and mechanical analysis was performed to analyze if the foams were a viable backbone implementation as a vapor chamber wick. However, initial SEM imaging of the foams indicated that these foams had a significant defect in the connected foam network which is shown in Figure 14.

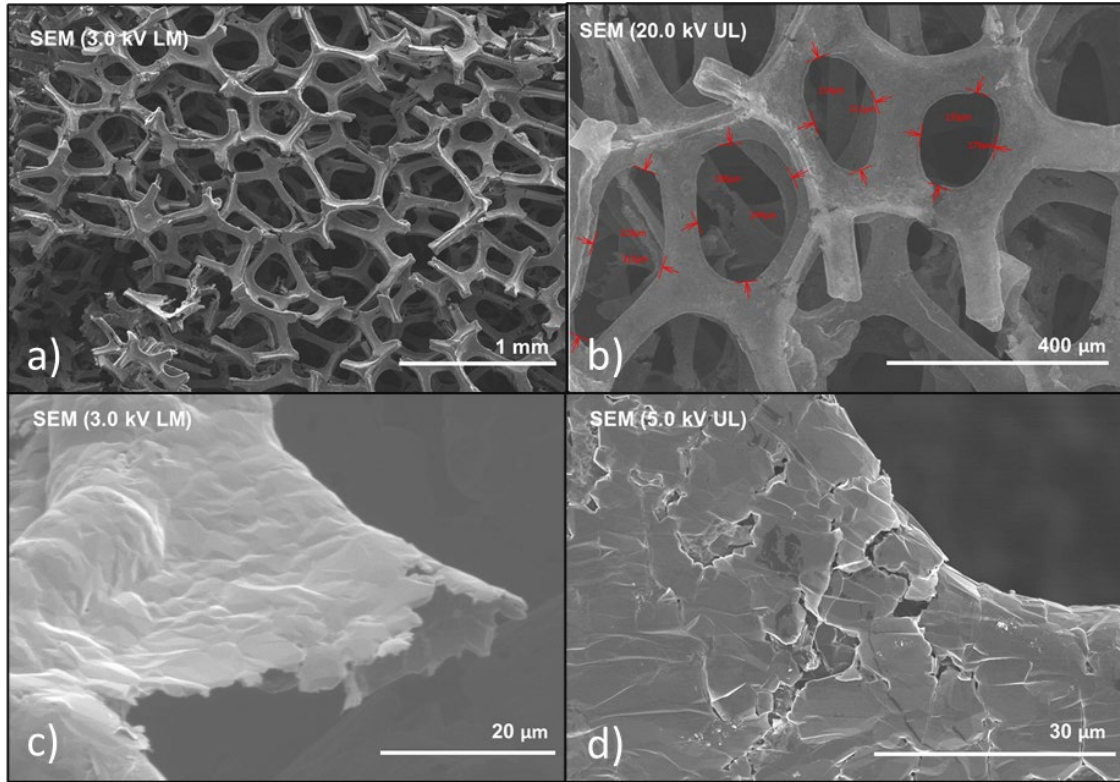


Figure 14 – SEM imaging of commercially available graphene foams at a) x35, b) x130, c) x2.00k, and d) 1.80k magnifications.

From the SEM analysis in Figure 14a, a high number of fractured ligaments can be seen throughout the foam indicating a low degree of connectivity. Figure 14c analyzes these ligaments showing a clean fracture of a node before any testing had begun. Furthermore, Figure 14d shows microfractures between grains on the graphene surface. Nieto et al. [64] similarly analyzed the deformation mechanisms of 3D graphene foams and demonstrated that discontinuous graphene sheets can cause premature failure of the foam as the number of load-bearing branches is low. Mechanical analysis of the commercial foams was performed and showed mechanical strengths (yield strength < 2.0 kPa) well below the desired values for composite fabrication confirming the effect of discontinuities on the properties of the foam. Further analysis of the quality of the

commercially purchased graphene foam was performed using Raman spectroscopy which indicated the graphene was more graphitic in nature than few-layer graphene as the ratio of 2D peak intensity to G peak intensity was 0.5. The results from the Raman spectroscopy are shown in Figure 15.

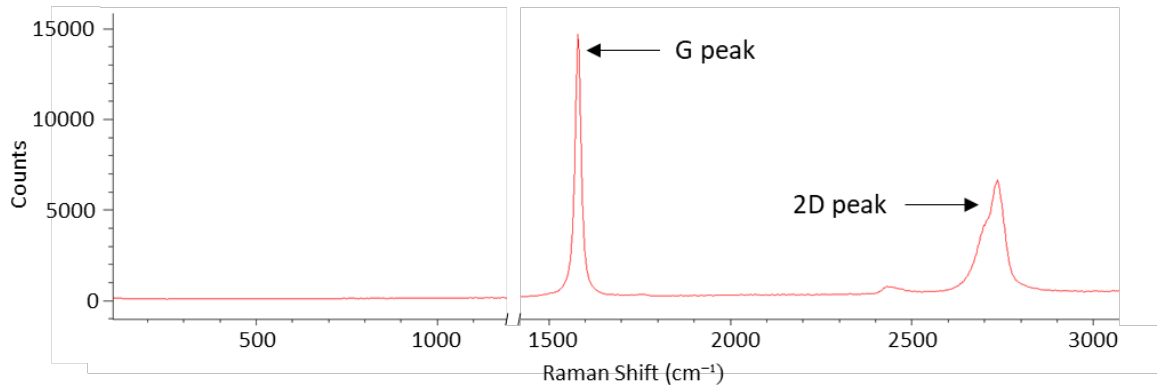


Figure 15 – Raman spectroscopy of commercial 3D graphene foams.

Thermal analysis was also performed on the base graphene foams using an LFA. Results from the tests show that the thermal diffusivity of the graphene foams was around .09 mm²/s at room temperature with thermal conductivities below < 2 W/mK, lower than thermal conductivities seen in other wick systems. The low material content of these graphene foams heavily contributes to the low thermal characteristics of the foam wicks.

From initial screening and testing, it was found that the graphene foam would not be a suitable starting material for the implementation into high-performance vapor chamber systems due to the low material content, graphene quality, and poor thermal and mechanical properties. To improve the capabilities of vapor chamber wicks over copper wicks, other routes of material development had to be reviewed.

2.4 Copper-Graphene Composites

Copper-graphene composite literature was analyzed to understand different methods of adding graphene into the copper matrix or system and characterizing them as well as to understand the property improvements. Jagannadham et al. [69] developed a process for fabricating a multilayer copper-graphene composite by chemically exfoliating graphene oxide onto a copper substrate. A secondary copper layer was deposited through laser physical vapor deposition to create a copper-graphene oxide composite layer. The layer was then placed in a flowing hydrogen environment at 400°C to reduce any oxides. The thermal conductivities of the composite layers were found to be 150 W/mK at 300K, lower than the copper substrate's thermal conductivity of 420 W/mK at 300K. Kim et al. [70] also developed multilayer copper-graphene specimens focusing on thin, monolayer graphene when forming their nanopillar specimens. The graphene was deposited through CVD but removed from the initial substrate for sequential stacking on other substrates. After a certain number of layers, nanopillars were cut perpendicular to the plane of the sheets. The resulting nanopillars showed significant improvements in compressive strength compared to single, bulk crystal metals achieving yield strengths of 1.5 GPa for copper-graphene composites and 4.0 GPa for nickel-graphene composites [70]. Other common methods for creating copper-graphene composites include the sintering of graphene-coated copper particles. Chu et al. [12] fabricated copper-graphene composites with in-plane thermal conductivities as high as 458 W/mK – roughly 20% higher than bulk copper – through spark plasma sintering of copper particles mixed with graphene sheets. Wejrzanowski et al. [71] analyzed both the numerical and experimental results of variously ordered graphene sheets in a copper-graphene composite matrix. Data suggested that when

graphene is aligned in layers, the thermal conductivity of the material is anisotropic, with higher thermal conductivities measured parallel to the graphene plane. On the other hand, when graphene is randomly ordered in the copper matrix, thermal conductivity may decrease with added graphene quantities. Lamellar composites were created through spark plasma sintering and measured thermal conductivities of 352 W/mK. Wang et al. [72] demonstrated the strengthening efficiency of reinforcing the copper matrix with reduced graphene oxide. Through the process, yield strengths of 395 MPa – 501 MPa were achieved; however, the highest improvement was seen at 2.4 vol% reduced graphene oxide compared to the maximum of 4.8 vol%. Due to the cost of fabricating monolayer/few-layer graphene, some copper-graphene composites use graphene nanoplatelets (10 – 30 layers) instead [73]. Further copper-graphene composites are documented in Table 4. Due to the promising nature of the literature and previous work on pure graphene foam, copper-graphene systems were identified as a potential route for wick material development; however, wick geometries make graphene implementation into the copper matrix difficult, so graphene coatings were explored to combine graphene's excellent thermal, electrical, and mechanical capabilities with the high material content and structural backbone of a copper foam.

Table 4 – State-of-the-art copper graphene composite properties.

Ref.	Title	Electrical	Thermal		Mechanical	
		σ [%IACS]	α [mm ² /s]	κ [W/mK]	E [GPa]	Y [MPa]
[69]	Cu-Gr multilayer film	–	–	150	–	–
[70]	Metal-Gr nanolayered composite	–	–	–	–	1500
[12]	Sintered Cu-Gr composite w/ aligned Gr	–	–	458	–	–
[71]	Sintered Cu-Gr composite	–	–	352	–	–
[72]	Reduced GRO-reinforced Cu matrix composite	–	–	–	–	395 - 501
[74]	Cu-Gr metal matrix composite through impregnation	–	–	–	109	308
[75]	Gr-nanoplatelet-reinforced copper matrix	~84%	86	–	–	470
[76]	Hot-press processing of Gr-Cu composites	–	–	–	~105	~320
[77]	Electroplated Cu-Gr thin film composite	~89.6%	–	–	123	–
[78]	Cu-Gr composite by SPS diffusion bonding	108.60%	–	–	–	–
[79]	Sintered Cu-Gr composite	84 - 94%	–	–	–	–
[80]	Ultra-high strength Cu-Gr composite	–	–	–	–	608
[81]	Gr reinforced Cu composite	61 - 63%	–	–	–	–
[82]	Freeze Dried and SPS GRO/Cu composite	–	–	–	–	109.4 - 121.2

2.4.1 Graphene Coatings

Recently, graphene has been used as both a protective coating and property-improving material because of graphene's conformal nature and chemical stability. Singh Raman et al. [83] used low-pressure chemical vapor deposition to deposit graphene onto pure copper substrate strips for protection of the copper from electrochemical degradation. Using 0.1 M sodium chloride solution, corrosion tests of the copper-graphene electrode strips were performed. Immersion during the test totaled 1 hr and showed significant discoloration on pure copper electrodes while the graphene-coated samples maintained the original coloration and graphene coating. Electrolytic resistance measurements were performed showing similar measurements for pore resistance between both the graphene-copper and pure copper samples, as well as significantly higher metal/electrolyte interface resistance for the graphene-copper ($6.05 \times 10^5 \Omega\text{cm}^2$) compared to pure copper ($3.8 \times 10^3 \Omega\text{cm}^2$). Similarly, Chen et al. [84] investigated graphene coatings for the oxidation resistance of copper and copper/nickel alloys. Base metal samples and graphene-coated samples were put under annealing conditions while exposed to the area to analyze the growth of oxides using SEM, Raman, and X-ray photoelectron spectroscopy (XPS). Outside of chemical protection, graphene coatings have been shown to have significant impacts on composite properties as well. Xu et al. [68] tested graphene composite coatings on SiC diodes and found the junction temperature lowered by 10°C and the thermal resistance reduced by 16.7%. Both results indicate graphene as a potential pathway for better heat dispersion. From another perspective, Rafiee et al. [85] demonstrated the wetting transparency of few-layer graphene coatings. The surface tension analysis of graphene on copper showed that the wettability only begins to transition to that of graphite

when 6+ graphene layers are reached. Silicon and gold substrates were also used to show graphene's wettability phenomenon. Furthermore, their study showed increased condensation heat transfer of 30 – 40% on copper from the oxidation suppression of graphene on copper without compromising the copper's high wettability. As graphene coatings presented themselves as not only an important tool for better electrical and thermal performance, but also demonstrating oxide-growth inhibition, corrosion resistance, and wetting transparency, they were selected as an effective pathway for increased foam wick properties in high-performance, high-heat flux vapor chamber applications.

2.5 Characterization Methodology

Before the development of the coated foam material system, characterization methods were chosen that would accurately demonstrate the improvements of each deposited layer. These characterization methods were chosen based on commonly used methods in the literature, compatibility with the nature of the foams, and availability.

2.5.1 Surface And Structure Analysis

For foam characterization, surface and structural analysis is the basis for confirming and understanding the deposition methods utilized. Scanning electron microscopy is a vital tool for understanding surface structure formation. SEM analysis uses an electron beam to excite the electrons in the sample material. These excited electrons release both secondary electrons and backscattering electrons, each providing use in material analysis. The typical low-magnification and high-magnification microscopy done with SEM collects the secondary electrons released from excitation to show high-resolution images at a much higher magnification than optical imaging. Secondary electrons are also low energy, so the depth

of penetration is moderately shallow (few nanometers) compared to other high-energy techniques when using low voltage and emission currents. Also, SEM electron beams are highly narrow giving the imaging technique a high depth of field. Since SEMs utilize an electron beam for analysis, analyzed samples must be electrically conductive to prevent charging which is not a problem for highly conductive copper-graphene composites. The electron excitation also produces X-rays that can be characterized through energy-dispersive X-ray spectroscopy (EDS). These X-rays are produced when a higher energy electron from an outer orbital fills a hole created during excitation from the electron beam. The excess energy from the migrating electron is emitted as an X-ray which is then collected and converted to voltage signals. Most elements have uniquely identifiable X-ray emission peaks though there is some overlap. EDS analysis has a greater penetration depth than secondary electron SEM analysis making characterization difficult for thin-layer graphene structures. Furthermore, EDS also picks up signals from carbon and oxygen atoms in the atmosphere even at low pressures making exact volume and weight fraction measurements unreliable; however, EDS is a good technique for structure identification during the electroless process to understand if there is a high presence of oxides or foreign elements from deposition solutions. Both these techniques are non-destructive to the copper-graphene sample.

Raman spectroscopy is another vital tool used for copper-graphene composite analysis. Raman spectroscopy analyses the Raman shift of a laser's energy due to interactions with a material's molecular vibrations. Due to the simplicity of graphene's structure, Raman analysis can easily identify graphene and its structural properties. There are three important Raman peaks to focus on when analyzing graphene: the D peak (~1350

cm^{-1}), the G peak ($\sim 1580 \text{ cm}^{-1}$), and the 2D peak ($\sim 2700 \text{ cm}^{-1}$). The D peak is associated with the organization of the carbon ring. The higher disorder will be shown by an intense D peak. An ideal, large monolayer graphene grain will have no D peak presence during Raman analysis. Monolayer graphene is identified and characterized by a thin, intense 2D peak and a lower-intensity G peak. As more layers are applied, the 2D peak widens while the G peak gains intensity. The ratio of the intensity of the 2D peak vs. the G peak should be greater than 1 to confirm mono- to few-layer graphene. The widening of the 2D peak from monolayer graphene to graphite is also shown in Figure 16 [44].

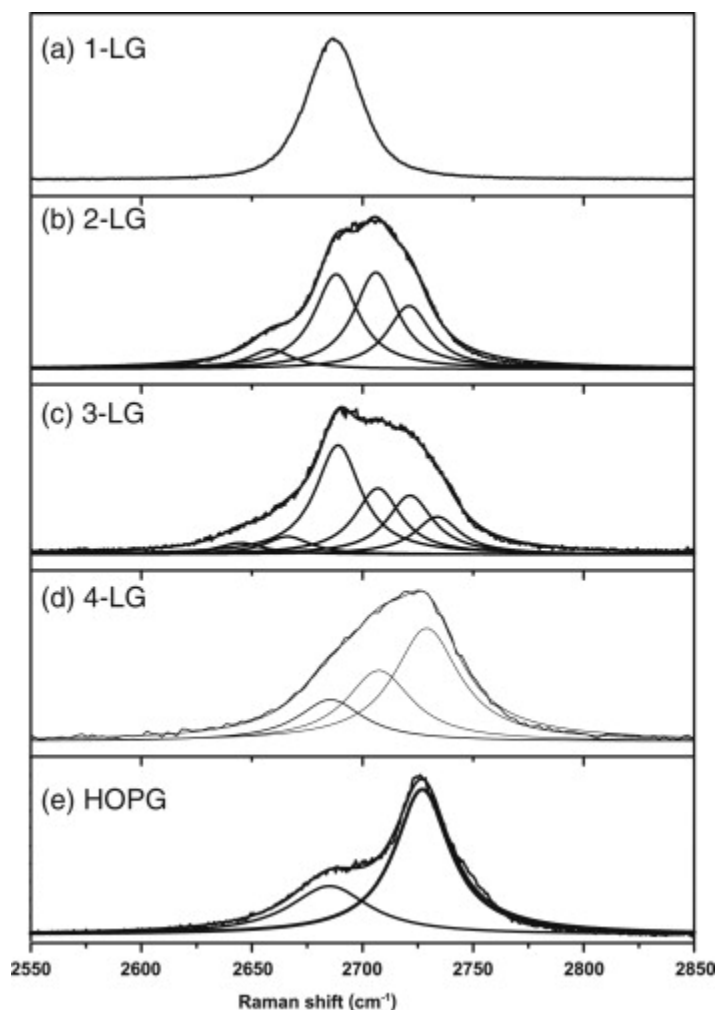


Figure 16 – Raman spectra of graphene with differing numbers of layers (L) and highly oriented pyrolytic graphite (HOPG) [44].

Because Raman scattering relies on a change in polarizability with molecular vibration, metals do not present Raman spectra, meaning the presence of copper will not disrupt the graphene spectrums analyzed. On the other hand, Raman spectroscopy can analyze the presence of oxides and foreign substances created from deposition along with EDS; however, the Raman shift for copper oxides ($\text{sub-}500 \text{ cm}^{-1}$) is much lower than the graphene peaks making them easily distinguishable. Also, as the source for Raman spectroscopy is light, there is no penetration of the laser into the sample making it a surface-

level characterization method. Furthermore, as copper and graphene are excellent thermal conductors, the high-intensity laser will not damage the surface of the samples.

2.5.2 *Thermal Conductivity Analysis*

Thermal analysis of the graphene-copper foams will be performed using laser flash analysis and simultaneous thermal analysis (STA). Laser flash analysis uses an infrared source to “flash” a material sample face and which is then absorbed into the material as heat. The heat then diffuses through the material, and the infrared signature is picked up on the other side. The time it takes for the thermal energy to travel through is recorded as the thermal diffusivity (α , mm²/s) of the material. Thermal diffusivity is an important property for heat-spreading materials and is also a component in calculating the thermal conductivity of a material [86]. As the time it takes heat to travel through a sample is dependent on the distance traveled, the thickness of the sample must be concisely recorded for accurate thermal diffusivity. Certain LFA machines can heat the sample as well allowing for the characterization of the material over increasing temperatures. STA couples the thermal characterization methods of thermogravimetric analysis (TGA) with differential scanning calorimetry (DSC). TGA is a thermoanalytical tool that measures the mass or weight of the sample over increasing temperatures [87]. DSC, on the other hand, measures the heat flow of the sample over a temperature range and is a vital tool for measuring material phenomena such as recrystallization and melting temperatures [88]. Coupling the two thermal analysis techniques allows an STA to measure the specific heat (or heat capacity, c_p , J/gK) of a material. The thermal conductivity (κ , W/mK) of the material can then be calculated using the relationship in Equation 1.

$$\alpha = \frac{\kappa}{c_p \times \rho_{Cu} \times \rho^*} \quad (1)$$

2.5.3 Electrical Conductivity Analysis

Electrical analysis is a valuable tool for the characterization of the foam as it correlates well to the other improving properties of the composite in a time-efficient manner as well as possible insight into the future necessity of sending signals and using the two-phase heat spreader for electrical wiring. Two common methods for the analysis of the electrical properties of topologically irregular structures are the van der Pauw method and the four-point probe method [60]. Both methods utilize four probes placed on the sample where two analyze the voltage and the others analyze the current. Electrical resistivity (ρ_e , Ω) and sheet resistivity (ρ_s , Ω/\square) can be calculated with the recorded information [89]. The electrical conductivity (σ , \bar{U} or S) of the sample is then calculated using the relationship with sheet resistance shown in Equation 2.

$$\sigma = \frac{1}{\rho_s * t} \quad (2)$$

Van der Pauw differs to four-point probe in where the pins are located. When using van der Pauw, the pins are located on the perimeter of the sample to record an average resistivity. In a four-point probe tool, the probes are equally spaced in a line and analyze the resistivity in the direction of the probes.

2.5.4 Mechanical Analysis

Uniaxial mechanical testing is a common methodology for analyzing the mechanical properties of a foam [60]. Foam materials can vary in mechanical properties

based on whether the foam is under tensile or compression loads. In a vapor chamber environment, if the wick is used for helping the structural integrity of the system, it can be subjected to both tensile and compressive stresses during both fabrication (pulling vacuum and charging the system with working fluid) and operation (constant pressure change with the changing of working fluid phases). Using uniaxial mechanical testing, important mechanical properties can be obtained such as a material's Young's modulus, yield strength, ultimate tensile strength, and relative toughness. As the cross-sectional area of the foam is composed of disconnected nodes, a definitive fracture strength cannot be obtained through testing. The various property testing methods used for evaluating foam performance are shown in Figure 17.

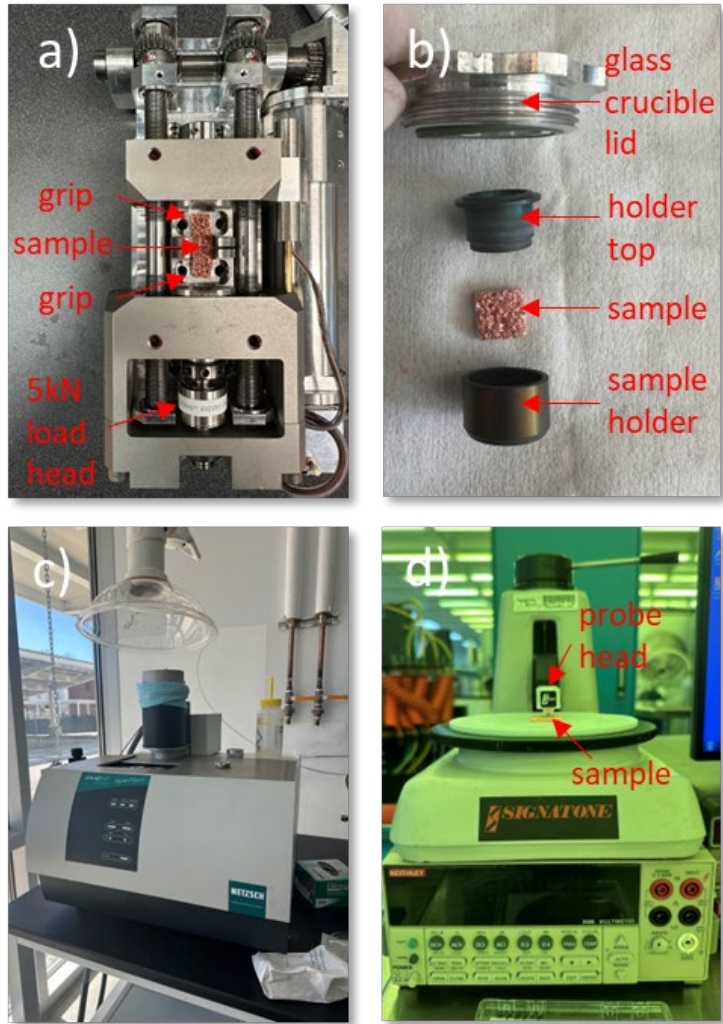


Figure 17 – Property characterization methods used to evaluate foams: a) uniaxial testing set-up and tool, b) laser flash analysis setup, c) laser flash tool, and d) four-point probe set-up and tool.

CHAPTER 3. SINGLE-LAYER GRAPHENE COATINGS

3.1 Acquisition Of Baseline Cu Foams

For the development of the graphene-coated copper Pure copper foams were purchased from ERG Aerospace and their baseline structure and properties were characterized. Four foam types of varying relative densities (ρ^*) were acquired based on pores per inch (PPI) and density: 40PPI uncompressed ($8 - 12\% \rho^*$), 40PPI 2x compressed ($19 - 23\% \rho^*$), 20 PPI uncompressed ($8 - 12\% \rho^*$), and 20 PPI 2x compressed ($17 - 22\% \rho^*$). The compressed foams were fabricated through the mechanical compression of their uncompressed PPI counterparts. Note that the compressed foam samples underwent more than one compressive test, and are marked as two times compressed (2x), etc. Post-cast compression increases the relative density of the samples but may be detrimental to other properties, e.g., connectivity. The relative density of the foams was calculated using the relationship shown in equation 3 where V is volume, m is mass, and the density of copper is ρ_{Cu} .

$$\rho^* = \frac{m}{V \cdot \rho_{Cu}} \quad (3)$$

The volume of the foams was calculated through length, width, and height measurements by calipers and the mass was measured using a scale. All foams purchased have their relative densities measured as the relative density has a significant effect on the overall foam properties. The average relative densities of the 4 foam types are displayed in Table 5.

Table 5 – Relative density averages of the 4 copper foam types chosen for the development of the graphene-coating.

	40 PPI Uncompressed	40 PPI 2x Compressed	20 PPI Uncompressed	20 PPI 2x Compressed
ρ^* [%]	9.5 ± 1.5	21.0 ± 0.8	10.2 ± 1.2	19.4 ± 1.7

The high-density foam types have twice the relative density as their low-density counterparts due to the compression process. To understand the effect of the compression on the connectivity and structure of the pure copper foams, as well as to characterize key microstructural features that will affect properties, optical analysis was performed to measure the average pore – displayed in Figure 18 – and ligament sizes while SEM analysis was performed to measure nodal connectivity based on the number of ligaments per node. At least 20 ligament and pore measurements were made for each foam type.

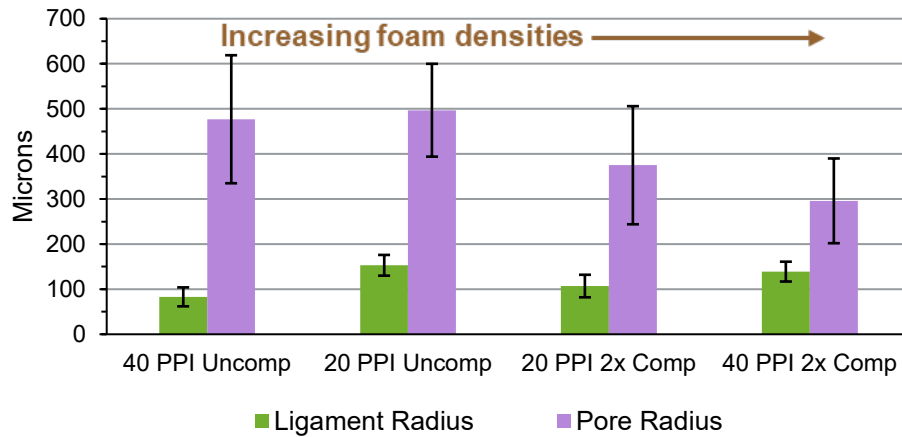


Figure 18 – Pore and ligament sizes based on foam type.

As expected, there is a decreasing average pore size with increasing relative density due to the compression process. Ligament sizes were unaffected by the densification of the foams. For connectivity evaluation, the ligaments per node were individually counted and

averaged over multiple foams of the same type. The results of both the optical microscopy and SEM analysis are in Table 6, while the SEM characterization is presented in Figure 19.

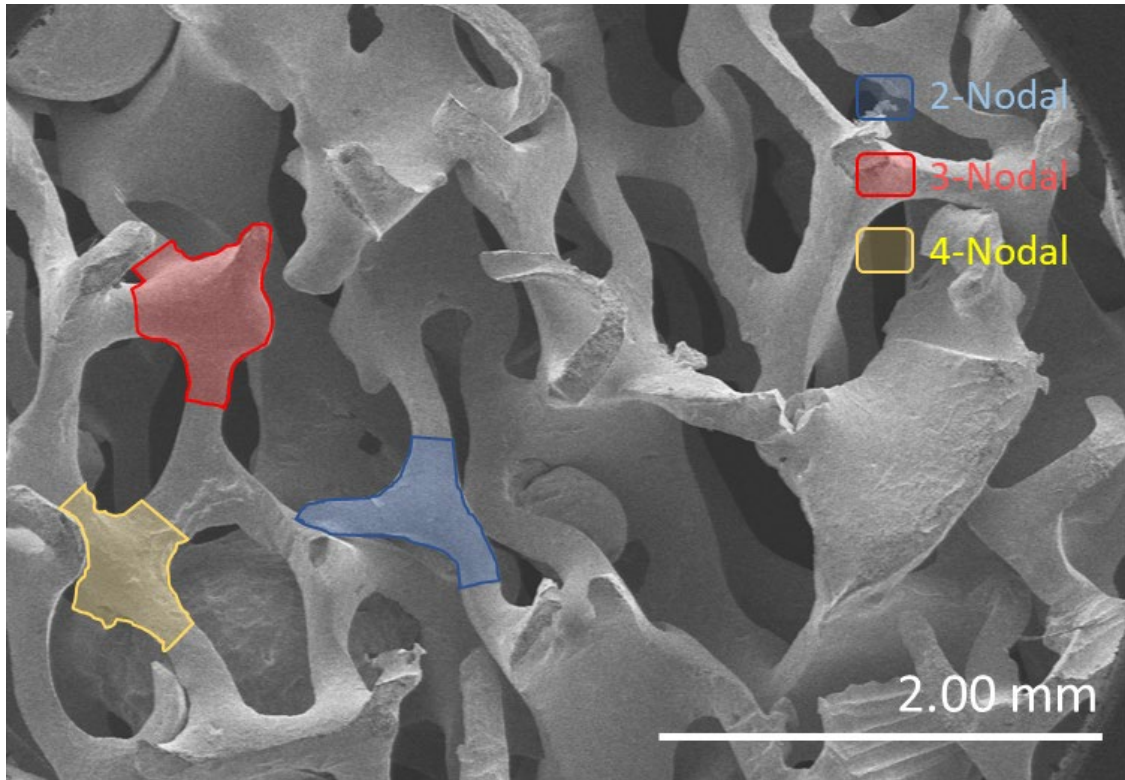


Figure 19 – SEM imaging of 40 PPI 2x compressed copper foam showing nodes with 2, 3, and 4 connections.

For the connectivity analysis, the number of ligaments per node was counted where a 4-nodal ligament indicated high connectivity while 2-nodal ligaments indicated low connectivity or breakage of ligaments. From the compression, the 2x compressed foams also showed a higher percentage of 2-nodal ligaments compared to the uncompressed foams indicating lower connectivity of the foam network as indicated in Figure 20.

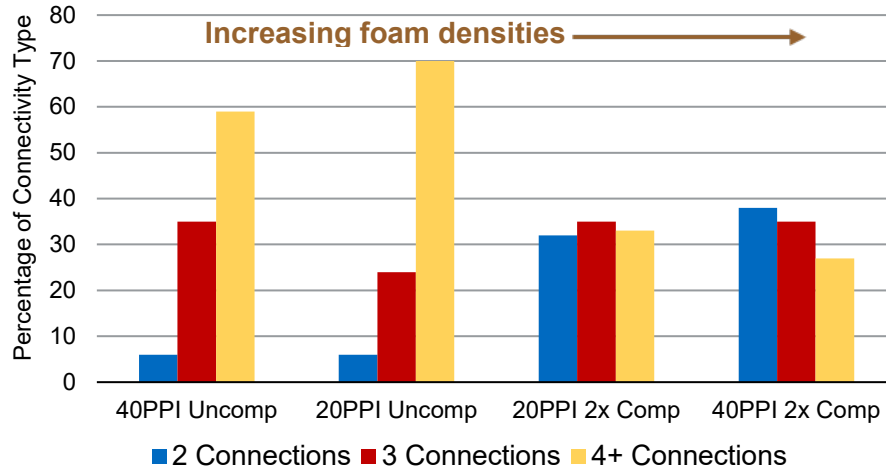


Figure 20 – Connectivity of the selected foam types.

The decreased connectivity of the high-density foams is due to ligament fracture/collapse from compression during post-processing. So, while the compression process does increase the relative density of the foam, it is at the expense of ligament connectivity. Though both low-density foam types have similar relative densities, the 20 PPI uncompressed foams showed the highest connectivity of the foams with 70% of the foam nodes having 4 or more connections.

Table 6 – Structural properties of baseline pure copper foams.

Foam [Description]	ρ^* [%]	Ligament Rad. [μm]	Pore Rad. [μm]	% of Node		
				4-Nodal+	3-Nodal [%]	2-Nodal
40 PPI Uncompressed	9.5 ± 1.5	83 ± 21	477 ± 142	59	35	6
40 PPI 2 \times Compressed	21.0 ± 0.8	107 ± 22	296 ± 94	27	35	38
20 PPI Uncompressed	10.2 ± 1.2	153 ± 23	497 ± 103	70	24	6
20 PPI 2 \times Compressed	19.4 ± 1.7	139 ± 25	375 ± 131	33	35	32

After the characterization of the base copper foam structure, the foams were then ready for the deposition of the graphene coating.

3.2 Low-Pressure Chemical Vapor Deposition

For the deposition of the single-layer graphene-coating, low-pressure chemical vapor deposition (LPCVD) was selected due to its high yield of monolayer graphene. The deposition method facilitates the synthesis of monolayer graphene with uniform thickness without any anisotropic effects. As the name suggests, LPCVD is a deposition process that occurs in high vacuum environments ($< 10^{-6}$ torr). The sample is placed on a graphite stage which is then inserted into a quartz furnace chamber. The process takes place at $\sim 1000^{\circ}\text{C}$ with a ramp rate of $150^{\circ}\text{C}/\text{min}$ in an argon atmosphere. Once 1000°C is reached, methane and hydrogen gases are then pumped into the chamber. While argon gas serves to prevent oxide growth on the graphene surface, methane is used as the carbon supply for graphene growth, and hydrogen is used for reducing the copper surface at high temperatures. Graphene deposition occurs in a 6-step surface reaction by diffusion of methane particles through the boundary layer to the substrate surface, absorption into the substrate, decomposition to form carbon and hydrogen, diffusion back to the surface, and desorption of the inactive hydrogens from the surface [90]. Previous studies have shown that, during the CVD process, graphene on the surface is much more stable than its single-carbon atom constituent. For this reason, the low availability of atomic carbon limits graphene growth solely to the surface of the copper substrate [91]. Furthermore, there is a boundary layer of stagnant thickness on the surface of the copper substrate due to the steady state gas flow during the CVD process that further promotes ideal graphene growth conditions. While atmospheric pressure chemical vapor deposition has a boundary layer with low diffusion

rates making it the rate-limiting steady for deposition at the low pressures of LPCVD significantly increases the diffusion rate at the boundary layer [90]. This makes the surface reaction regime the rate-limiting step which ensures that, as long as there is a uniform temperature of the substrate, there should be a uniform graphene thickness. LPCVD growth of graphene also shows self-limiting kinetics during graphene growth ensuring the growth of mostly mono/bilayer graphene [90]. The growth period for the graphene is 30 minutes, and the chamber is then cooled back to room temperature at a variable rate under the convection of argon purge gas.

3.3 Surface Analysis & Verification

To verify the presence and quality of the graphene layer on the topologically irregular foam, SEM analysis and Raman spectroscopy were used to characterize the deposited graphene as described below.

3.3.1 SEM Analysis Of Single-Layer Graphene Coating

Scanning electron microscopy can be used to analyze the presence of graphene on the copper surfaces as well as possible graphene grain size and overlapping graphene sheets. The SEM voltages used for analysis were 2.5 kV – 10 kV with accelerating voltages of 5 – 10 A. Lower voltages were used for direct graphene analysis due to the lower penetration of the electron beam. Graphene is identifiable on a copper surface by looking for “wrinkles” throughout the foam. The surface of the single-layer graphene foam coatings under an SEM is shown in Figure 21.

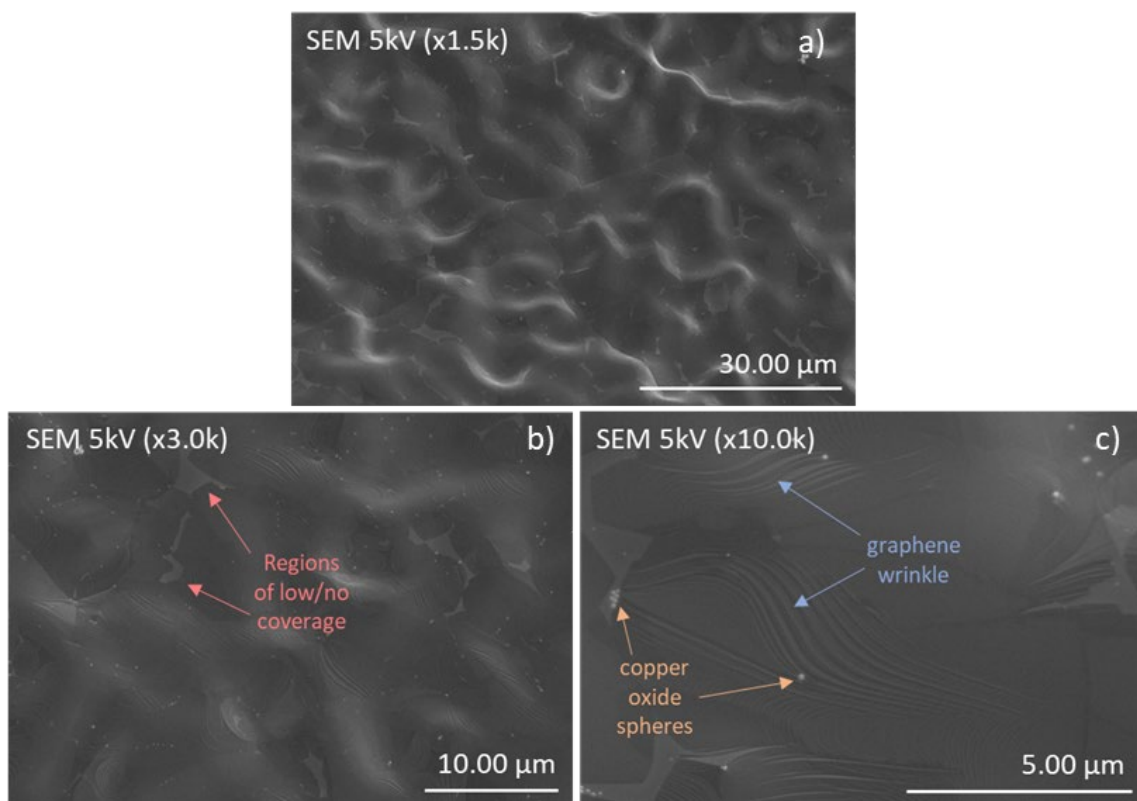


Figure 21 – SEM imaging of Gr-coating Cu foams at a) x1.5k, b) x3.0k, and c) x10.0k.

Graphene wrinkles on the surface are sub-micron in size and can only be used to confirm the presence of graphene on the surface, not the quality. Due to the local topology of the foams, darker regions (bi/tri-layer) and light regions (no/low coverage) can be seen at higher magnifications ($> x5.0k$). Singular copper oxides and copper oxide clusters are shown on the surface of the graphene layers after deposition but can be removed during the cleaning of the foam. After verification of the complete coverage of graphene on the copper foam surface, Raman analysis was then performed to evaluate the quality of the graphene coating.

3.3.2 Raman Spectroscopy Of Single-Layer Graphene Coating

As previously mentioned, Raman spectroscopy is a valuable tool for analyzing graphene quality due to the unique Raman spectra of monolayer graphene. For characterization, a 488 nm wavelength was used. The Raman spectrum recorded from the analysis of the graphene grown on the surface of the copper foams is shown in Figure 22. Every graphene-coated foam is checked during both fabrication and testing, and all show the same peak intensities for the single-layer samples.

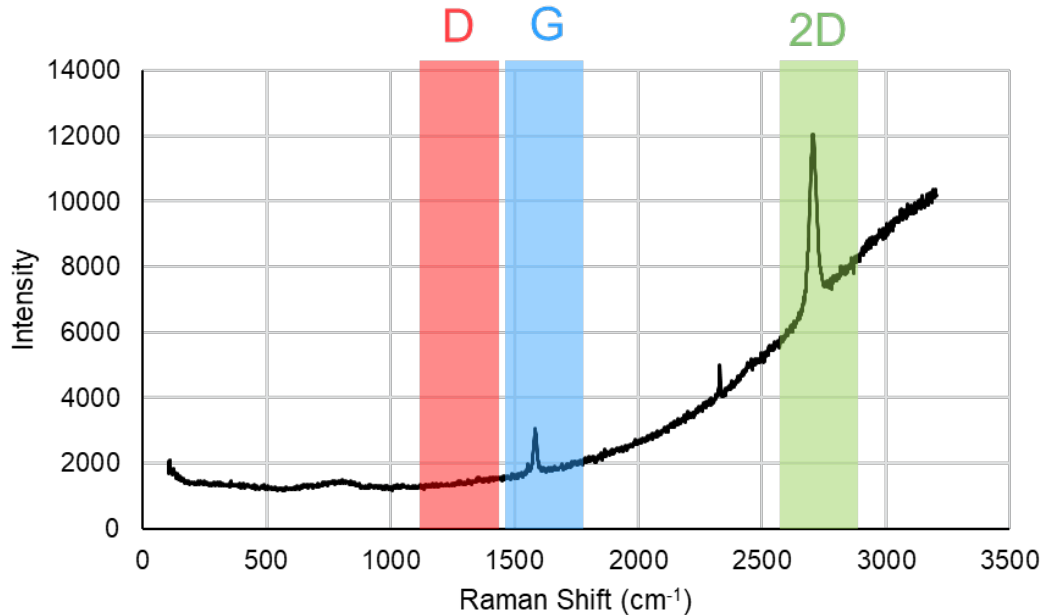


Figure 22 – Raman spectroscopy of Gr-coating on a 40 PPI uncompressed copper foam.

From Raman analysis of the graphene, the 2D peak shows a high intensity over the G peak. These peak intensities indicate the presence of the desired monolayer graphene structure. Furthermore, the D peak has no prominence meaning the graphene grains are well connected with low amounts of dislocations and disconnections of the graphene

network. Through Raman analysis on all copper foam structure types, similar Raman spectra were obtained indicating the graphene deposition process is unaffected by the present variable pore sizes.

3.4 Wick Wettability, Permeability, And Capillary Performance With Gr-Coating

For the evaluation of how the graphene coating affects the copper foam wick, tests that evaluated wettability, capillary pressures, and permeability were performed. To confirm the wetting transparency of the graphene outer layer coating, optical wettability tests were performed using a contact angle measurement system. Due to the geometry of the foam structure, contact angle measurements are difficult to accurately measure so the wettability was analyzed on a copper sheet. The graphene layer was deposited onto copper sheets using the same CVD process, and the working fluids tested for comparison were DI water and OpticoolA. DI water was selected due to its availability, chemical inertness, and well-understood wettability on copper systems. OpticoolA, on the other hand, is a chemically inert, low-viscosity, dielectric fluid that could be used for vapor chamber implementation in the future when the vapor chamber will be used as a structure for electrical real estate. Figure 23 shows the results of the contact angle study on both copper and Gr-coated copper foils. The averages are based on over 100 data points for each test and are done at multiple locations on the graphene-coated copper sheets. The variation of the contact angle is around 0.5° for a single location set and 1.5° for different copper sheets. Under both working fluids, the graphene-coated copper foil demonstrated the same contact angle as the copper foil indicating that the graphene did not affect the underlying copper's wettability.

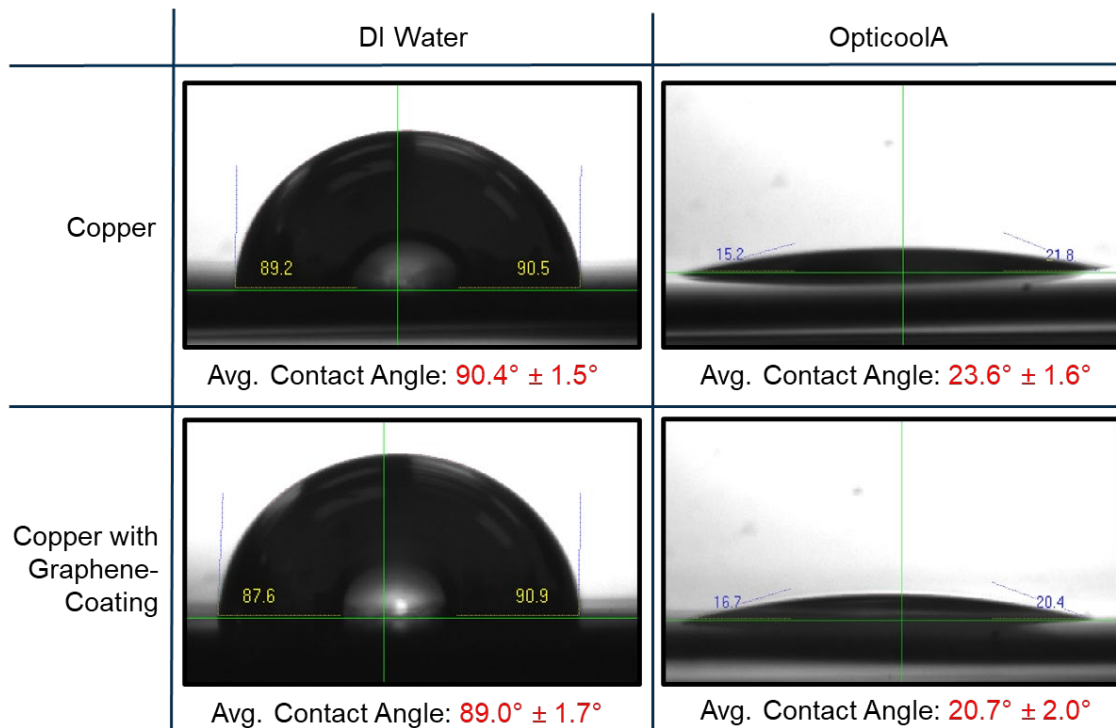


Figure 23 – Contact angle measurements of Cu vs Gr-coated copper using water and OpticoolA.

The results from the contact angle measurement tests verify the wetting transparency properties of monolayer/few-layer graphene-coated copper. Furthermore, there was a slight increase in the wettability of the materials system when OpticoolA was used as the working fluid which could indicate that other, oil-based working fluids could be tested further for better compatibility with graphene-coated copper systems. After demonstrating that the monolayer graphene-coating does not affect the wettability of the underlying structure, an evaluation of the capillary pressure and permeability performance of the foams was performed.

The applicability of these types of foams to be implemented – from a capillary pressure perspective – into a vapor chamber testing set-up was analyzed by dipping the

wick structures in a 20 mL bath of OpticoolA. OpticoolA was chosen due to its higher wettability and lower viscosity making differences between foam types more distinguishable. The vertical distance that the working fluid traveled was measured under rough estimation using calipers. Because of the imprecise technique, the results were only used to evaluate the relative performance between wick types and cannot be directly compared against outside wick structures. Due to the high permeability of foams over other wick types, this test was primarily performed to gauge the capillary performance to understand which foam type would perform best in a vapor chamber system. Table 7 presents the results for both copper foams and graphene copper foams to understand if the graphene coating had a large effect on the capillary pressures.

Table 7 – Vertical travel distance of OpticoolA through Cu foams and Gr-coated Cu foams demonstrating the relative capillary performance of foam types.

Foam	ρ^*	Travel Distance	
		Cu Foam	Gr-Coated Cu Foam
40 PPI Uncomp	10%	4.0 mm	3.7 mm
20 PPI Uncomp	10%	2.8 mm	2.7 mm
20 PPI 2x Comp	19%	6.8 mm	6.6 mm
40 PPI 2x Comp	21%	10.1 mm	9.8 mm

The graphene coating had minimal effect on the capillary performance which was expected as capillary pressures are a factor of wettability of the working fluid which was also unaffected. Furthermore, the 40 PPI 2x Comp foam type produced the largest travel distance of the working fluid indicating that it highest capillary pressures relative to the other foam types.

Another set of testing was performed to evaluate both the capillary performance and permeability by measuring the travel speed of OpticoolA through the different foam types. A 50 mL bath of OpticoolA was used to ensure there would be a sufficient amount of fluid for each test. The foam was slowly lowered into the bath and observed using a Kron Chronos 1.4 – an optical high-speed camera – to accurately measure both time and distance at a rate of 240 frames per second. The foam is left in contact with the bath for 5 seconds to ensure enough time is given for fluid travel. Once again, these measurements were imprecise due to the difficulty in measuring speed due to the low light absorption of the high-speed camera. For that reason, these results were used to measure the relative performance between foam types. Because permeability is a function of pore size which is unaffected by the added graphene layer, these tests were performed on only the base copper foams. As expected, the 40 PPI 2x compressed (21.2% ρ^*) foam type performed the most promising for the application from a capillary performance and permeability perspective with fluid travel speeds. Both uncompressed foam types demonstrated insufficient capillary pressures to finish the tests making the foam type unfavorable for future vapor chamber implementation.

3.5 Physical Property Characterization Of Gr-Coated Foams

After verifying the presence and wetting properties of the monolayer Gr-coating on Cu samples, the electrical, thermal, and mechanical properties of the Cu foam with and without a graphene coating were obtained.

3.5.1 *Laser Flash Analysis Of Single-Layer Coating*

Thermal characterization of the Cu foam with and without a graphene coating was obtained using LFA, specifically, a Netzch LFA 467 HT HyperFlash. Samples were 10 mm x 10 mm in area and placed into the furnace chamber. The density of each foam sample was also measured before thermal analysis. Furthermore, because few-layer graphene is a highly transparent material, the copper foam-coated graphene may maintain copper's highly reflective properties. To ensure efficient amounts of infrared light were absorbed into the foam structure during testing, all samples were spray-coated with an opaque graphite coating. For the test, thermal diffusivity measurements were made from 25°C then 50°C to 350°C in increments of 50°C. Diffusivity measurements are taken three times for each sample at a given temperature. The same temperature range was used for STA runs as well. Thermal diffusivities were almost incomparable between foam tests due to the high dependency on density, so the foams can only be compared by calculated thermal conductivity. Both the thermal conductivity of the copper foams and graphene-coated copper foams and the increase in thermal conductivity is shown in Figure 24. The error between each temperature data set was measured to an average of 2.5%, while the error between foams was around 5%.

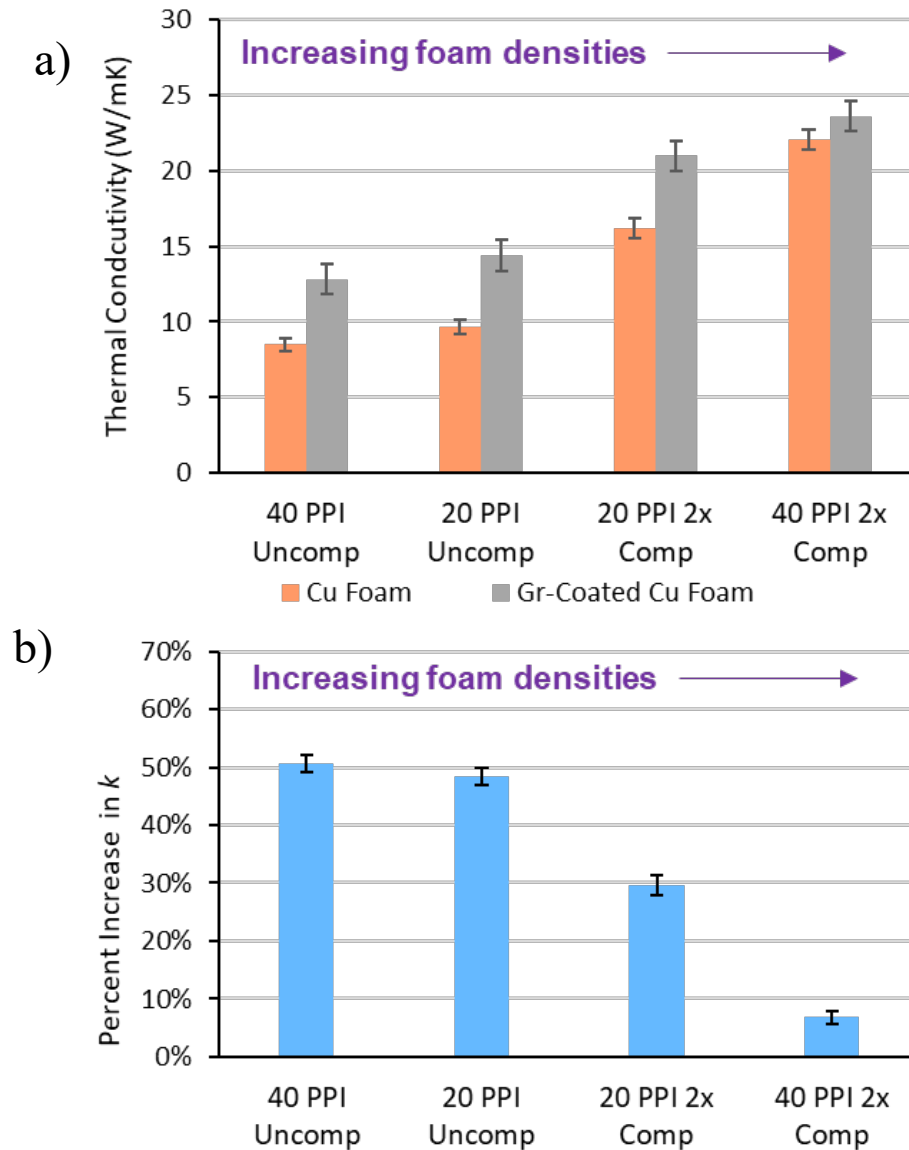
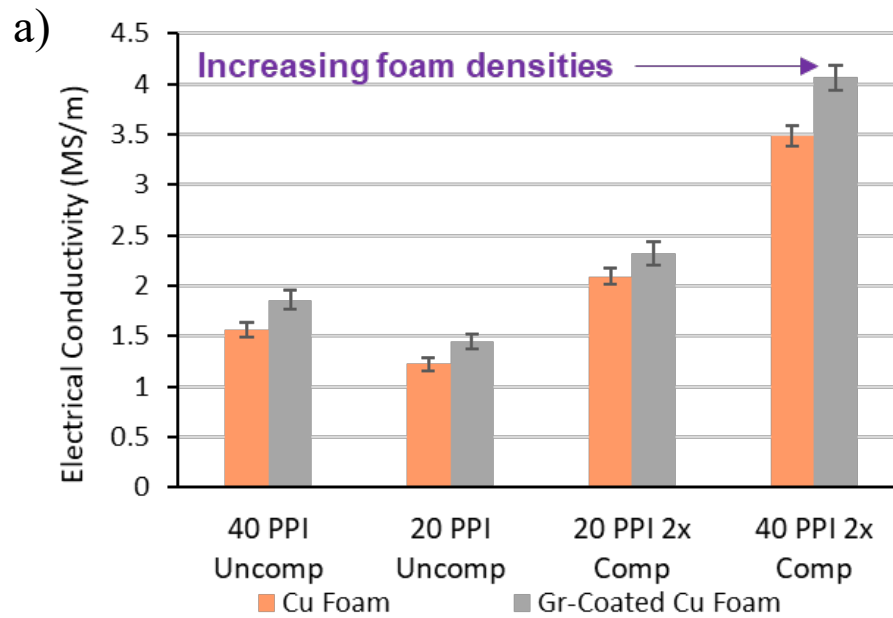


Figure 24 – a) The thermal conductivity of Cu foams and Gr-coated Cu foams and the b) thermal conductivity improvement for each foam type at 25°C.

For thermal testing, all foams saw an increase in thermal properties as well with the largest increase being for the 40 PPI uncompressed foam which saw a thermal conductivity increase from 8.5 W/mK to 12.8 W/mK (+51%). The full results from the thermal characterization at room temperature are displayed in Table 8.

3.5.2 Four-Point Probe Analysis Of Single-Layer Coating

The electrical conductivity of the Cu foams with and without a graphene coating was obtained using a Signatone four-point probe. The electrical resistivity of both the pure copper base foams and single-layer composites was measured to compare the improvements based on each structure. Due to the randomness of the foam structure, 5 electrical resistivity measurements were taken at 5 separate locations on both the front and back sides of the foam. The results for the electrical conductivity measurements of the copper foams and graphene-coated copper foams are displayed in Figure 25.



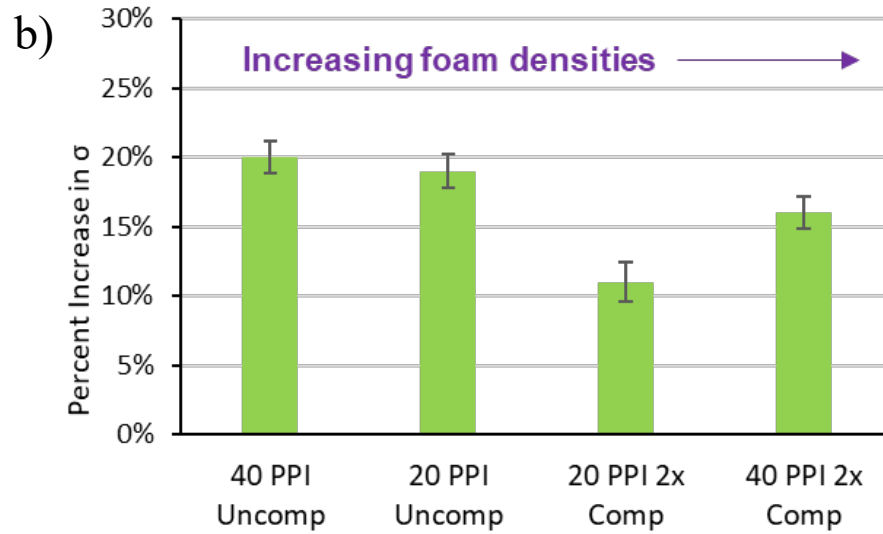


Figure 25 – a) The thermal conductivity of Cu foams and Gr-coated Cu foams and the b) thermal conductivity improvement for each foam type at 25°C.

Both uncompressed foams had a greater increasing electrical performance over their twice compressed counterparts indicating that the increased connectivity of the foams could be contributing to better property improvements. For the electrical testing, the pure copper uncompressed 40PPI foams had the largest average improvement in electrical conductivity from 1.57 MS/m to 1.86 MS/m (+20%), while the worst performance improvement was seen in the 20PPI foams with an electrical conductivity increase from 2.09 MS/m to 2.32 MS/m (+11%). The complete data from the four-point probe testing on the single-layer composite is shown in Table 8.

Based on both the thermal and electrical data, the low-porosity foams should have more improvements compared to their high-density counterparts. August et al. [92] demonstrated the surface-to-volume ratio – or exchange surface – based on ligament thickness and relative density. The foams were generated through the decomposition of

3D-Voronoi models to generate similar randomness of metal open-cell foams. As shown in Figure 26 from numerical simulations, higher relative density foams have a higher exchange surface than their lower density foams.

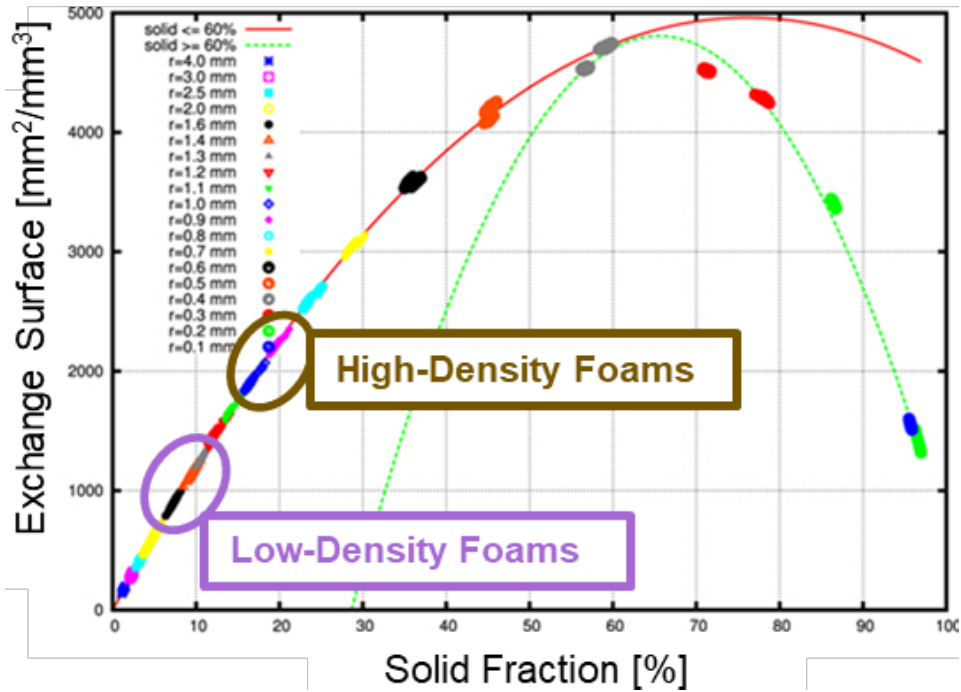


Figure 26 – Exchange surface based on the relative density of metal open-cell foams with an average ligament radius of 0.1 mm [92].

For all metal open-cell foams, increasing the relative density of the foam results in an increase in the surface-to-volume ratio. As graphene is a 2D structure, the vol% of graphene in the copper foam is directly proportional to the exchange surface as well. Based on the data from August et al. [92], the higher-density foams have an exchange surface twice that of the lower-density foams, $\sim 2000 \text{ m}^2/\text{m}^3$ vs. $\sim 1000 \text{ m}^2/\text{m}^3$. Because graphene is a 2-dimensional structure, the amount of graphene-coated is proportional to the exchange surface. Therefore, it can be reasonably inferred that the large increase in thermal

conductivity of the low-density foams vs. the high-density foams cannot solely be attributed to the vol% addition of graphene, so further literature was analyzed to understand the thermal and electrical mechanisms demonstrated by the coatings.

Though thermal and electrical conductivities are typically thought to improve relatively similarly to each other, the theory behind how graphene transports heat vs. electricity can give insight into the differing property improvement rates. As with all materials, graphene and copper's electrical conductivity is based on the transportation of electrons through the material. Since electrons are a major component in heat transfer as well, increasing electron conductivity can in turn increase thermal conductivity; however, phonons are another particle that can contribute heavily to a material's heat transfer capabilities. As monolayer graphene is a two-dimensional material, phonon dispersion and confinement are significantly different than for 3-dimensional counterparts. Although the fundamental reasoning behind the significant difference in phonon properties between the two-dimensional graphene and graphite/bulk crystals is continuously being studied, experimental data has proven a large part of thermal transport in graphene at room temperature is heavily dictated by phonons with negligible effect from electrons [93-95].

Table 8 – Electrical and thermal properties of Cu and Cu-Gr single-layer foams.

Foam [Description]	ρ^* [%]	Percentage of Node			Thermal Conductivity		Electrical Conductivity	
		4-N	3-N [%]	2-N	[W/mK] Cu	[W/mK] Cu + Gr	[MS/m] Cu	[MS/m] Cu + Gr
40 PPI Uncomp.	9.5	59	35	6	8.5	12.8 (+51%)	1.57	1.86 (+20%)
40 PPI 2× Comp.	21.0	27	35	38	22.1	23.6 (+8%)	3.48	4.06 (+17%)
20 PPI Uncomp.	10.2	70	24	6	9.7	14.4 (+48%)	1.22	1.45 (+19%)
20 PPI 2× Comp.	19.4	33	35	32	16.2	21.0 (+31%)	2.09	2.32 (+11%)

3.5.3 Uniaxial Tensile Testing Of Single-Layer Coating

Finally, uniaxial tension tests were performed on all copper foam with and without the graphene coating. Tensile testing was selected since foams perform worse under tensile stresses compared to shear and compressive stresses. As the foam wicks will be subject to multiaxial stresses during both fabrication and use of the vapor chamber, it is important to understand if the foams can withstand the tensile loads. A Kammrath & Weiss testing frame with a 5kN load head and a minimum gauge length of 8 mm was used to perform the uniaxial tension test. To limit compressive stresses and limit damage to the copper foam, an adhesive was used to secure the foam ends to the grips of the mechanical tester. 4 hours were given for the glue to set and ensure there would be no slipping of the foams. The tensile tests are performed until full failure of the foam wick which ranges between 20 - 140% elongation depending on both toughness and ligament orientation. Because of the

randomness of the foam's inner structure, the main properties analyzed for comparison are Young's modulus, yield strength, ultimate tensile strength (UTS), and energy absorption. The Young's modulus was calculated as the slope of the stress vs. strain curve from the start to 0.2% elongation. The yield strength was calculated by the intersection between the Young's modulus at a 0.2% strain offset with the stress vs. strain curve. Energy absorption was calculated as the area under the stress vs. strain curve up to the UTS point. The UTS was chosen as an appropriate point as it is where ligaments begin to individually fracture and fail. Since the uniaxial tensile tests were destructive and required large foam samples (25mm x 8 mm x 3mm), only around 2 tests could be performed for each foam type for each coating layer. Stress vs. strain graphs comparing 20 PPI uncompressed and 2x compressed for both the base Cu foams and Gr-coated Cu foams are shown in Figure 27. Furthermore, the yield strength, Young's modulus, and energy absorption of both the base Cu foams and Gr-coated Cu foam are displayed in Figure 28. The tensile mechanical properties of both the base Cu foam and Gr-coated Cu foams are shown in Table 9.

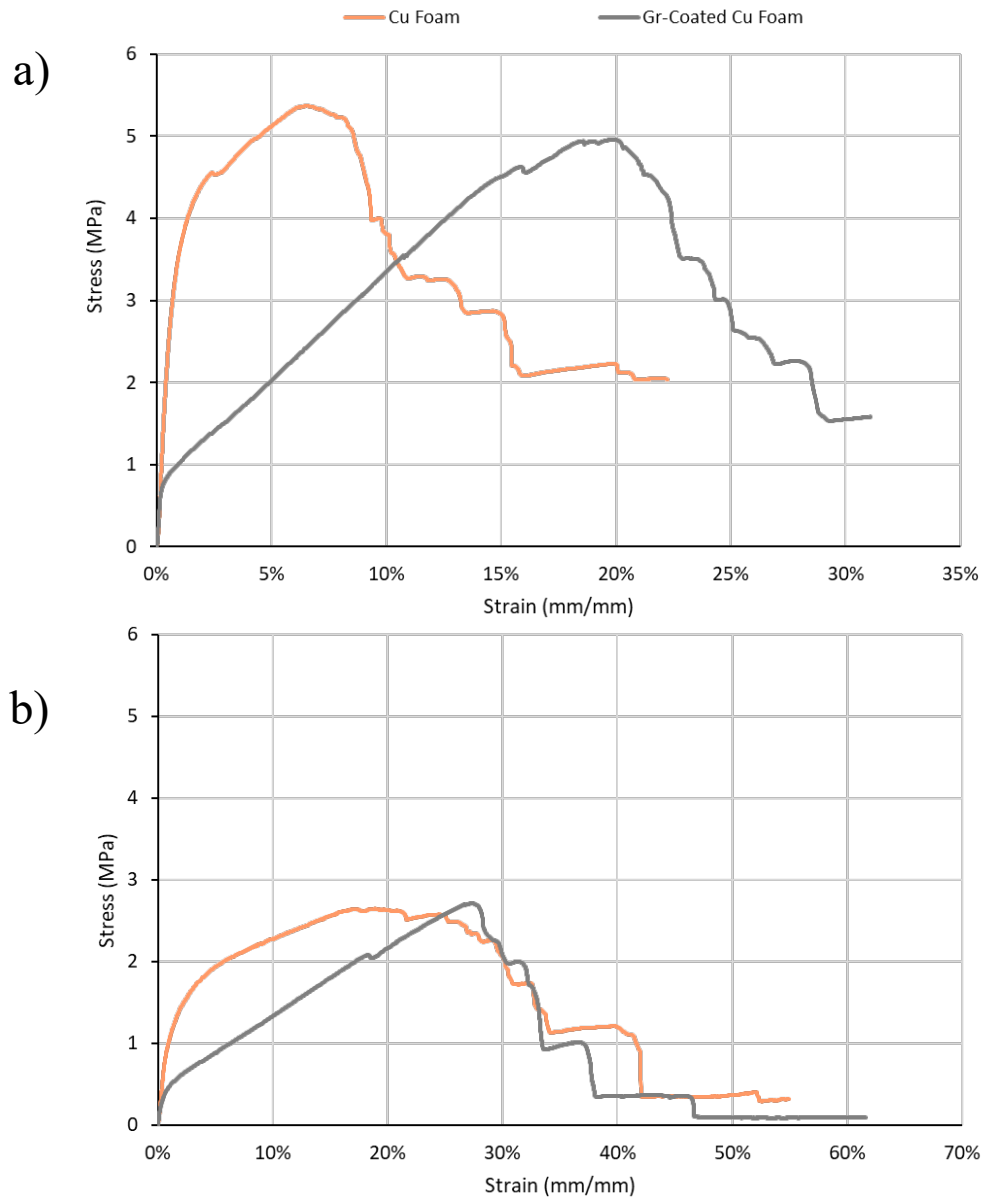
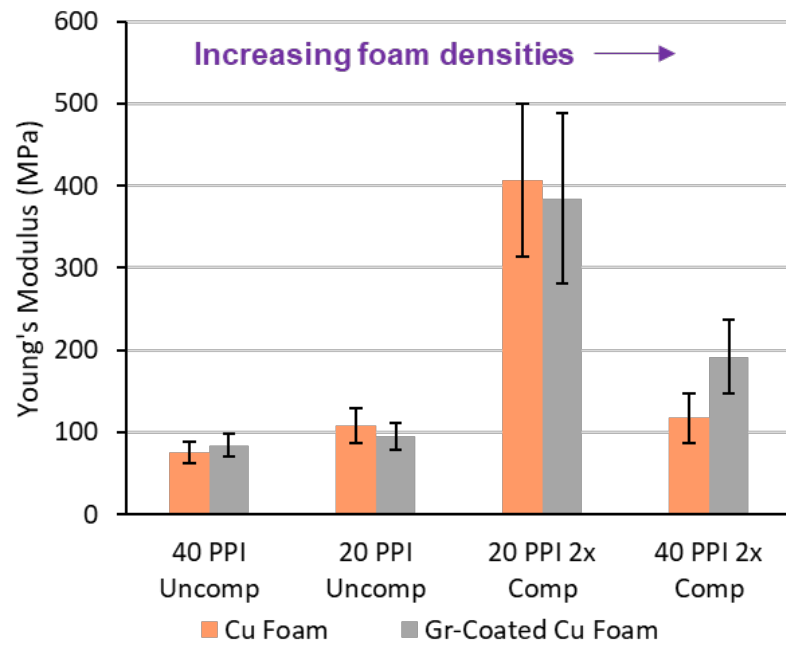
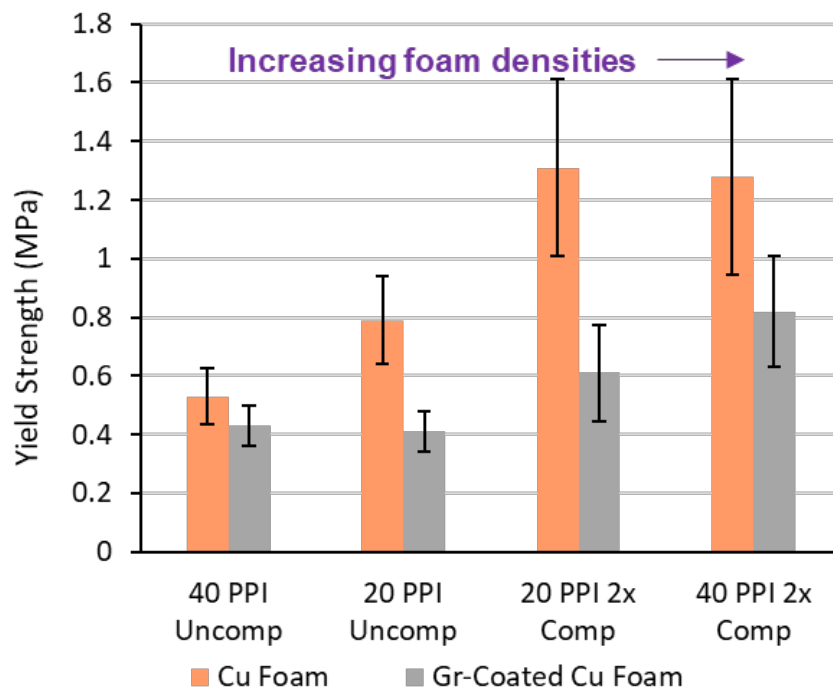


Figure 27 – Stress vs. strain curves of Cu and Gr-coated Cu foams for both a) 20 PPI uncompressed and b) 20 PPI 2x compressed.

a)



b)



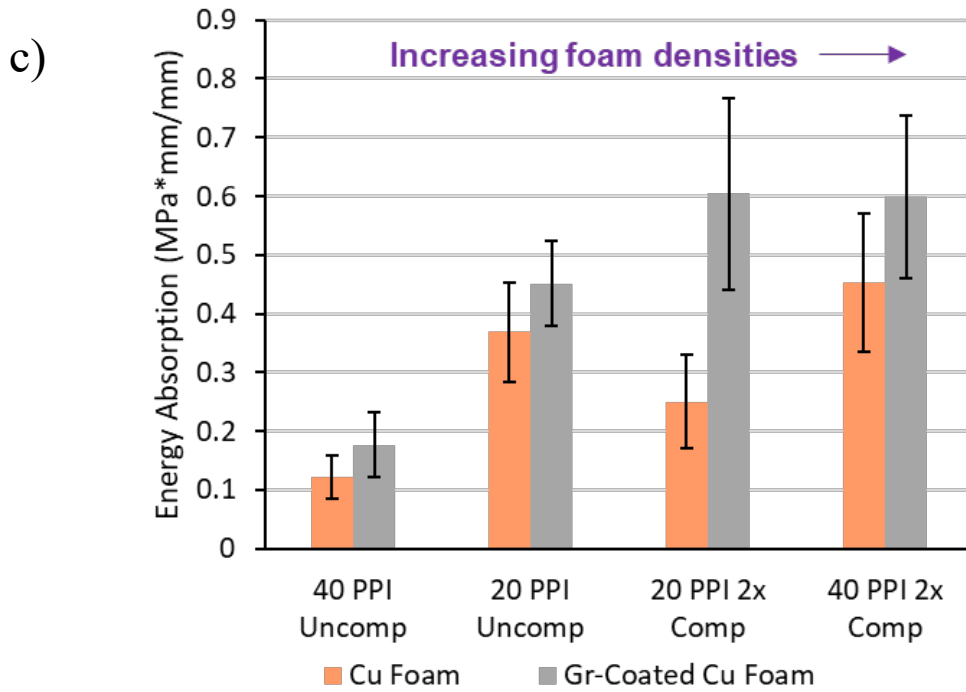


Figure 28 – The a) tensile Young’s modulus, b) tensile yield strength, and c) energy absorption of the base Cu foams vs. Gr-coated Cu foams.

Table 9 – Mechanical properties of Cu and Cu-Gr single-layer foams.

Foam [Description]	ρ^* [%]	Tensile Yield Strength		Elastic Modulus		Energy Absorption	
		[MPa] Cu	[MPa] Cu + Gr	[MPa] Cu	[MPa] Cu + Gr	[MPa*mm/mm] Cu	[MPa*mm/mm] Cu + Gr
40 PPI Uncomp.	9.5	0.55	0.43 (-19%)	75	84 (+11%)	0.12	0.18 (+44%)
40 PPI 2× Comp.	21.0	0.85	0.64 (-36%)	117	173 (+47%)	0.45	0.60 (+32%)
20 PPI Uncomp.	10.2	0.79	0.41 (-49%)	108	95 (-12%)	0.37	0.45 (+22.2)
20 PPI 2× Comp.	19.4	1.31	0.61 (-54%)	407	384 (-6%)	0.25	0.60 (+141%)

The elastic modulus of the foams remained relatively the same with some exceptions from local high- or low-density variations due to the randomness of the foam network; however, most foams saw a significant increase in energy absorption during tensile loading.

The measured values of the yield strength shown are general approximations based on the curving region between two linear regions of the copper foam uniaxial testing. This region is the last region of the stress vs. strain curve in which some regions of the foam are still elastically deformed. Using the dimensions of integrable vapor chambers (40 mm x 40 mm x 3 mm) and the mechanical objectives of withstanding pressures of 344 kPa, the vapor chamber wicks would see multiaxial stresses of 2.3 MPa assuming the vapor chamber acts as a pressure vessel. The yield strengths demonstrated during mechanical testing indicate that these foams would not be suitable to be the sole reinforcement within a vapor chamber system, further emphasizing the importance of support pillars in vapor chamber design. Though there is a significant decrease in the yield strength of the materials, the large increase in toughness is a favorable property improvement for thermal applications due to the increased resistance to failure during thermal cycling. However, graphene has previously been used as a reinforcement material for metal composites for improved yield strength and Young's modulus. To understand why the graphene deposition negatively affected the yield strength, the LPCVD process was investigated.

3.5.3.1 Annealing Study Of Copper Foam

Looking into the CVD process, graphene deposition and growth occur at 1000°C over 30 min. After a deeper analysis of important copper temperatures, this puts the foam well above the recrystallization temperature (324°C) and near the melting temperature (1085°C) of copper. These conditions indicate that there could be annealing of the precursor Cu foam during graphene deposition. For this reason, Cu foams were placed in the CVD furnace without depositing any graphene to examine possible copper softening and annealing effects. As the annealing of copper can have a significant effect on not only the mechanical properties but electrical and thermal as well, a study of the property improvements by annealing was performed. The annealing of the foams increases the grain size decreasing the dislocation densities which, in turn, reduces the mechanical strength of the copper foams. Furthermore, internal stresses in the high-density induced during the post-processing compression are relaxed at the elevated temperatures due to the increased mobility of the copper atoms. The 40PPI uncompressed foam type was placed in a similar thermal cycle as the CVD process in an argon atmosphere without exposure to graphene nucleating gases to simulate the possible annealing during graphene deposition. The stress vs. strain curve of the 3 foam states (as-received Cu foam, annealed Cu foam, and Gr-coated Cu foam) is depicted in Figure 29.

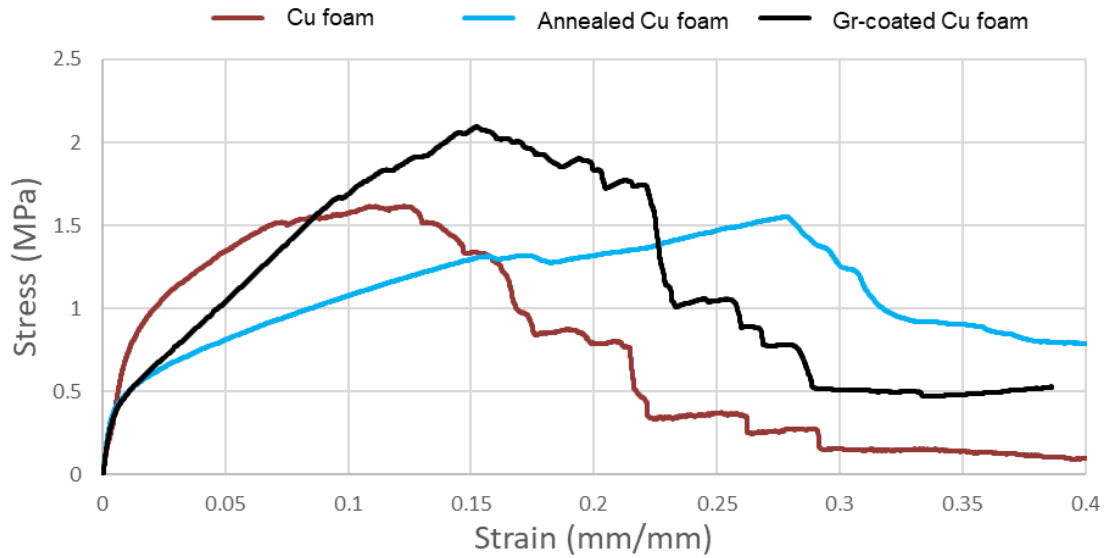


Figure 29 – Stress vs. strain of 40PPI uncompressed foam as received (red), annealed (blue), and Gr-coated (black).

From Figure 29, the large drop in yield strength seen in the Gr-coated copper foams is also seen in the annealed base copper foam. The yield stress of the annealed foam and graphene-coated foam dropped by 32% and 36% respectively though large improvements in the mechanical toughness were seen. Furthermore, the copper-graphene single-layer composite exhibited the highest elastic modulus and UTS compared to the base and annealed pure copper foams. These results demonstrate that the high-temperature CVD process plays a significant role in decreasing the mechanical properties of the base copper foam and is not a direct result of the graphene addition.

Following the mechanical analysis of the CVD annealing cycle, four-point probe analysis was performed and showed that the copper foam had an electrical conductivity improvement of ~8% from the annealing process. This indicates that the graphene addition still had a significant effect on the properties of the Gr-coated foam. As both heat and

electrical transport in copper are affected by free electron mobility, it can be safely assumed that some, but not all, of the thermal improvements seen during laser flash analysis can be attributed to the annealing of the base copper foam during the CVD process.

From the improvements seen in both thermal and electrical conductivity, the idea to add multiple layers of separate, parallel graphene networks was developed to test if the benefits of the graphene coating could be further improved. These graphene layers would need to be separated by a copper layer so a conformal deposition process needed to be developed for the multilayer coating could be deposited. For multilayer fabrication, the low-density 40 PPI uncompressed foam was selected because the foam type displayed the largest improvement in electrical and thermal properties. The 40 PPI 2x compressed was also selected for further development due to its higher capillary pressures for future vapor chamber implementation.

CHAPTER 4. MULTILAYER GRAPHENE COATING

4.1 Electroless Deposition Of Intermediate Cu Layer On Gr-Coated Cu Foam

Because of the promising results from the single-layer Gr-coating on the Cu foam wicks, further research into the fabrication of a coating comprised of multiple, parallel monolayer graphene networks separated by intermediate copper layers was researched. For the development of the multilayer system, a method of applying a uniform, conformal coating of copper onto an irregular structure would be necessary to separate the graphene layers. Though sputtering has been a common method to apply a thin, conformal coating in most electronic packaging applications, the directionality of the sputtering process with the irregular topology of a foam could lead to significantly non-uniform coating throughout the foam with the increased difficulty of deposition with higher density foams. Furthermore, sputtering processes have been shown to damage due to the high energy of the sputtered atoms onto the thin layer [96]. Electroless plating, on the other hand, is another copper deposition process that relies on the electrode potential of a given surface when fully submerged in an electroless bath. As the name implies, electroless plating does not require external energy and naturally deposits a coating through chemical reactions on a substrate over time. An electroless bath is an aqueous solution containing free metal ions that can be reduced onto a substrate surface. The two reactions that occur in the electroless process are the cathodic reduction reaction of the metal ions and the anodic oxidation of a reducing agent [97]. Formaldehyde is a common reducing agent for electroless copper plating. The probability of a spontaneous redox reaction can be predicted by the redox electrode potential which is related to the Gibbs free energy (ΔG) and rate constant of the

electrode reaction [97]. Negative redox potential is a good indicator of an effective electroless deposition process given certain parameters. When the reducing agent becomes oxidized, it provides electrons to the Cu^{2+} ions in the solution to reduce to Cu^0 on the substrate; however, in some systems, if the activation energy is much higher than the activation energy required for room temperature deposition, the spontaneous solution decomposition has a low probability of occurring [98]. Also, since the deposition process is purely based on chemical reactions and not electrical fields (electrolytic deposition), a uniform deposition can be achieved for complex shapes. As all surfaces of the open-cell foam would be exposed to the bath, a conformal coating could be achieved with an optimized process; however, because chemical nature of the process, deposition rates are lower than that of other copper deposition methods. Due to the effectiveness of the electroless deposition process, electroless copper plating was viewed as a potential option to create intermediate layers between graphene networks. Though graphene is a recently introduced material for electronic applications, there have already been attempts to electrolessly deposit metal layers onto a graphene surface by using graphene as the reducing agent. Narula et al. [99] have demonstrated a method of electrolessly plating copper by using graphene as the reducing agent in a 0.2 M copper sulfate bath at room temperature. Typically, in the case of copper and graphene, copper has a higher work function than graphene indicating the electrochemical potential of reduction would be positive; however, a study of charge transfer by Khomyakov et al. [100] showed that when the equilibrium separation is under a specific value, the electrochemical potential can be negative resulting in a negative charge on the graphene surface and positive charge on the copper allowing for the reduction of the free Cu^{+2} onto the graphene surface. Furthermore,

experimental proofs have indicated that graphene in contact with copper can behave n-doped possibly providing electrons for Cu^{2+} reduction for electroless deposition [101]. Cole et al. [102] further analyzed how the electrochemical potential at the graphene surface can cause an excess build-up of hydronium ions that can accumulate electrons at the graphene surface in low pH solutions. Reduction of Cu^{2+} thus takes place through the accumulated hydronium ions by band alignment of n-doped graphene and reduction potential. Thus, this phenomenon at the graphene interface makes the electroless deposition of copper onto graphene an effective method of depositing the intermediate copper layer. The successful setups used in the literature were applied to replicate the deposition process for multilayer coating development.

4.1.1 Original Electroless Cu Deposition Setup

For beginning trials of electroless copper deposition, a similar setup was used as seen in the literature [103]. A 25 ml of Atotech 0.4 M copper sulfate solution was diluted to a 0.2 M copper sulfate solution using DI water to create a 50 ml electroless solution. The deposition process took place at room temperature with no form of circulation in the bath. For verification of the process, a monolayer graphene-coated copper sheet was placed in the bath for 12 hours.

4.1.1.1 Challenges With Characterizing The Deposited Cu Layer

Though SEM and Raman spectroscopy can be used to show the presence of copper on the surface of the graphene, measuring the growth rate of the copper layer can be challenging. SEM imaging of the copper layer on the sheet composite showed impartial coverage of the graphene layer. From simple optical cross-sectioning of the top surface,

the original copper and deposited copper were indistinguishable with no evidence of the location of the graphene layer. An SEM-based method was developed as described below.

4.1.2 Plating Rate Characterization On Cu Foil Geometries

To analyze the deposition, the protective polymer coating (nitrocellulose in ethyl acetate) was placed on a part of the surface to be coated and acted as a copper growth prohibitor. SEM imaging at the interface of the polymer coating and deposited copper could be used to identify the thickness of the deposited copper (see Figure 30). By using a micro-cross-sectioning technique, the difference in copper height can be analyzed to measure the deposition rate of the copper layer. The first samples used for the characterization of the deposited layer were pure copper sheets and the deposition process is shown in Figure 30.

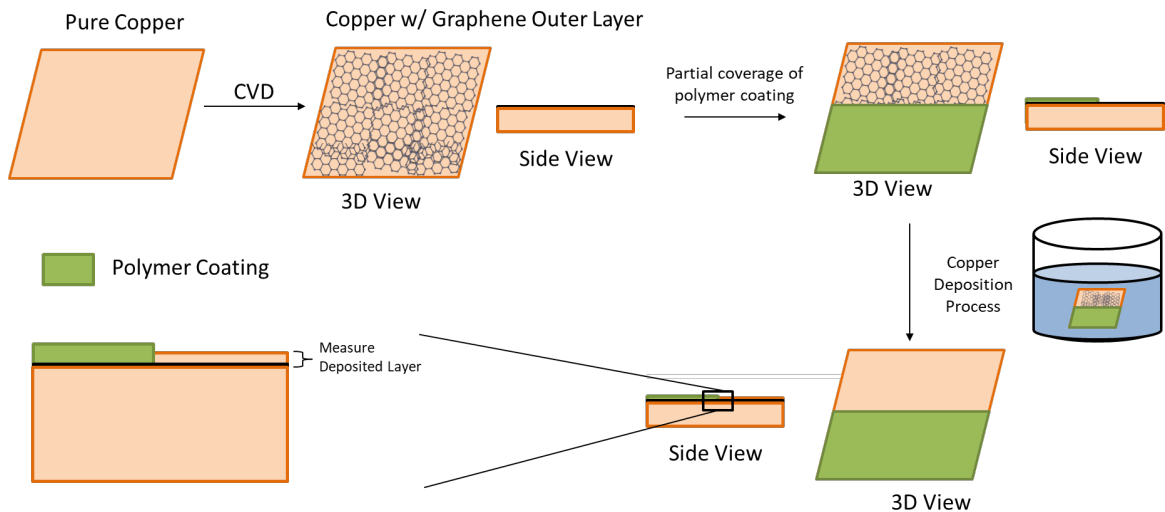


Figure 30 – Deposition process using a polymer coating as a Cu growth inhibitor to analyze growth rates.

For a clearer deposition layer during analysis, the deposition time for the copper intermediate layer was increased to 24 hours still at room temperature. The cross-sectioning

technique used in the process utilizes a Thermo-Fisher Helios 5CX FIB-SEM (Focused Ion Beam – Scanning Electron Microscopy) to mill away material to analyze the polymer/Cu interface. A FIB-SEM is a tool that combines visual analysis with the milling capabilities of the condensed ion beam. To use the FIB capabilities of the tool, the sample must be placed at a working distance of 4mm and an angle of 52° (perpendicular to the ion beam). As the polymer coating is prone to charging under both the SEM and FIB portions of the tool, a thin carbon strip is deposited over the interface region. The carbon strip also helps to protect the cross-section interface from degradation by high-energy ions. After the carbon strip is deposited, a rectangular cut is made using the ion beam at $\sim 0.43\text{nA}$. A cleaning cut was then made using a lower current of $\sim 0.23\text{A}$. The cross-section is then viewed with the SEM at the 38° angle. The polymer coating and electroless copper interface, analyzed under a FIB-SEM, is shown in Figure 31.

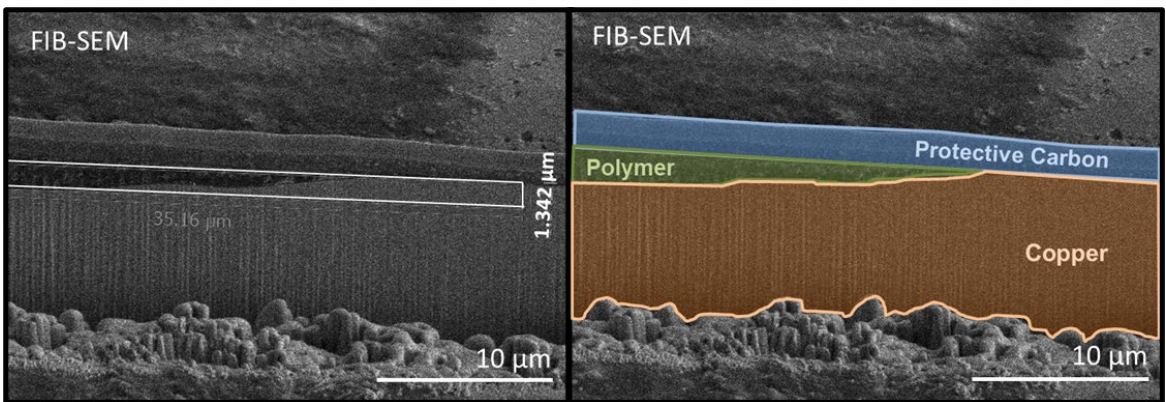


Figure 31 – FIB-SEM cross-section of polymer coating and electroless copper interface for deposition rate characterization.

From the FIB-SEM analysis, the difference in the two layers is found to be $\sim 1.7\mu\text{m}$ after correcting for the viewing angle tilt, equating to an average deposition rate of $0.07\mu\text{m/hr}$ on the copper sheet. However, due to the higher surface-to-volume ratio and

confined spaces of the copper foams, the electroless copper deposition rate on the sheet geometry cannot be assumed for the foam geometry as well. Therefore, the deposition rate characterization process was solely for proof-of-concept for depositing copper on the graphene layer and for a method of electroless copper deposition rates in a time-efficient manner.

4.1.2.1 Optimization Of Electroless Cu Deposition Process

After confirming the existence of the Cu layer and deposition rate characterization technique on the copper sheet, the electroless process was performed on the Gr-coated Cu foams. Because the foam structure has a significantly higher surface-to-volume ratio and the pores restrict solution flow, it cannot be assumed the foam will have a similar deposition rate as the Cu sheet. Furthermore, due to the incomplete coverage seen on the Cu sheet circulation was added to improve the deposition coverage, and the electroless Cu deposition process was optimized by increasing the concentration of copper sulfate in the electroless solution. SEM imaging was used to characterize the increasing coverage of electroless copper on the Gr-coated foam wick which is shown in Figure 32.

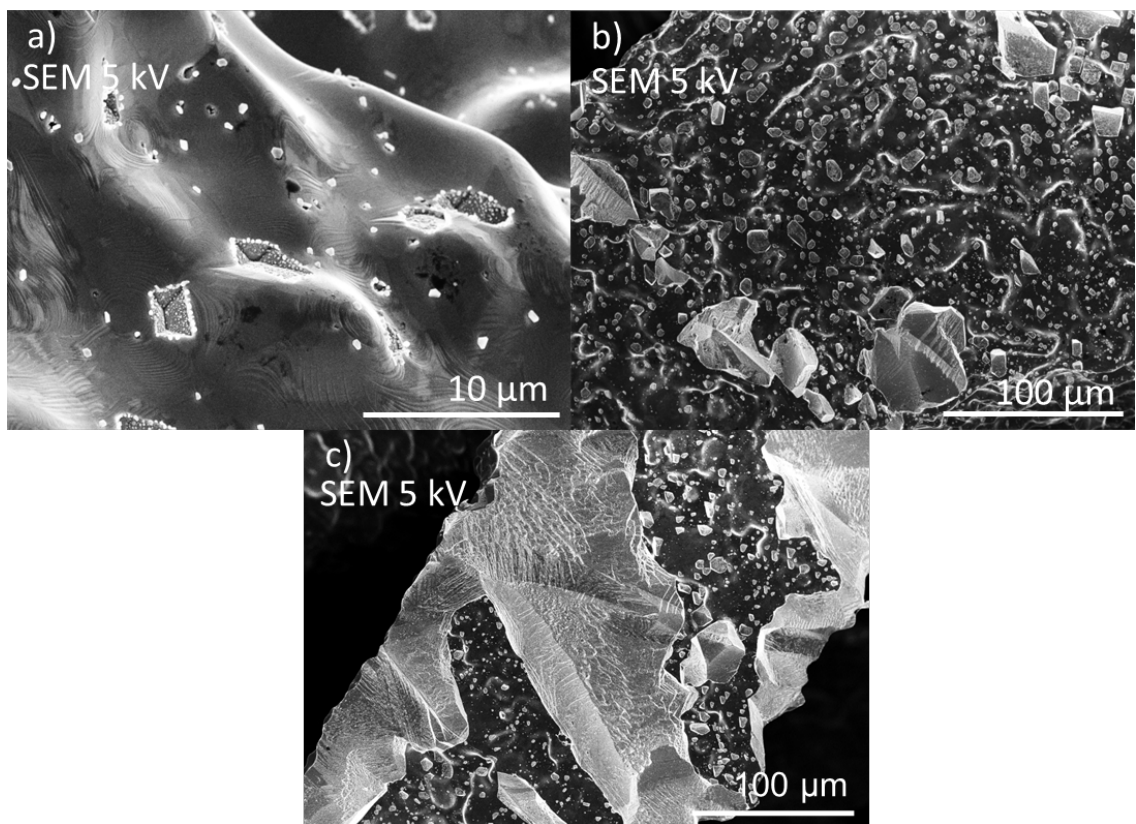


Figure 32 – SEM imaging of Cu deposition on Gr-coated Cu foams after original electroless deposition at a) 0.2 M CuSO₄ (low coverage), b) 0.3 M CuSO₄ (medium coverage), and c) 0.4 M CuSO₄ (high, but incomplete coverage).

Electroless deposition in a 0.2 M CuSO₄ electroless bath, shown in Figure 32a, resulted in a low amount of coverage of copper on the graphene surface. From SEM analysis, the graphene “wrinkles” are exposed with copper grain nucleation sites around 5 microns in diameter. With increased concentration to 0.3 M CuSO₄, the nucleation of copper grains remains relatively low and does not cover the dark graphene surface; however, the increase in concentration did result in increased growth in copper grains (indicated by the large lighter structures in Figure 32b). Increasing the concentration of the bath to the maximum concentration of the commercially available Atotech solution, 0.4 M CuSO₄, resulted in higher coverage of copper as shown in Figure 32c; however, there is

still a significant presence of uncovered graphene indicated by the continuous dark regions. These results make the current setup for depositing a conformal, fully covering copper intermediate layer unsuccessful. With the restrictions in bath concentration, the next step in improving the copper coverage is adding energy to promote nucleation and growth of the copper grains through the form of heat. Increasing the temperature of the electroless process may aid the deposition of copper since this is a common method in electrolytic processes to increase growth rates due to increasing the thermodynamic probability of the redox and oxidation reactions [98]. The electroless bath stayed at 0.4 M copper sulfate with light stirring (~100 rpm in 1L beaker) for 24hr, but the temperature was increased to 50°C. SEM analysis of the heated electroless copper deposition process is shown in Figure 33.

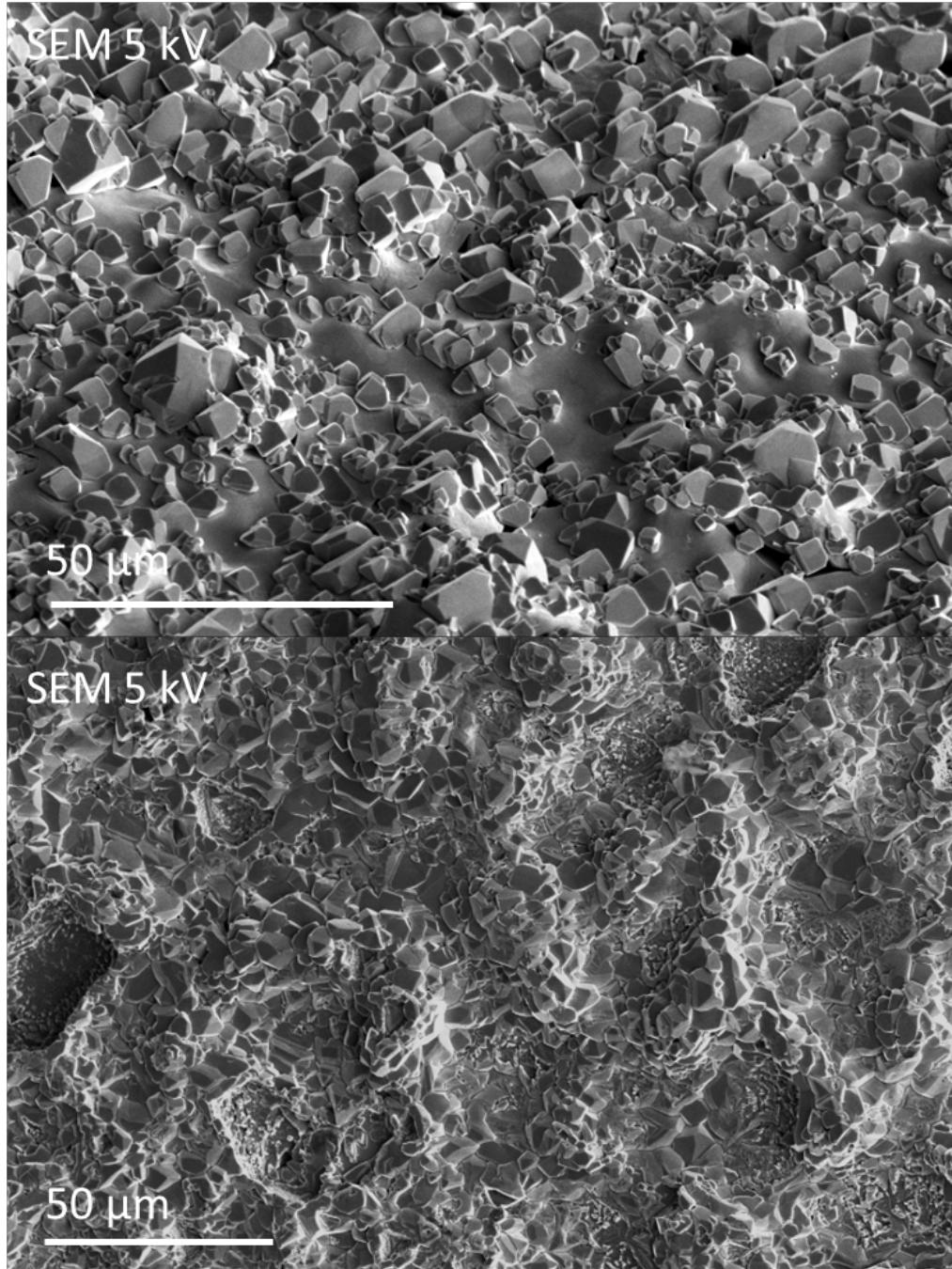


Figure 33 – SEM analysis of electrolessly deposited Cu on a Gr-coated Cu foam at 50°C.

SEM imaging of the foam surface shows high/full coverage in all regions of the foam creating an effective intermediate copper layer. The increased temperature resulted

in a significant increase in the nucleation and growth of electroless copper grains. The copper grains on the surface of the foam have variable diameters averaging between 5 – 10 μm .

4.1.2.2 Plating Rate Characterization On Foam Geometry

After an effective copper deposition process was created, the deposition rate of the copper layer was analyzed using a similar process to the copper foil geometry. The imaging of the interface is shown in Figure 34.

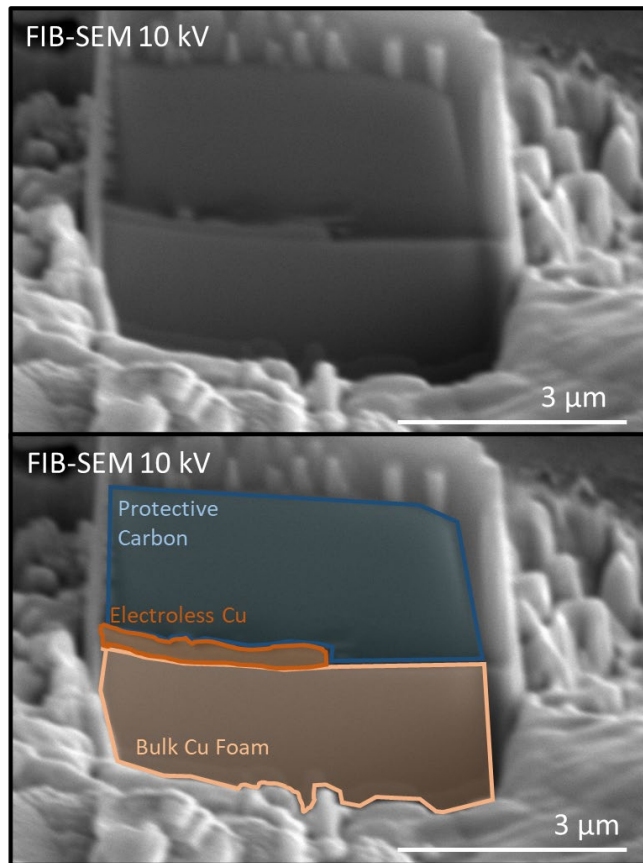


Figure 34 – FIB-SEM cross-section of newly deposition Cu layer on the Gr-coated Cu foam surface.

Due to the topology of the foam, a thick polymer coating is difficult to apply. Furthermore, under the ion beam, the protective polymer coating degrades from the surface before the carbon strip can be applied. For that reason, the polymer coating is not shown in the FIB-SEM cross-section; however, as shown in Figure 34, a distinct new copper layer can be seen under the protective carbon strip. The newly deposited copper region measures at roughly 650 ± 25 nm with an average deposition rate of 27 nm/hr; however, Figure 33 shows copper grains well over 20 microns in diameter which could indicate that in some regions of the foam, the electroless copper layer is thicker than the measured thickness at the protective polymer/Cu interface. Due to the precise nature of FIB-SEM analysis and geometry of the foams, only 3-5 measurements of polymer/Cu interfaces could be analyzed per sample.

4.1.2.3 Surface Analysis Of Electroless Cu Layer

After the verification of full coverage of the electroless copper layer, Raman analysis was performed to ensure there are no foreign structures that deposit from the copper sulfate bath. Specific foreign structures under investigation were high-intensity copper oxides, copper sulfate crystals, other sulfides, or other oxides. Figure 35 shows the results of the Raman spectroscopy using the same 488nm laser as previously used on the single-layer Gr-coated Cu foam samples.

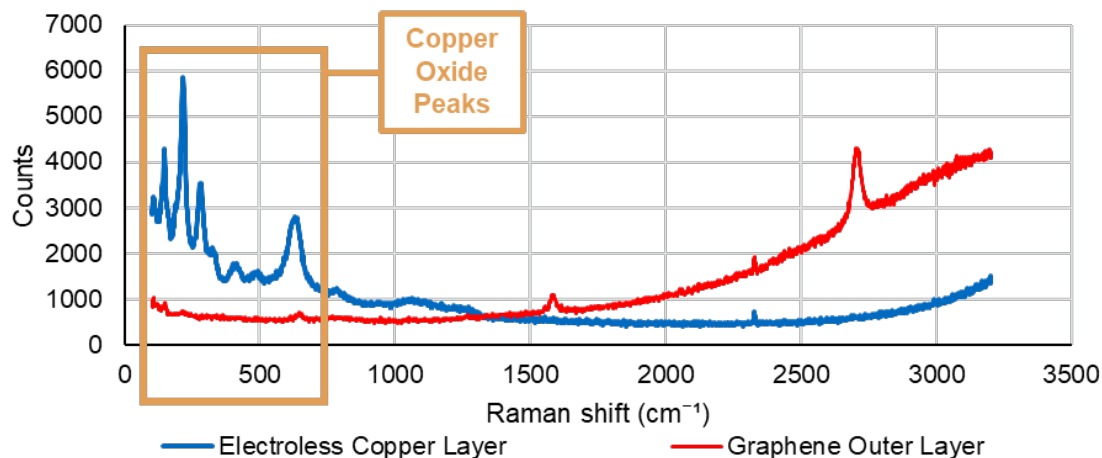


Figure 35 – Raman spectroscopy of Gr-coated Cu foam and electroless Cu layer.

Raman analysis of the copper layer shows no graphene peak intensities at either of the G or 2D peak locations compared to the Raman spectrum taken before deposition. As Raman is a surface characterization technique, this indicates there are no exposed areas of graphene on the foam surface; however, the large intensity peaks of the electroless copper layer’s Raman spectrum indicate the presence of cuprite (copper oxide). The formation of copper oxides on the surface could be a result of copper oxide formation during the electroless process or naturally forming surface oxides that form at room temperature. Because copper reduces from Cu^{2+} during the redox reaction, some copper ions may deposit as Cu^{+1} which oxygen may attach to nucleate copper oxide growth [99].

4.1.2.4 Surface Oxide Removal Of Electroless Cu Layer

To accurately assess the properties of the electroless Cu on the Gr-coated Cu foams, reduction of the surface oxides is needed as CuO can have a significant effect on thermal, mechanical, and electrical properties. Two different processes were analyzed for the removal of the surface oxides: sulfuric acid and forming gas. Sulfuric acid is a common acid that removes copper oxides through chemical reactions. The H_2SO_4 reacts with the

CuO to form CuSO₄ and H₂O as by-products; however, sulfuric acid can etch further than the oxide layer and possibly affect the underlying copper and graphene layers. To verify the process was appropriate for the composite foam, a copper-graphene single-layer sample was placed into a 5% H₂SO₄ acidic bath for 15 minutes. From Raman analysis, the H₂SO₄ had reduced the graphene intensity indicating possible removal of the graphene layer. Though the method could work with a reduced concentration of sulfuric acid, other methods of oxide removal were evaluated due to how thin each coating layer is.

Forming gas reduction of the copper oxide was a second promising option as it solely reduces the oxides rather than etching the copper entirely. Forming gas is a gaseous mixture of 5% H₂ in an N₂ atmosphere and is similar to the reduction process used during the CVD process of the graphene layers. The oxide reduction process using forming gas requires temperatures above 250°C to effectively reduce the oxide. The reduction process for the copper layer analysis ramps the furnace to 300°C in 9 sec. and is held at 300°C for 10 min. The forming gas is constantly circulated to ensure the water vapor by-products are properly removed during reduction. The temperature profile is shown in Figure 36.

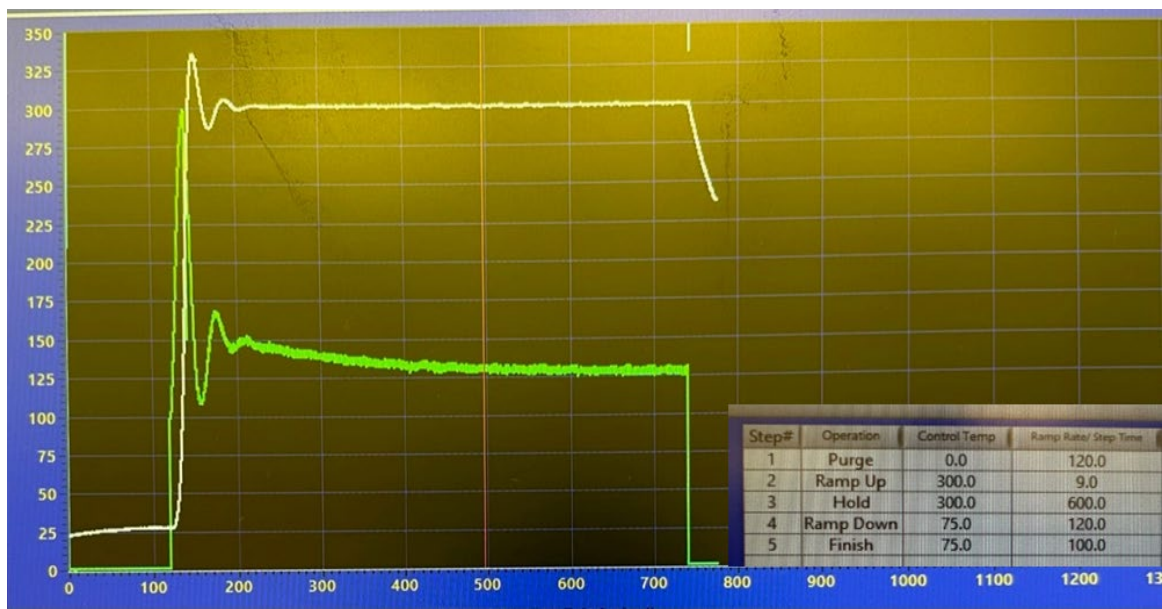


Figure 36 – Thermal profile of forming gas reduction process.

The white line in the thermal profile in Figure 36 denotes the temperature of the furnace, and due to the rapid increase in temperature, there is a slight overshoot to $\sim 330^{\circ}\text{C}$ which then levels out to 300°C after around a minute. The green line denotes the power usage to heat the furnace. As the furnace is cooling down, forming gas is still flowed through the chamber to prevent any oxidation of the sample. After the forming gas reduction, SEM analysis show slight deterioration of the copper/copper oxide grains while Raman analysis showed low-intensity peaks for copper oxide compared to the pre-forming gas samples. Because the reduction process occurs near the recrystallization temperature, it may also have a small effect on the underlying copper foam, so the reduction process was only performed when measuring the properties of the electroless Cu-coated foam and not for further development of the multilayer Gr-coating. Once the conformal electroless copper layer was analyzed through these surface characterization techniques, the foam samples were ready for the deposition of a secondary graphene layer.

4.2 Secondary Graphene Layer

Though there was an indication of copper oxide present in the electroless copper layer which could result in poor-quality graphene formation, the CVD process used is designed for oxide removal and grain growth. Along with hydrogen gas that can reduce the surface oxides of the copper foam, the high temperature of the process is also above the decomposition temperature of copper oxide (between 850 and 1000°C). Furthermore, the high-temperature annealing process will smoothen the electroless layer and increase grain size for high-quality graphene deposition. The same CVD processing parameters that were used to deposit the first graphene network were used to deposit the second.

4.2.1 *Surface Characterization*

As the CVD process is designed and optimized for graphene deposition and growth on pure copper surfaces and not oxides, a major concern for the deposited layer was going to be insufficient or no coverage of a secondary graphene layer; however, displayed in Figure 37, an interesting phenomenon is shown by SEM evaluation of the secondary graphene layer.

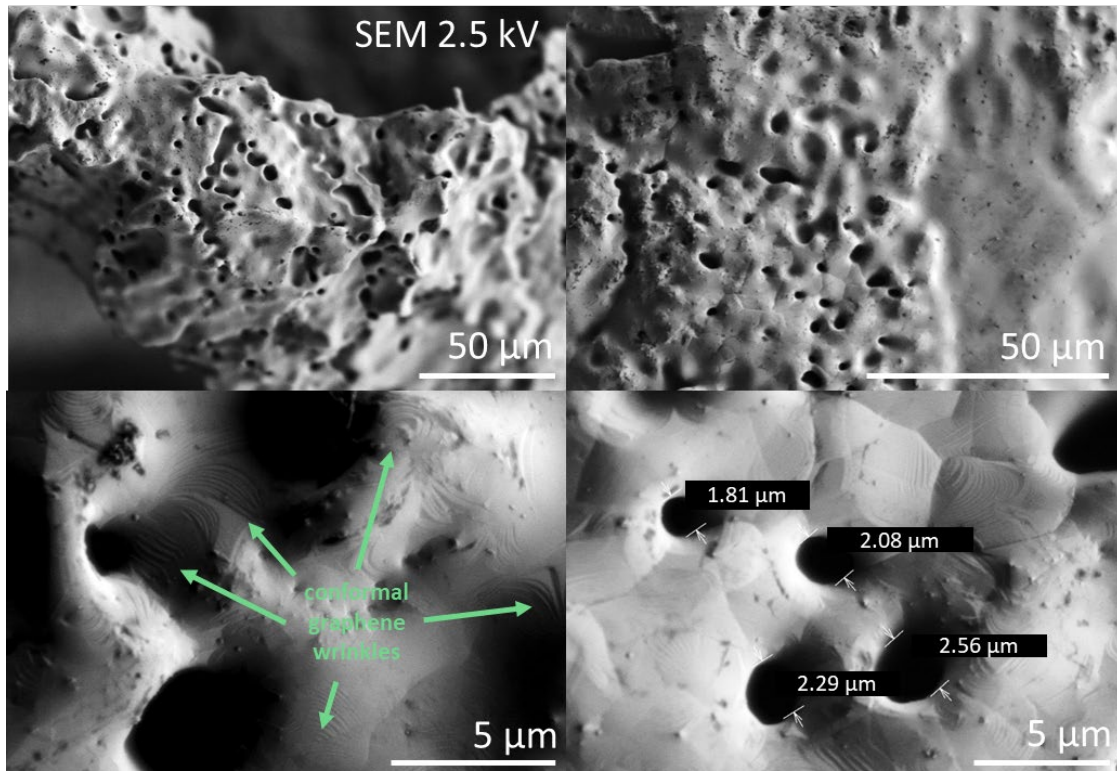


Figure 37 – SEM analysis of the secondary graphene layer of the multilayer Gr-coating.

The SEM analysis of the secondary graphene layer showed a high amount of surface micropores on the foam that had not previously existed caused by the high amount of volume lost during decomposition and reduction of the copper oxides. The micropores have diameters ranging between 1 – 10 μm , significantly smaller than the pore sizes of the base foam. Though these structures may look like a defect on the surface of the foam ligaments, the small micropores formed a biporous structure throughout the original foam. Biporous foams have demonstrated significant improvements in high heat flux applications due to their increased number of boiling sights as well as increased capillary pressures due to the addition of pores of smaller magnitudes [15]. Furthermore, SEM analysis confirmed that the graphene coating is conformal in and around the microporous (shown by the

graphene wrinkles in Figure 37). Raman spectroscopy was performed as well to verify that the copper oxide did not affect the thickness of the graphene layer as well. The results showed near identical spectra to the single-layer graphene coating with prominent peaks only at the G and 2D graphene peak locations as shown in Figure 38.

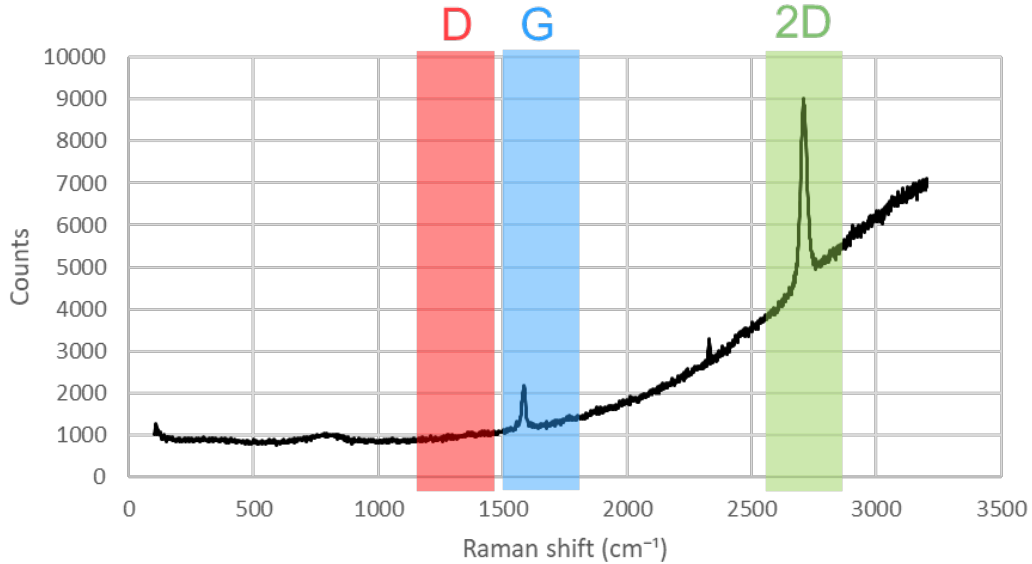


Figure 38 – Raman spectrum of secondary graphene layer deposited on the intermediate electroless Cu layer.

The high intensity of the 2D (2700 cm⁻¹) peak compared to the G peak (1560 cm⁻¹) indicates that the deposited graphene layer is monolayer/bilayer, the preferred graphene structure. Furthermore, despite the highly granular electroless layer, a conformal, continuous graphene layer was deposited as indicated by the absence of the D peak.

4.2.2 Thermal Characterization

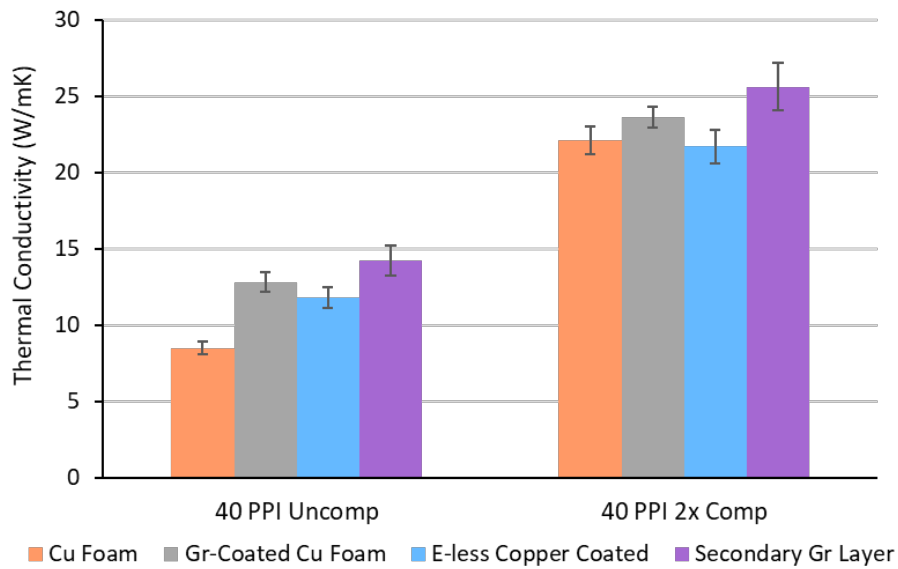
Based on the increased properties from the electrical characterization, further laser flash analysis was performed to understand if the thermal conductivity was similarly affected by the secondary graphene layer. Both the thermal diffusivity measured and

thermal conductivities calculated are shown in Table 10. Furthermore, a graph demonstrating the thermal conductivity of each coating layer along with the percent increase in thermal conductivity is displayed in Figure 39.

Table 10 – Thermal diffusivity and conductivity of 40 PPI uncompressed copper foam after multilayer graphene deposition process.

Foam	Relative Density [%]	Thermal Conductivity [W/mK]	Thermal Diffusivity [mm ² /s]	Density [% density]
40 PPI Uncomp				
Pure Cu	9.5	8.5	27.4	9.0
Cu-Gr		12.8 (+51%)	39.3	9.4
Cu-Gr-Cu		11.8 (+38%)	40.6	8.4
Cu-Gr-Cu-Gr		14.2 (+67%)	33.9	12.2

a)



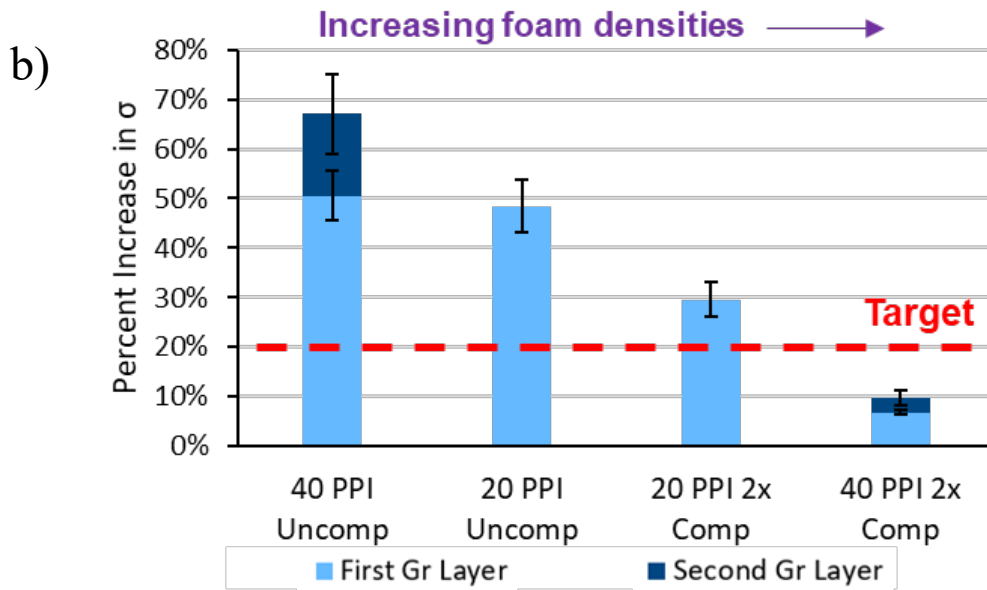


Figure 39 – a) Thermal conductivity of the 40 PPI foam types and b) the percent improvement in thermal conductivity with each additional Gr layer compared to the research objective.

After the deposition of two layers of separated graphene networks, the net percentage increase in thermal conductivity was +67% for the 40 PPI uncompressed foam type. As previously mentioned, the increases in thermal conductivity seen in the low-density copper foam can be contributed to both graphene’s unique high phonon mobility along with a higher total material percentage of graphene in the composite; however, the increase in thermal conductivity from the secondary graphene layer is lesser than the increase from the first. This could be a result of the increased interaction between the original graphene layer and the copper layers which has been shown to decrease graphene’s thermal properties along with the high oxide content in the electroless layer [104]. Though the low-density 40 PPI foam type well-exceeded the target thermal conductivity increase, the high-density counterpart fell short with both graphene layers indicating the importance

of a well-connected and organized foam structure. The thermal conductivity measurements of both the high-density and low-density foams are further presented in Table 12.

4.2.3 Electrical Characterization

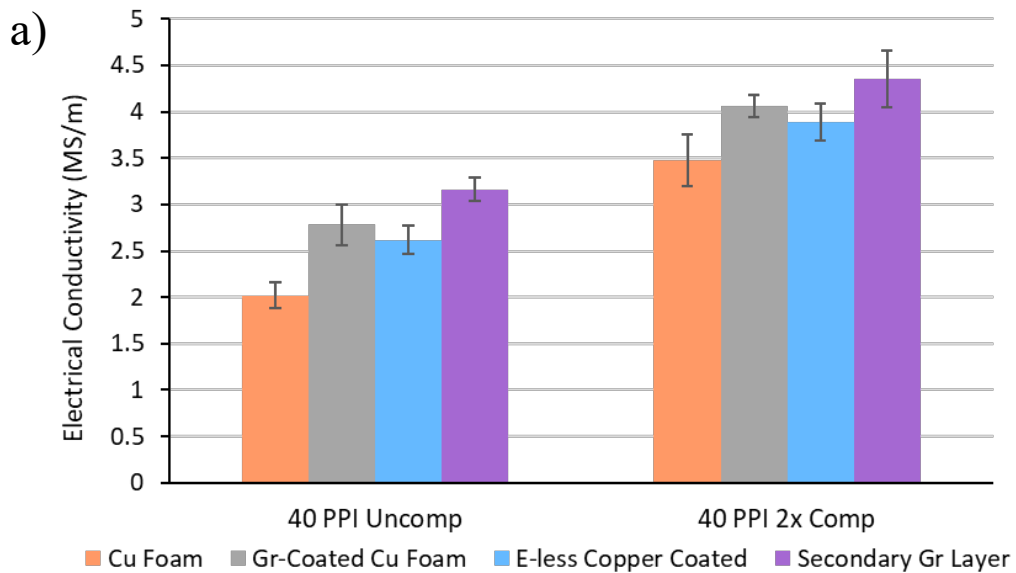
As electrical characterization of the foam composites is the only non-destructive testing method, a singular foam structure’s electrical resistivity and conductivity were measured through each step of the process to confirm the demonstrated trends and reduce the amount of uncertainty and error in the development of the multilayer coating. Four-point probe analysis was still used and the selected wick was the low porosity 40 PPI uncompressed foam since it was previously shown to have the largest benefit from the graphene additions. The measured ρ^* of the chosen 40 PPI uncompressed foam was 11.0%.

Table 11 – Electrical conductivity and resistivity of 40 PPI uncompressed copper foam after multilayer graphene deposition process.

Foam	Relative Density	Avg. Electrical Conductivity	Avg. Sheet Resistivity
40 PPI Uncomp	[%]	[MS/m]	[Ω/\square]
Pure Cu	11.0	2.02	1.60E-04
Cu-Gr		2.78 (+38%)	1.15E-04 (-28%)
Cu-Gr-Cu		2.63 (+30%)	1.23E-04 (-23%)
Cu-Gr-Cu-Gr		3.16 (+56%)	1.03E-04 (-36%)

As shown in Table 11, each layer demonstrated an increase in electrical properties over the original pure copper foam. The graphene layers demonstrated a 37.9% increase for the first graphene layer and a 20.1% increase for the second. Since the annealing process

had a lower impact than both of the property increases seen with graphene deposition, it can be inferred that both property improvements were heavily affected by the sequential graphene addition. The 40 PPI 2x compressed saw a similar trend increasing electrical conductivity from 4.06 MS/m with the single-layer graphene coating to 4.35 MS/m with the secondary graphene layer (an +7.1% increase with the second layer of graphene). Both foam types had a reduction in electrical conductivity due to the addition of the electroless layer as a result added oxide content similar to the thermal conductivity results. Figure 40 displays both the electrical conductivity of the 40 PPI foam types with each layer and the percent increase in electrical conductivity with each graphene layer.



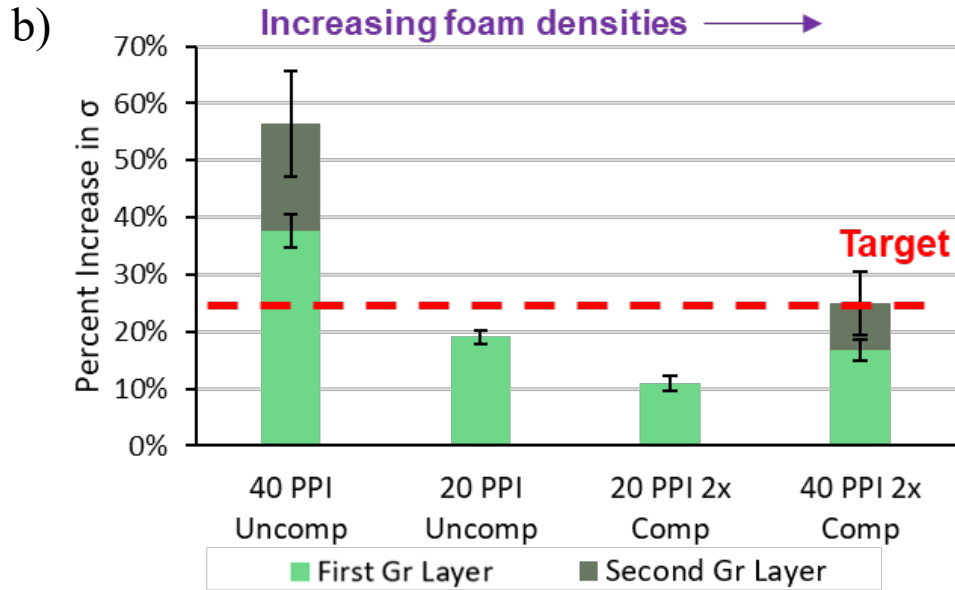
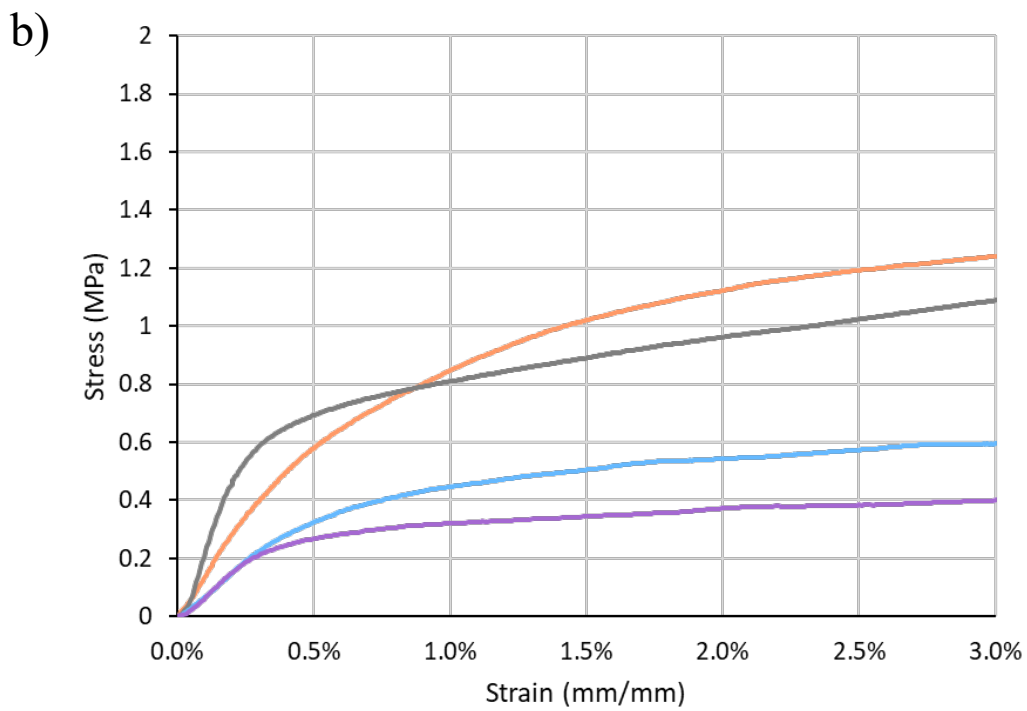
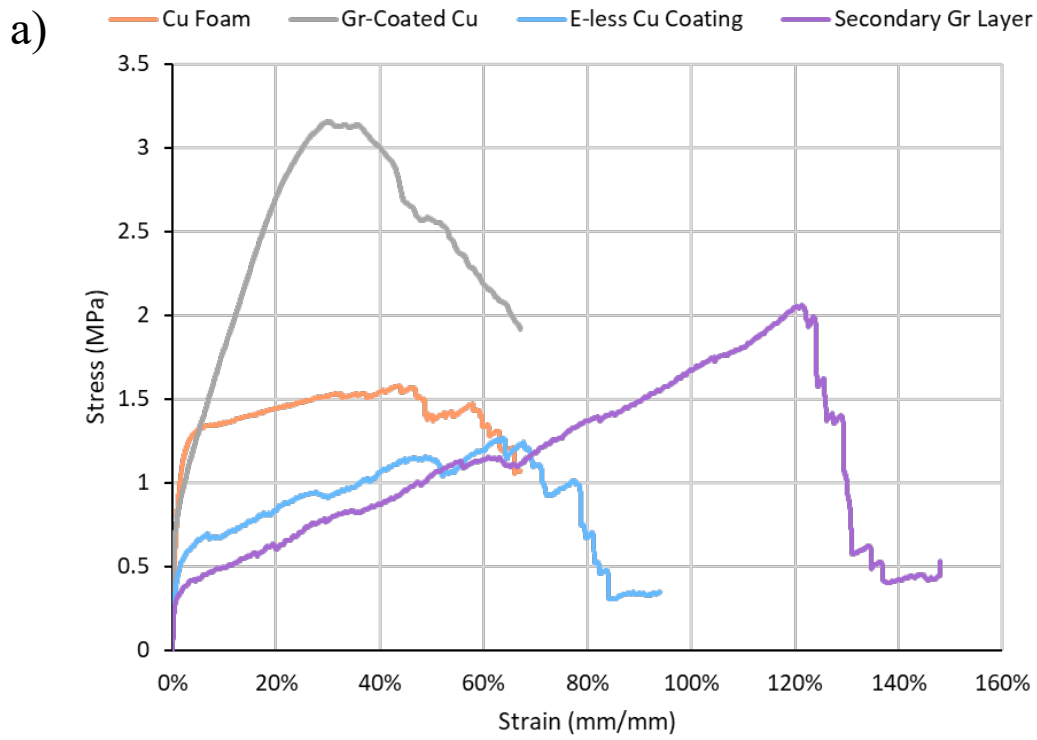


Figure 40 – a) Electrical conductivity of the 40 PPI foam types and b) the percent improvement in thermal conductivity with each additional Gr layer compared to the research objective.

4.2.4 Mechanical Characterization

Finally, mechanical characterization of the composite foams was performed again to understand the effects of a second annealing process. The stress vs. strain curve comparing the 40 PPI 2x compressed foam type at each layer stage is shown in Figure 41 along with graphs of yield strength and Young's modulus to better display the effects of the layers.



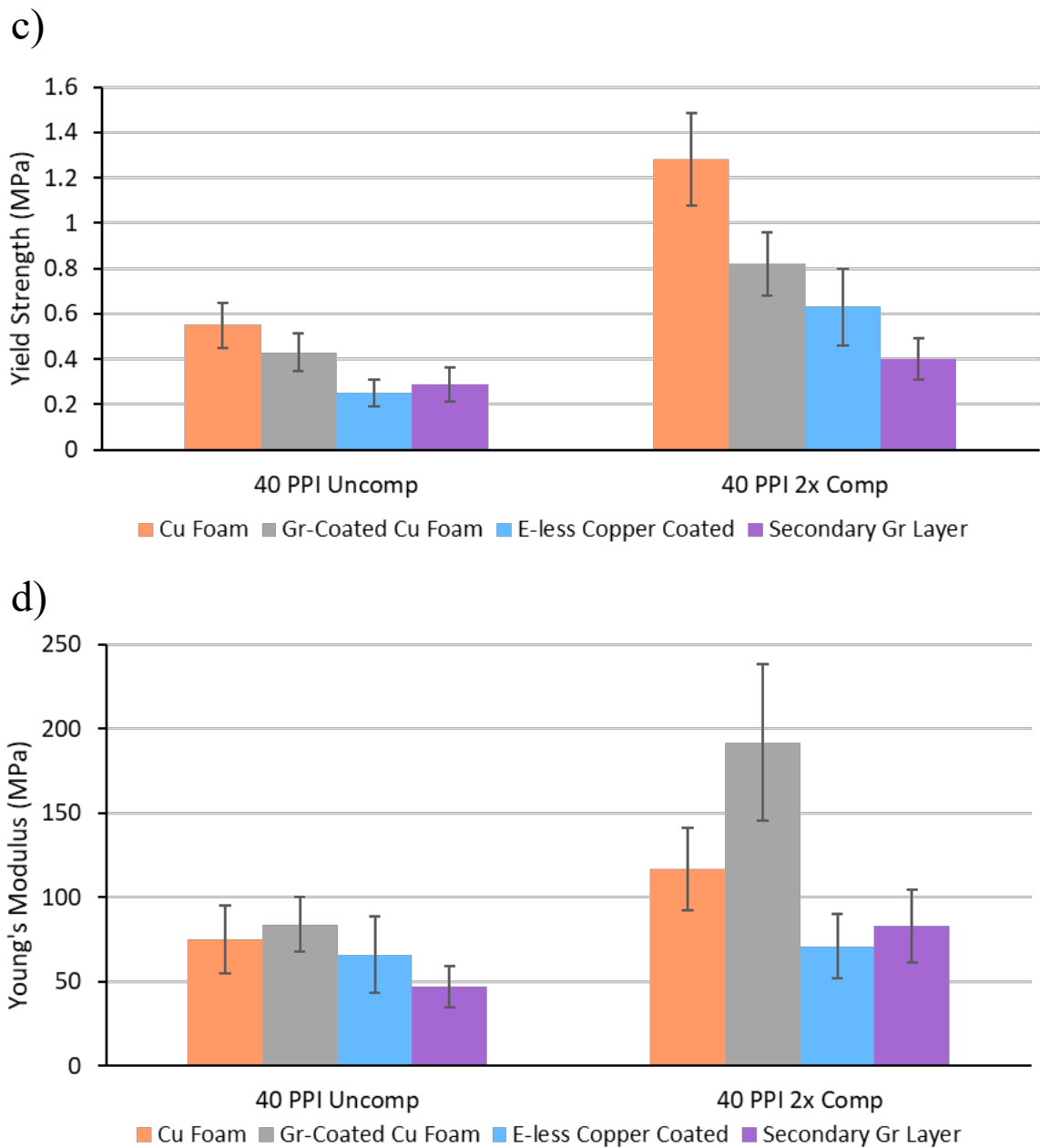


Figure 41 – a) The stress vs. strain curves of the 40 PPI 2x compressed foam type, b) exploded view of the curve to 0.3% strain, c) the yield strengths of the 40 PPI foam types, and d) Young's modulus of the 40 PPI foam types with each added layer.

From the uniaxial tensile tests of the multilayer composite foam, the high-density foam continued to show a large decrease in yield strength and a significant increase in toughness with a UTS at 120% elongation of the foam. Furthermore, there was a significant decrease in yield strength by 65% from the base Cu foam. The low-density foams also had a significant impact from the addition of the secondary graphene layer with a decrease in yield strength by roughly 47% from the base Cu foam. These results indicate that there was further annealing of the base copper structure during the deposition of the secondary graphene layer. Both high-density and low-density foam structures saw a decrease in Young's modulus with addition of both the electroless Cu layer and secondary Gr layer. The low-density 40 PPI foam had a large decrease in the energy absorption (69%) of the foam possibly due to a higher oxide content in the electroless layer. All of the electrical, thermal, and mechanical property characterization of both the low-density and high-density 40 PPI foam types from the pure Cu base foams to the multilayer Gr-coated system is shown in Table 12.

Table 12 – Electrical, thermal, and mechanical properties of both 40 PPI foam types

Foam		Thermal Cond.	Electrical Cond.	Yield Strength	Young's Modulus	Energy Absorption
Type	System	[W/mK]	[MS/m]	[MPa]	[MPa]	[MPa*mm/mm]
40 PPI 2x Comp	Cu	22.1	3.48	0.85	117	0.45
	Cu-Gr	23.6 (+7%)	4.06 (+17%)	0.64 (-25%)	173 (+47%)	0.60 (+33%)
	Cu-Gr-Cu	21.7 (-2%)	3.89 (+12%)	0.42 (-52%)	71 (-39%)	0.73 (+62)
	Cu-Gr-Cu-Gr	25.6 (+16%)	4.35 (+25%)	0.30 (-65%)	83 (-29%)	1.37 (+204%)
40 PPI Uncomp.	Cu	8.5	2.02	0.55	75	0.12
	Cu-Gr	12.8 (+51%)	2.78 (+38%)	0.43 (-21%)	84 (+11%)	0.18 (+44%)
	Cu-Gr-Cu	11.8 (+38%)	2.62 (+30%)	0.24 (-56%)	66 (-12%)	0.04 (-69%)
	Cu-Gr-Cu-Gr	14.2 (+67%)	3.16 (+56%)	0.29 (-47%)	47 (-37%)	0.05 (-59%)

CHAPTER 5. CONCLUSION

5.1 Summary

This work examined the feasibility of conformal graphene coatings on copper foams in wicks and whether multi-layer Cu-Graphene pairs substantially enhance mechanical, thermal, and electrical properties. The graphene layers were deposited onto the foam wick using a high-temperature chemical vapor deposition process, and an electroless deposition process was developed for the intermediate copper layer. Raman and SEM analysis proved the existence of monolayer copper on the surface of the foam, and the property characterization of each deposited graphene layer had large improvements (between 11 – 38% increase) in electrical conductivity and (between 8 – 67%) in thermal conductivity surpassing the original target of 20% improvement over base copper foams for the low-density, well-connected structures. Foams of higher connectivity demonstrated the highest improvements in properties indicating that connectivity of the foam structure plays a greater role in the impact of a graphene coating than general vol% increases. Due to the annealing of the base Cu foam during CVD, there was a decline in the yield strength of the base Cu foams (between ; however, the mechanical toughness of the foams generally increases due to the softening of the base Cu.

The electroless deposition process effectively deposited a Cu layer of full coverage by using a 50°C heated and stirred copper sulfate bath but with high amounts of copper oxide crystals which hindered the measured properties of the foam. A method for measuring the deposition rate of the intermediate copper layer was developed by using a protective polymer coating as a copper growth inhibitor and measuring differential copper

heights using a FIB-SEM. Due to the circulation of the solution, the deepest parts of the foam structure had the lowest deposition rates which were calculated at ~650 nm over 24 hours, significantly lower than on a plain copper sheet. Large decreases in mechanical properties were seen with the addition copper layer, though the thermal and electrical properties had minimal decline (~8% and ~5% respectively) in performance compared to their copper-graphene single-layer precursor.

From a usability and implementation perspective, the first layer graphene addition is the most impactful in terms of property enhancement while also not affecting the wettability of the copper foam. The wettability, capillary pressures, and permeability were verified to be controlled by the underlying base foam when the coating was mono- to tri-layer graphene emphasizing the importance of an optimized base foam for those properties. The thermal and electrical conductivity improvements of the secondary graphene layer demonstrated are only marginal considering the degradation in mechanical properties and increased cost and complexity of fabrication. However, the deposition of the second graphene layer causes significant decomposition of the copper oxides from the electroless process creating numerous micropores – magnitudes smaller than the pores of the base foam – across the foam ligaments and nodes. These micropores have the potential to significantly increase the wetting and capillary properties of the foam wick, which foam wicks typically lack due to their large pore sizes in favor of permeability. The creation of micropores could also provide further nucleation sights for boiling during high-temperature use of the vapor chamber. The design rules derived from this research have created a potential path for fabrication of high-performance wicks to be integrated into miniaturized vapor chambers capable of handling heat fluxes $> 1 \text{ kW/cm}^2$. As such, future work was

developed to understand the path forward for the design and implementation of the composite coating.

5.2 Pathways for Future Work

Further implementation of the Gr-coated foam as wicks will necessitate measurements of the heat spreading in actual chambers. Current processing methods explored in this work make multi-layer Cu-Graphene layer deposition undesirable in terms of property gains. Future work may explore a more optimized electroless deposition system that reduces the nucleation and growth of copper oxides. In the other direction, the reduction of Cu oxides could prove beneficial through the micropore creation demonstrated in this work. A method to introduce these micropores into single-layer applications could be studied to generate the biporous structure. By inducing the original copper foam with a thick Cu/CuO layer, micropores can be introduced into the single-layer composite to reduce the overall cost and complexities that come with multilayer fabrication. Quantitative evaluation of the impact of micropores on permeability and capillary performance should be studied to understand the benefits of the foam's possible biporous nature.

Furthermore, since both deposition processes demonstrated conformal coating capabilities, the composite coating process could be applied to other wick structures that may suffer from low thermal conductivity. As additive manufacturing techniques develop further, optimized wick structures could be developed and manufactured that can take advantage of the property improvements due to improved connectivity and surface-to-volume ratios at higher foam densities. Application of the coating could also be applied to

ultra-thin vapor chamber technologies that rely on thin material systems for optimized performance.

Outside of direct implementation as wick systems, these Gr-coated Cu foam systems could be used as electrically and thermally conductive composite reinforcement for polymer systems. Because of the open-cell design and large pore size, polymers could easily infiltrate the foam structure to create a bulk composite system.

Overall, these pathways of future work illustrate the potential impact of Gr-coated Cu and Cu-Gr composite systems in the thermal management systems of both modern and future electronic packaging architectures for increased longevity and reliability.

REFERENCES

- [1] G. Zhou, J. Li, and Z. Jia, "Power-saving exploration for high-end ultra-slim laptop computers with miniature loop heat pipe cooling module," *Applied Energy*, vol. 239, pp. 859-875, 2019/04/01/ 2019, doi: <https://doi.org/10.1016/j.apenergy.2019.01.258>.
- [2] A. B. Cohen, "ModSim Challenges in Co-Design of Embedded Cooling Solutions ", ed. Pacific Northwest National Laboratory: DARPA, 2015.
- [3] X. C. Tong, "Thermal Management Fundamentals and Design Guides in Electronic Packaging," in *Advanced Materials for Thermal Management of Electronic Packaging*, X. C. Tong Ed. New York, NY: Springer New York, 2011, pp. 1-58.
- [4] R. Siddharth, "Design and Demonstration of 3D Glass Panel Embedded (GPE) Package for Superior Bandwidth and Power-Efficiency," Doctor of Philosophy, Electrical and Computer Engineering, Georgia Institute of Technology, Georgia Tech Library, 2021.
- [5] P. Thanh-Long, Y. Saito, and M. Mochizuki, "Integrated vapor chamber heat spreader for high power processors," in *2014 International Conference on Electronics Packaging (ICEP)*, 23-25 April 2014 2014, pp. 424-428, doi: 10.1109/ICEP.2014.6826719.
- [6] F. Zhou, Y. Liu, and E. M. Dede, "Design, Fabrication, and Performance Evaluation of a Hybrid Wick Vapor Chamber," *Journal of Heat Transfer*, vol. 141, no. 8, 2019, doi: 10.1115/1.4043797.
- [7] J. A. Weibel, S. V. Garimella, and M. T. North, "Characterization of evaporation and boiling from sintered powder wicks fed by capillary action," *International Journal of Heat and Mass Transfer*, vol. 53, no. 19, pp. 4204-4215, 2010/09/01/ 2010, doi: <https://doi.org/10.1016/j.ijheatmasstransfer.2010.05.043>.
- [8] Z. Liu. "AMD Admits Faulty Vapor Chamber Causes RX 7900 XTX Throttling." 2023
- [9] S. Cho, "Thermal Performance Enhancement of Packaging Substrates With Integrated Vapor Chamber," Doctor of Philosophy, School of Mechanical Engineering, Georgia Institute of Technology, Georgia Tech Library, 2018.
- [10] M. Lu, L. Mok, and R. J. Bezama, "A Graphite Foams Based Vapor Chamber for Chip Heat Spreading," *Journal of Electronic Packaging*, vol. 128, no. 4, pp. 427-431, 2005, doi: 10.1115/1.2351908.

- [11] X. Ji, J. Xu, A. M. Abanda, and Q. Xue, "A vapor chamber using extended condenser concept for ultra-high heat flux and large heater area," *International Journal of Heat and Mass Transfer*, vol. 55, no. 17, pp. 4908-4913, 2012/08/01/ 2012, doi: <https://doi.org/10.1016/j.ijheatmasstransfer.2012.04.018>.
- [12] K. Chu *et al.*, "Thermal properties of graphene/metal composites with aligned graphene," *Materials & Design*, vol. 140, pp. 85-94, 2018/02/15/ 2018, doi: <https://doi.org/10.1016/j.matdes.2017.11.048>.
- [13] K. Li *et al.*, "Copper–Carbon Nanotube Composites Enabled by Electrospinning for Advanced Conductors," *ACS Applied Nano Materials*, vol. 3, no. 7, pp. 6863-6875, 2020/07/24 2020, doi: 10.1021/acsanm.0c01236.
- [14] T. Semenic and I. Catton, "Heat Removal and Thermophysical Properties of Biporous Evaporators," 2006. [Online]. Available: <https://doi.org/10.1115/IMECE2006-15928>.
- [15] S.-C. Wu, C.-J. Huang, S.-H. Chen, and Y.-M. Chen, "Manufacturing and testing of the double-layer wick structure in a loop heat pipe," *International Journal of Heat and Mass Transfer*, vol. 56, no. 1, pp. 709-714, 2013/01/01/ 2013, doi: <https://doi.org/10.1016/j.ijheatmasstransfer.2012.09.054>.
- [16] Q. Cai, A. Bhunia, C. Tsai, M. W. Kendig, and J. F. DeNatale, "Studies of material and process compatibility in developing compact silicon vapor chambers," *Journal of Micromechanics and Microengineering*, vol. 23, no. 6, p. 065003, 2013/04/25 2013, doi: 10.1088/0960-1317/23/6/065003.
- [17] G. Chen, Y. Tang, Z. Wan, G. Zhong, H. Tang, and J. Zeng, "Heat transfer characteristic of an ultra-thin flat plate heat pipe with surface-functional wicks for cooling electronics," *International Communications in Heat and Mass Transfer*, vol. 100, pp. 12-19, 2019/01/01/ 2019, doi: <https://doi.org/10.1016/j.icheatmasstransfer.2018.10.011>.
- [18] S.-C. Wong, S.-F. Huang, and K.-C. Hsieh, "Performance tests on a novel vapor chamber," *Applied Thermal Engineering*, vol. 31, no. 10, pp. 1757-1762, 2011/07/01/ 2011, doi: <https://doi.org/10.1016/j.applthermaleng.2011.02.020>.
- [19] T. Liu, W. Yan, W. Wu, and S. Wang, "Thermal performance enhancement of vapor chamber with modified thin screen mesh wick by laser etching," *Case Studies in Thermal Engineering*, vol. 28, p. 101525, 2021/12/01/ 2021, doi: <https://doi.org/10.1016/j.csite.2021.101525>.
- [20] G. Huang, W. Liu, Y. Luo, Y. Li, and H. Chen, "Fabrication and thermal performance of mesh-type ultra-thin vapor chambers," *Applied Thermal Engineering*, vol. 162, p. 114263, 2019/11/05/ 2019, doi: <https://doi.org/10.1016/j.applthermaleng.2019.114263>.

- [21] G. Huang, W. Liu, Y. Luo, and Y. Li, "A novel ultra-thin vapor chamber for heat dissipation in ultra-thin portable electronic devices," *Applied Thermal Engineering*, vol. 167, p. 114726, 2020/02/25/ 2020, doi: <https://doi.org/10.1016/j.applthermaleng.2019.114726>.
- [22] A. Sutygina, U. Betke, G. Hasemann, and M. Scheffler, "Manufacturing of Open-Cell Metal Foams by the Sponge Replication Technique," *IOP Conference Series: Materials Science and Engineering*, vol. 882, no. 1, p. 012022, 2020/07/01 2020, doi: 10.1088/1757-899X/882/1/012022.
- [23] S. Ryu, J. Han, J. Kim, C. Lee, and Y. Nam, "Enhanced heat transfer using metal foam liquid supply layers for micro heat spreaders," *International Journal of Heat and Mass Transfer*, vol. 108, pp. 2338-2345, 2017/05/01/ 2017, doi: <https://doi.org/10.1016/j.ijheatmasstransfer.2017.01.071>.
- [24] B. Sun, C. Peng, D. Yang, and H. Li, "Effect of the Wick and the Working Medium on the Thermal Resistance of FPHP," (in English), *Frontiers in Energy Research*, Original Research vol. 6, 2018-July-24 2018, doi: 10.3389/fenrg.2018.00037.
- [25] D. Huang, L. Jia, H. Wu, and O. Aaker, "Experimental Investigation on the Vapor Chambers with Sintered Copper Powder Wick," *Journal of Thermal Science*, vol. 30, no. 6, pp. 1938-1950, 2021/11/01 2021, doi: 10.1007/s11630-020-1366-3.
- [26] Y.-S. Chen, K.-H. Chien, C.-C. Wang, T.-C. Hung, and B.-S. Pei, "A simplified transient three-dimensional model for estimating the thermal performance of the vapor chambers," *Applied Thermal Engineering*, vol. 26, no. 17, pp. 2087-2094, 2006/12/01/ 2006, doi: <https://doi.org/10.1016/j.applthermaleng.2006.04.008>.
- [27] R. Ranjan, J. Y. Murthy, S. V. Garimella, D. H. Altman, and M. T. North, "Modeling and Design Optimization of Ultrathin Vapor Chambers for High Heat Flux Applications," *IEEE Transactions on Components, Packaging and Manufacturing Technology*, vol. 2, no. 9, pp. 1465-1479, 2012, doi: 10.1109/TCPMT.2012.2194738.
- [28] Y.-S. Chen, K.-H. Chien, C.-C. Wang, T.-C. Hung, Y.-M. Ferng, and B.-S. Pei, "Investigations of the Thermal Spreading Effects of Rectangular Conduction Plates and Vapor Chamber," *Journal of Electronic Packaging*, vol. 129, no. 3, pp. 348-355, 2006, doi: 10.1115/1.2753970.
- [29] Z. Chen, Y. Li, W. Zhou, L. Deng, and Y. Yan, "Design, fabrication and thermal performance of a novel ultra-thin vapour chamber for cooling electronic devices," *Energy Conversion and Management*, vol. 187, pp. 221-231, 2019/05/01/ 2019, doi: <https://doi.org/10.1016/j.enconman.2019.03.038>.
- [30] L. Lv and J. Li, "Managing high heat flux up to 500W/cm² through an ultra-thin flat heat pipe with superhydrophilic wick," *Applied Thermal Engineering*, vol. 122, pp. 593-600, 2017/07/25/ 2017, doi: <https://doi.org/10.1016/j.applthermaleng.2017.05.050>.

- [31] D. Lee and C. Byon, "Fabrication and characterization of pure-metal-based submillimeter-thick flexible flat heat pipe with innovative wick structures," *International Journal of Heat and Mass Transfer*, vol. 122, pp. 306-314, 2018/07/01/ 2018, doi: <https://doi.org/10.1016/j.ijheatmasstransfer.2018.01.135>.
- [32] C. Oshman, Q. Li, L.-A. Liew, R. Yang, V. M. Bright, and Y. C. Lee, "Flat flexible polymer heat pipes," *Journal of Micromechanics and Microengineering*, vol. 23, no. 1, p. 015001, 2012/11/30 2013, doi: 10.1088/0960-1317/23/1/015001.
- [33] Y. Yang, J. Li, H. Wang, D. Liao, and H. Qiu, "Microstructured wettability pattern for enhancing thermal performance in an ultrathin vapor chamber," *Case Studies in Thermal Engineering*, vol. 25, p. 100906, 2021/06/01/ 2021, doi: <https://doi.org/10.1016/j.csite.2021.100906>.
- [34] Y. Nam, S. Sharratt, G. Cha, and Y. S. Ju, "Characterization and Modeling of the Heat Transfer Performance of Nanostructured Cu Micropost Wicks," *Journal of Heat Transfer*, vol. 133, no. 10, 2011, doi: 10.1115/1.4004168.
- [35] R. Lewis, L.-A. Liew, S. Xu, Y.-C. Lee, and R. Yang, "Microfabricated ultra-thin all-polymer thermal ground planes," *Science Bulletin*, vol. 60, no. 7, pp. 701-706, 2015/04/01/ 2015, doi: <https://doi.org/10.1007/s11434-015-0760-9>.
- [36] M. Wei, S. Somasundaram, B. He, Q. Liang, C. S. Tan, and E. N. Wang, "Experimental characterization of Si micropillar based evaporator for advanced vapor chambers," in *2014 IEEE 16th Electronics Packaging Technology Conference (EPTC)*, 3-5 Dec. 2014 2014, pp. 335-340, doi: 10.1109/EPTC.2014.7028412.
- [37] S. Lips, F. Lefèvre, and J. Bonjour, "Combined effects of the filling ratio and the vapour space thickness on the performance of a flat plate heat pipe," *International Journal of Heat and Mass Transfer*, vol. 53, no. 4, pp. 694-702, 2010/01/31/ 2010, doi: <https://doi.org/10.1016/j.ijheatmasstransfer.2009.10.022>.
- [38] L. Chen, D. Deng, Q. Huang, X. Xu, and Y. Xie, "Development and thermal performance of a vapor chamber with multi-artery reentrant microchannels for high-power LED," *Applied Thermal Engineering*, vol. 166, p. 114686, 2020/02/05/ 2020, doi: <https://doi.org/10.1016/j.applthermaleng.2019.114686>.
- [39] S. Goodarzi, T. Da Ros, J. Conde, F. Sefat, and M. Mozafari, "Fullerene: biomedical engineers get to revisit an old friend," *Materials Today*, vol. 20, no. 8, pp. 460-480, 2017/10/01/ 2017, doi: <https://doi.org/10.1016/j.mattod.2017.03.017>.
- [40] S. Margadonna and K. Prassides, "Recent Advances in Fullerene Superconductivity," *Journal of Solid State Chemistry*, vol. 168, no. 2, pp. 639-652, 2002/11/01/ 2002, doi: <https://doi.org/10.1006/jssc.2002.9762>.
- [41] Y. Piao *et al.*, "Optical and Electrical Properties of Inner Tubes in Outer Wall-Selectively Functionalized Double-Wall Carbon Nanotubes," *The Journal of*

Physical Chemistry Letters, vol. 2, no. 13, pp. 1577-1582, 2011/07/07 2011, doi: 10.1021/jz200687u.

- [42] Y. Wang and G. J. Weng, "Electrical Conductivity of Carbon Nanotube- and Graphene-Based Nanocomposites," in *Micromechanics and Nanomechanics of Composite Solids*, S. A. Meguid and G. J. Weng Eds. Cham: Springer International Publishing, 2018, pp. 123-156.
- [43] E.-C. Cho, C.-W. Chang-Jian, Y.-S. Hsiao, K.-C. Lee, and J.-H. Huang, "Three-dimensional carbon nanotube based polymer composites for thermal management," *Composites Part A: Applied Science and Manufacturing*, vol. 90, pp. 678-686, 2016/11/01/ 2016, doi: <https://doi.org/10.1016/j.compositesa.2016.08.035>.
- [44] L. M. Malard, M. A. Pimenta, G. Dresselhaus, and M. S. Dresselhaus, "Raman spectroscopy in graphene," *Physics Reports*, vol. 473, no. 5, pp. 51-87, 2009/04/01/ 2009, doi: <https://doi.org/10.1016/j.physrep.2009.02.003>.
- [45] K. I. Bolotin *et al.*, "Ultrahigh electron mobility in suspended graphene," *Solid State Communications*, vol. 146, no. 9, pp. 351-355, 2008/06/01/ 2008, doi: <https://doi.org/10.1016/j.ssc.2008.02.024>.
- [46] J. B. Oostinga, H. B. Heersche, X. Liu, A. F. Morpurgo, and L. M. K. Vandersypen, "Gate-induced insulating state in bilayer graphene devices," *Nature Materials*, vol. 7, no. 2, pp. 151-157, 2008/02/01 2008, doi: 10.1038/nmat2082.
- [47] A. A. Balandin *et al.*, "Superior Thermal Conductivity of Single-Layer Graphene," *Nano Letters*, vol. 8, no. 3, pp. 902-907, 2008/03/01 2008, doi: 10.1021/nl0731872.
- [48] E. D. Obraztsova, M. G. Rybin, and P. A. Obraztsov, "7 - Optical properties of graphene," in *Graphene (Second Edition)*, V. Skakalova and A. B. Kaiser Eds.: Woodhead Publishing, 2021, pp. 133-142.
- [49] A. R. Urade, I. Lahiri, and K. S. Suresh, "Graphene Properties, Synthesis and Applications: A Review," *JOM*, vol. 75, no. 3, pp. 614-630, 2023/03/01 2023, doi: 10.1007/s11837-022-05505-8.
- [50] E. Solfiti and F. Berto, "Mechanical properties of flexible graphite: review," *Procedia Structural Integrity*, vol. 25, pp. 420-429, 2020/01/01/ 2020, doi: <https://doi.org/10.1016/j.prostr.2020.04.047>.
- [51] A. Kausar and R. Taherian, "2 - Electrical Conductivity in Polymer Composite Filled With Carbon Microfillers," in *Electrical Conductivity in Polymer-Based Composites*, R. Taherian and A. Kausar Eds.: William Andrew Publishing, 2019, pp. 19-40.
- [52] L. Menacho, M. Carrasco, and Z. Ayala, "Comparison between Monolayer and Bilayer Graphene energy bands using the Tight Binding model," *Journal of*

Physics: Conference Series, vol. 1143, no. 1, p. 012022, 2018/12/01 2018, doi: 10.1088/1742-6596/1143/1/012022.

- [53] R. Narayan, J. Lim, T. Jeon, D. J. Li, and S. O. Kim, "Perylene tetracarboxylate surfactant assisted liquid phase exfoliation of graphite into graphene nanosheets with facile re-dispersibility in aqueous/organic polar solvents," *Carbon*, vol. 119, pp. 555-568, 2017/08/01/ 2017, doi: <https://doi.org/10.1016/j.carbon.2017.04.071>.
- [54] L. Hu *et al.*, "Pyrolysis-assisted graphene exfoliation from graphite particles deposited on photoresist pillars," in *2012 12th IEEE International Conference on Nanotechnology (IEEE-NANO)*, 20-23 Aug. 2012 2012, pp. 1-4, doi: 10.1109/NANO.2012.6322004.
- [55] K. V. Emtsev *et al.*, "Towards wafer-size graphene layers by atmospheric pressure graphitization of silicon carbide," *Nature Materials*, vol. 8, no. 3, pp. 203-207, 2009/03/01 2009, doi: 10.1038/nmat2382.
- [56] I. Sharma, G. S. Papanai, S. J. Paul, and B. K. Gupta, "Partial Pressure Assisted Growth of Single-Layer Graphene Grown by Low-Pressure Chemical Vapor Deposition: Implications for High-Performance Graphene FET Devices," *ACS Omega*, vol. 5, no. 35, pp. 22109-22118, 2020/09/08 2020, doi: 10.1021/acsomega.0c02132.
- [57] M. T. Pettes, H. Ji, R. S. Ruoff, and L. Shi, "Thermal Transport in Three-Dimensional Foam Architectures of Few-Layer Graphene and Ultrathin Graphite," *Nano Letters*, vol. 12, no. 6, pp. 2959-2964, 2012/06/13 2012, doi: 10.1021/nl300662q.
- [58] M. Loeblein *et al.*, "High-Density 3D-Boron Nitride and 3D-Graphene for High-Performance Nano-Thermal Interface Material," *ACS Nano*, vol. 11, no. 2, pp. 2033-2044, 2017/02/28 2017, doi: 10.1021/acsnano.6b08218.
- [59] X. Chen, P. K. Eggers, A. D. Slattery, S. G. Ogden, and C. L. Raston, "Template-free assembly of three-dimensional networks of graphene hollow spheres at the water/toluene interface," *Journal of Colloid and Interface Science*, vol. 430, pp. 174-177, 2014/09/15/ 2014, doi: <https://doi.org/10.1016/j.jcis.2014.05.048>.
- [60] W. Zhang *et al.*, "Preparation of graphene foam with high performance by modified self-assembly method," *Applied Physics A*, vol. 122, no. 3, p. 259, 2016/03/03 2016, doi: 10.1007/s00339-016-9684-8.
- [61] J. Sha *et al.*, "Three-Dimensional Printed Graphene Foams," *ACS Nano*, vol. 11, no. 7, pp. 6860-6867, 2017/07/25 2017, doi: 10.1021/acsnano.7b01987.
- [62] A. Azhari, E. Toyserkani, and C. Villain, "Additive Manufacturing of Graphene-Hydroxyapatite Nanocomposite Structures," *International Journal of Applied Ceramic Technology*, <https://doi.org/10.1111/ijac.12309> vol. 12, no. 1, pp. 8-17, 2015/01/01 2015, doi: <https://doi.org/10.1111/ijac.12309>.

- [63] J. Klett, R. Hardy, E. Romine, C. Walls, and T. Burchell, "High-thermal-conductivity, mesophase-pitch-derived carbon foams: effect of precursor on structure and properties," *Carbon*, vol. 38, no. 7, pp. 953-973, 2000/01/01/ 2000, doi: [https://doi.org/10.1016/S0008-6223\(99\)00190-6](https://doi.org/10.1016/S0008-6223(99)00190-6).
- [64] A. Nieto, B. Boesl, and A. Agarwal, "Multi-scale intrinsic deformation mechanisms of 3D graphene foam," *Carbon*, vol. 85, pp. 299-308, 2015/04/01/ 2015, doi: <https://doi.org/10.1016/j.carbon.2015.01.003>.
- [65] K. M. Yocham *et al.*, "Mechanical Properties of Graphene Foam and Graphene Foam—Tissue Composites," *Advanced Engineering Materials*, <https://doi.org/10.1002/adem.201800166> vol. 20, no. 9, p. 1800166, 2018/09/01 2018, doi: <https://doi.org/10.1002/adem.201800166>.
- [66] W. Park, X. Li, N. Mandal, X. Ruan, and Y. P. Chen, "Compressive mechanical response of graphene foams and their thermal resistance with copper interfaces," *APL Materials*, vol. 5, no. 3, p. 036102, 2017/03/01 2017, doi: 10.1063/1.4978272.
- [67] Z. Chen, W. Ren, L. Gao, B. Liu, S. Pei, and H.-M. Cheng, "Three-dimensional flexible and conductive interconnected graphene networks grown by chemical vapour deposition," *Nature Materials*, vol. 10, no. 6, pp. 424-428, 2011/06/01 2011, doi: 10.1038/nmat3001.
- [68] J. Xu, J. Mo, H. Yin, Y. Ma, and Z. Yin, "Study on Enhancement of Heat Dissipation Capacity of Radiating Substrate with Graphene Composite Coating," in *2018 2nd IEEE Conference on Energy Internet and Energy System Integration (EI2)*, 20-22 Oct. 2018 2018, pp. 1-3, doi: 10.1109/EI2.2018.8582198.
- [69] K. Jagannadham, "Orientation dependence of thermal conductivity in copper-graphene composites," *Journal of Applied Physics*, vol. 110, no. 7, p. 074901, 2011/10/01 2011, doi: 10.1063/1.3641640.
- [70] Y. Kim *et al.*, "Strengthening effect of single-atomic-layer graphene in metal-graphene nanolayered composites," *Nature Communications*, vol. 4, no. 1, p. 2114, 2013/07/02 2013, doi: 10.1038/ncomms3114.
- [71] T. Wejrzanowski, M. Grybczuk, M. Chmielewski, K. Pietrzak, K. J. Kurzydowski, and A. Strojny-Nedza, "Thermal conductivity of metal-graphene composites," *Materials & Design*, vol. 99, pp. 163-173, 2016/06/05/ 2016, doi: <https://doi.org/10.1016/j.matdes.2016.03.069>.
- [72] L. Wang *et al.*, "High apparent strengthening efficiency for reduced graphene oxide in copper matrix composites produced by molecule-lever mixing and high-shear mixing," *RSC Advances*, 10.1039/C5RA04782J vol. 5, no. 63, pp. 51193-51200, 2015, doi: 10.1039/C5RA04782J.

- [73] P. Hidalgo-Manrique, X. Lei, R. Xu, M. Zhou, I. A. Kinloch, and R. J. Young, "Copper/graphene composites: a review," *Journal of Materials Science*, vol. 54, no. 19, pp. 12236-12289, 2019/10/01 2019, doi: 10.1007/s10853-019-03703-5.
- [74] D.-B. Xiong *et al.*, "Graphene-and-Copper Artificial Nacre Fabricated by a Preform Impregnation Process: Bioinspired Strategy for Strengthening-Toughening of Metal Matrix Composite," *ACS Nano*, vol. 9, no. 7, pp. 6934-6943, 2015/07/28 2015, doi: 10.1021/acsnano.5b01067.
- [75] X. Si *et al.*, "Effect of carbide interlayers on the microstructure and properties of graphene-nanoplatelet-reinforced copper matrix composites," *Materials Science and Engineering: A*, vol. 708, pp. 311-318, 2017/12/21/ 2017, doi: <https://doi.org/10.1016/j.msea.2017.10.015>.
- [76] K. Chu and C. Jia, "Enhanced strength in bulk graphene-copper composites," *physica status solidi (a)*, <https://doi.org/10.1002/pssa.201330051> vol. 211, no. 1, pp. 184-190, 2014/01/01 2014, doi: <https://doi.org/10.1002/pssa.201330051>.
- [77] Z. An, J. Li, A. Kikuchi, Z. Wang, Y. Jiang, and T. Ono, "Mechanically strengthened graphene-Cu composite with reduced thermal expansion towards interconnect applications," *Microsystems & Nanoengineering*, vol. 5, no. 1, p. 20, 2019/05/20 2019, doi: 10.1038/s41378-019-0059-0.
- [78] J. Yang *et al.*, "Improving the electrical conductivity of copper/graphene composites by reducing the interfacial impurities using spark plasma sintering diffusion bonding," *Journal of Materials Research and Technology*, vol. 15, pp. 3005-3015, 2021/11/01/ 2021, doi: <https://doi.org/10.1016/j.jmrt.2021.09.100>.
- [79] C. Ayyappadas, A. Muthuchamy, A. Raja Annamalai, and D. K. Agrawal, "An investigation on the effect of sintering mode on various properties of copper-graphene metal matrix composite," *Advanced Powder Technology*, vol. 28, no. 7, pp. 1760-1768, 2017/07/01/ 2017, doi: <https://doi.org/10.1016/j.apt.2017.04.013>.
- [80] L. Wang *et al.*, "Graphene-copper composite with micro-layered grains and ultrahigh strength," *Scientific Reports*, vol. 7, no. 1, p. 41896, 2017/02/07 2017, doi: 10.1038/srep41896.
- [81] N. Khobragade, B. Kumar, S. Bera, and D. Roy, "Studies on graphene reinforced Cu base composites prepared by two step thermal processing method," *Materials Today: Proceedings*, vol. 4, no. 8, pp. 8045-8051, 2017/01/01/ 2017, doi: <https://doi.org/10.1016/j.matpr.2017.07.143>.
- [82] X. Zhang, K. Wu, M. He, Z. Ye, S. Tang, and Z. Jiang, "Facile synthesis and characterization of reduced graphene oxide/copper composites using freeze-drying and spark plasma sintering," *Materials Letters*, vol. 166, pp. 67-70, 2016/03/01/ 2016, doi: <https://doi.org/10.1016/j.matlet.2015.12.040>.

- [83] R. K. Singh Raman *et al.*, "Protecting copper from electrochemical degradation by graphene coating," *Carbon*, vol. 50, no. 11, pp. 4040-4045, 2012/09/01/ 2012, doi: <https://doi.org/10.1016/j.carbon.2012.04.048>.
- [84] S. Chen *et al.*, "Oxidation Resistance of Graphene-Coated Cu and Cu/Ni Alloy," *ACS Nano*, vol. 5, no. 2, pp. 1321-1327, 2011/02/22 2011, doi: 10.1021/nn103028d.
- [85] J. Rafiee *et al.*, "Wetting transparency of graphene," *Nature Materials*, vol. 11, no. 3, pp. 217-222, 2012/03/01 2012, doi: 10.1038/nmat3228.
- [86] R. Mishra, J. Militky, and M. Venkataraman, "7 - Nanoporous materials," in *Nanotechnology in Textiles*, R. Mishra and J. Militky Eds.: Woodhead Publishing, 2019, pp. 311-353.
- [87] L. Kumar, M. S. Alam, C. L. Meena, R. Jain, and A. K. Bansal, "Chapter 4 - Fexofenadine Hydrochloride," in *Profiles of Drug Substances, Excipients and Related Methodology*, vol. 34, H. G. Brittain Ed.: Academic Press, 2009, pp. 153-192.
- [88] M. K. Singh and A. Singh, "Chapter 9 - Thermal characterization of materials using differential scanning calorimeter," in *Characterization of Polymers and Fibres*, M. K. Singh and A. Singh Eds.: Woodhead Publishing, 2022, pp. 201-222.
- [89] A. A. Ramadan, R. D. Gould, and A. Ashour, "On the Van der Pauw method of resistivity measurements," *Thin Solid Films*, vol. 239, no. 2, pp. 272-275, 1994/03/01/ 1994, doi: [https://doi.org/10.1016/0040-6090\(94\)90863-X](https://doi.org/10.1016/0040-6090(94)90863-X).
- [90] S. Bhaviripudi, X. Jia, M. S. Dresselhaus, and J. Kong, "Role of Kinetic Factors in Chemical Vapor Deposition Synthesis of Uniform Large Area Graphene Using Copper Catalyst," *Nano Letters*, vol. 10, no. 10, pp. 4128-4133, 2010/10/13 2010, doi: 10.1021/nl102355e.
- [91] W. Zhang, P. Wu, Z. Li, and J. Yang, "First-Principles Thermodynamics of Graphene Growth on Cu Surfaces," *The Journal of Physical Chemistry C*, vol. 115, no. 36, pp. 17782-17787, 2011/09/15 2011, doi: 10.1021/jp2006827.
- [92] A. August and B. Nestler, "About the surface area to volume relations of open cell foams," *Engineering Research Express*, vol. 2, no. 1, p. 015021, 2020/01/23 2020, doi: 10.1088/2631-8695/ab6ac6.
- [93] D. L. Nika and A. A. Balandin, "Phonons and thermal transport in graphene and graphene-based materials," *Reports on Progress in Physics*, vol. 80, no. 3, p. 036502, 2017/01/20 2017, doi: 10.1088/1361-6633/80/3/036502.
- [94] S. Hu, J. Chen, N. Yang, and B. Li, "Thermal transport in graphene with defect and doping: Phonon modes analysis," *Carbon*, vol. 116, pp. 139-144, 2017/05/01/ 2017, doi: <https://doi.org/10.1016/j.carbon.2017.01.089>.

- [95] S. K. Jaćimovski, M. Bukurov, J. P. Šetrajčić, and D. I. Raković, "Phonon thermal conductivity of graphene," *Superlattices and Microstructures*, vol. 88, pp. 330-337, 2015/12/01/ 2015, doi: <https://doi.org/10.1016/j.spmi.2015.09.027>.
- [96] X. P. Qiu *et al.*, "Disorder-free sputtering method on graphene," *AIP Advances*, vol. 2, no. 3, p. 032121, 2012/09/01 2012, doi: 10.1063/1.4739783.
- [97] S. Ghosh, "Electroless copper deposition: A critical review," *Thin Solid Films*, vol. 669, pp. 641-658, 2019/01/01/ 2019, doi: <https://doi.org/10.1016/j.tsf.2018.11.016>.
- [98] Y. Shacham-Diamand and V. M. Dubin, "Copper electroless deposition technology for ultra-large-scale-integration (ULSI) metallization," *Microelectronic Engineering*, vol. 33, no. 1, pp. 47-58, 1997/01/01/ 1997, doi: [https://doi.org/10.1016/S0167-9317\(96\)00030-5](https://doi.org/10.1016/S0167-9317(96)00030-5).
- [99] U. Narula, C. M. Tan, and E. S. Tok, "Metal on Graphenated Metal for VLSI Interconnects," *Advanced Materials Interfaces*, <https://doi.org/10.1002/admi.201800270> vol. 5, no. 13, p. 1800270, 2018/07/01 2018, doi: <https://doi.org/10.1002/admi.201800270>.
- [100] P. A. Khomyakov, G. Giovannetti, P. C. Rusu, G. Brocks, J. van den Brink, and P. J. Kelly, "First-principles study of the interaction and charge transfer between graphene and metals," *Physical Review B*, vol. 79, no. 19, p. 195425, 05/20/ 2009, doi: 10.1103/PhysRevB.79.195425.
- [101] A. Dahal, R. Addou, H. Coy-Diaz, J. Lallo, and M. Batzill, "Charge doping of graphene in metal/graphene/dielectric sandwich structures evaluated by C-1s core level photoemission spectroscopy," *APL Materials*, vol. 1, no. 4, p. 042107, 2013/10/01 2013, doi: 10.1063/1.4824038.
- [102] D. J. Cole, P. K. Ang, and K. P. Loh, "Ion Adsorption at the Graphene/Electrolyte Interface," *The Journal of Physical Chemistry Letters*, vol. 2, no. 14, pp. 1799-1803, 2011/07/21 2011, doi: 10.1021/jz200765z.
- [103] U. Narula, C. M. Tan, and E. S. Tok, "Graphene as a Reducing Agent for Electroless Plating of Metal," in *2018 IEEE 13th Nanotechnology Materials and Devices Conference (NMDC)*, 14-17 Oct. 2018 2018, pp. 1-4, doi: 10.1109/NMDC.2018.8605846.
- [104] L. Chen and S. Kumar, "Thermal transport in graphene supported on copper," *Journal of Applied Physics*, vol. 112, no. 4, p. 043502, 2012, doi: 10.1063/1.4740071.